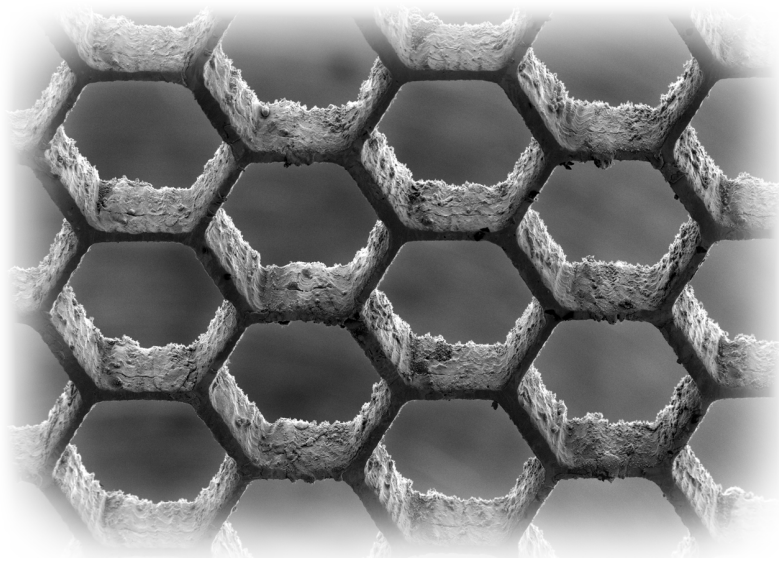


# Thermoelectronic Power Generation from Solar Radiation and Heat



Dissertation zur Erlangung des Doktorgrades

an der Mathematisch-Naturwissenschaftlichen Fakultät  
der Universität Augsburg

vorgelegt von

Cyril Stephanos

Augsburg, November 2012

*Figure on title page:  
Scanning electron microscope (SEM) picture of a  
laser-cut tungsten foil with a honeycomb pattern.  
Such a metallic grid is an essential component  
of thermoelectronic energy converters.  
Photograph by B. Fenk, Max-Planck-Institute Stuttgart.*

Erstgutachter: Prof. Dr. Jochen Mannhart  
Zweitgutachter: Prof. Dr. Armin Reller  
Tag der mündlichen Prüfung: 17. Dezember 2012





# Contents

<b>1</b>	<b>Introduction</b>	<b>1</b>
<b>2</b>	<b>Introduction to Thermionic Energy Conversion</b>	<b>3</b>
2.1	Working Principle, Applications and Main Challenges . . . . .	3
2.2	Approaches to Avoid the Influence of the Space Charge . . . . .	6
2.3	Work Function and Contact Potential . . . . .	8
2.4	Electron Emission Phenomena . . . . .	12
2.5	Ideal Output Characteristics and Efficiency . . . . .	16
2.6	Analogy and Comparison of Thermionic and Thermoelectric Converters	26
2.7	Brief Historical Overview . . . . .	29
<b>3</b>	<b>Concept of Thermoelectronic Energy Converters</b>	<b>31</b>
3.1	Working Principle and Introduction of the New Model . . . . .	31
3.2	Electrons in Electric and Magnetic Fields . . . . .	35
3.3	Guidelines for Efficient Energy Converters with Gate Electrodes . . . . .	42
3.4	Model Calculations for Thermoelectronic Energy Converters . . . . .	46
<b>4</b>	<b>One-Dimensional Current Model</b>	<b>57</b>
4.1	Basic Principles of One-Dimensional Electrostatic Calculations . . . . .	57
4.2	Established Space-Charge Theories for Plane-Parallel Converters . . . . .	59
4.3	Model for an Ideal Gate . . . . .	67
4.4	Current-Tube Model - Connection to Experimental Set-Up . . . . .	81
4.5	Main Conclusions of the One-Dimensional Model Calculations . . . . .	83
<b>5</b>	<b>Experimental Investigation of the Concept</b>	<b>85</b>
5.1	Overview of the Experimental Setup and Development Stages . . . . .	85
5.2	Main Experimental Results . . . . .	90
5.3	Comparison of Experimental Results and Model Calculations . . . . .	94
<b>6</b>	<b>Transition to Small-Scale, Efficient Thermoelectronic Energy Converters</b>	<b>101</b>
6.1	Transition to Smaller Dimensions and Higher Current Densities . . . . .	101
6.2	Efficiencies of Small-Scale Thermoelectronic Energy Converters . . . . .	106
6.3	Possible Material Classes for Practical, Thermoelectronic Converters . . . . .	112
6.4	Potential Enhancements to Our Concept . . . . .	114
<b>7</b>	<b>Summary</b>	<b>117</b>

<b>8 Conclusion</b>	<b>119</b>
<b>A Appendix</b>	<b>121</b>
A.1 Source Code for the Numerical Calculations . . . . .	121
<b>Bibliography</b>	<b>133</b>

# 1 Introduction

Energy consumption pervades modern-day lives, including many aspects of entertainment, information, security, infrastructure, or health, to name but a few. We consume energy directly, *e.g.*, when using mobile devices, making coffee or taking the car, or contribute indirectly to energy consumption, by buying products, using the internet or eating out. Even when exploring wild nature, we use battery powered torches, cameras, or space-based satellite navigation systems.

Technological progress and our constantly evolving life style have led to a steadily growing demand in energy. Over the last forty years, global energy consumption has more than doubled [1]. Although this rate of development seems to be slowing down in highly developed countries, energy demand is growing fast in newly industrialized countries like China, India or parts of South America, as they are striving to close the technological gap. In China alone, energy consumption has increased by over 300 % over the same period of time [1]. Furthermore, CO<sub>2</sub> emission, nuclear waste as well as the exploitation of resources, have had a long lasting impact on landscapes and ecosystems.

To reduce the dependency on conventional energy resources, new, efficient methods of energy conversion and renewable energies are being explored. Especially the harvesting of solar energy holds enormous potential, as the solar power reaching Earth exceeds the global consumption of primary energy by a factor of 10000.

However, solar energy still constitutes less than 1 % of human global energy production [1], as new technologies are expensive and need time to develop. Assessing and enhancing existing energy conversion processes is therefore indispensable to reducing the consumption of critical resources and limiting the environmental impact.

Converting heat into electric power accounts for the generation of about 80 % of today's electricity [1]. However, technical limitations prevent the heat, mainly generated by burning fossil fuels or even concentrating solar power, from being fully utilized. Coal, for example — responsible for approximately 40 % of global electricity production [1] — is burned at a temperature of 1500 °C–1600 °C [2]. The steam turbines that are used in coal-combustion power plants, however, work with inlet temperatures of only about 600 °C [2]. Due to this significant temperature gap, excess energy is lost in the process.

Thermionic energy conversion, as explored and developed in the frame of this and Stefan Meir's theses [3], provides an opportunity to close this gap by converting the excess energy into electrical output power. Thermionic converters can work efficiently at very high inlet temperatures, while rejecting heat that can be used to power secondary heat engines. This way, the generated heat can be fully utilized and the efficiency of the energy conversion process is greatly enhanced [4].

The concept of thermionic energy conversion was developed in the beginning of the 20th century, and was the subject of intensive research in the 1950s and 1960s [5,6]. The

concept is simple [6, 7]: electrons are emitted from a heated metal electrode in vacuum and absorbed on a second, cooler metal electrode. This electron flow induces a voltage difference that can be used to source a current and generate electrical power.

In addition to improving the efficiency of existing conversion processes, thermionic converters have the potential to be used as highly-efficient autonomous heat engines, *e.g.*, in space applications [5, 8], or for converting fuel-combustion heat in cars [4]. For solar applications, the electron emission can be enhanced by exploiting the photoelectric effect [9], making them candidates for converting solar energy to electricity with unprecedented efficiency.

The main obstacle facing this technology is the formation of a space-charge cloud inside the converters, which dramatically reduces their efficiency. Despite intensive efforts, no solution to this problem has so far been found.

In this thesis, I will present a new concept that abolishes the space-charge cloud and enables a virtually space-charge free electron transport in thermionic converters. Our concept uses a positively charged gate electrode that creates a potential trough, which accelerates the electrons away from the concentrated space-charge region. The gate is a structured metal grid mounted between the two electrodes. A magnetic field is used to prevent the electrons from reaching the gate by channeling them through the gate openings. This new concept involves exclusively electrons and no ions. It is therefore best characterized as ‘thermoelctronic energy conversion’.

Under the guidance of Prof. Dr. Mannhart, we developed this project in a team. We collaborated closely on all aspects of the project; Stefan Meir focused on the experimental setup and measurements, while I was responsible for theoretical considerations and model calculations of the system.

We created a mechanical setup to investigate the working principle and the effect of the electric and magnetic fields. We further developed model calculations based on established space-charge theories to predict the performance of the energy converters and to compare them to the experimental results.

I will look in detail into the physical principles of thermoelectronic energy conversion and determine the ultimate conversion efficiency limit. After introducing the newly developed model, I will concentrate on theoretical considerations and model calculations. I will give a brief overview of our experimental setup and measurements, which are described in detail by Stefan Meir in reference [3]. Finally, I will explore potential efficiencies of thermoelectronic energy converters based on our new concept, both for combined cycle systems and stand-alone converters and the compelling implications for solar energy converters.

Throughout this thesis, the electric potential and the current will be used related to electrons rather than positive charges. The current therefore indicates the direction of motion of electrons, and a positive potential indicates a repelling potential for electrons.

## 2 Introduction to Thermionic Energy Conversion

In this chapter, I will present an overview of the fundamental principles of thermionic energy converters. After introducing the basic working principle, possible applications, and the main challenges, I will focus on two physical concepts, the work function and electron emission, that are essential for thermionic energy conversion and will play a crucial role throughout the course of this work. Building on that, I will determine the efficiency limit for thermionic devices and illustrate the analogies between thermionic and thermoelectric converters. At the end of the chapter I will give a brief historical overview of thermionic energy conversion.

### 2.1 Working Principle, Applications and Main Challenges

A thermionic energy converter (TIC) is a heat engine that converts thermal energy to electrical energy. Electrons are thermally emitted from a hot surface — called the emitter — and absorbed on a second, cold surface — the collector. As a result, a voltage difference between the two electrodes is induced, which can be used to drive a current through a load resistance. In its most basic form, a thermionic converter consists only of an emitter and a collector in vacuum, an electrical load resistance and the electrical connections (figure 2.1).

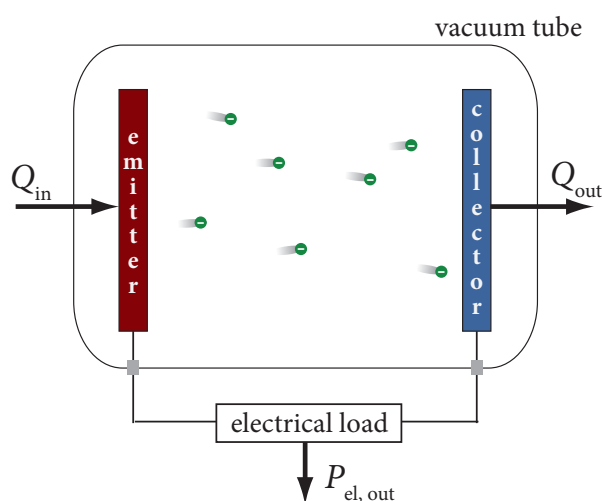


Figure 2.1: Sketch of the essential parts and the working principle of a thermionic energy converter. Electrons are emitted from the heated emitter surface and absorbed by the cold collector. A voltage is induced, which can be used to source a current through an electrical load.

The efficiency limit for every heat engine is given by the Carnot efficiency  $\eta_{\text{Carnot}}$ , which is determined only by the temperatures  $T_{\text{hot}}$  and  $T_{\text{cold}}$  of the hot and cold heat reservoirs

$$\eta_{\text{Carnot}} = 1 - \frac{T_{\text{cold}}}{T_{\text{hot}}}. \quad (2.1)$$

In a TIC, the temperatures that may be applied are, in principle, only limited by the melting point of the metals. Since the heat transport in vacuum is small, a high temperature difference between the two metal plates can be maintained during operation. Therefore, very high temperature differences between emitter and collector can be applied, implying a high Carnot efficiency limit.

Different to most other heat engines generating electrical power from thermal energy, a TIC does not use mechanical work as an intermediate step, leading to fewer potential energy loss channels. Furthermore, the main process in a TIC, the emission and absorption of electrons, is reversible, if thermalization of the electrons can be avoided (see chapter 2.5). As a consequence, the efficiencies of TICs can in principle be very high, close to  $\eta_{\text{Carnot}}$ .

By reversing the working principle, thermionic devices can be operated as heat pumps and therefore be used for refrigeration [10].

### Applications for Thermionic Energy Converters

Possibly the greatest advantage of TICs lies in the high-temperature regime, which is typically reached by combustion or nuclear decay, or even by concentrated solar light.

The high applied temperatures also open up the possibility of using a TIC as a topping cycle. The rejected heat from the collector can be used to power a second heat engine that is particularly efficient in a lower temperature regime, such as a steam turbine or a Stirling motor. As a result, a very high overall efficiency is obtained [4, 11–13].

Further advantages of TICs are that no moving parts and no working liquid or gas are used, enabling a potentially long lifetime and low maintenance, a high power density, a small size and a possibly low mass of the devices [5, 6].

These properties are specifically suited to space applications, but also make thermionic converters compelling candidates for converting fuel combustion heat into electricity for use in transportation purposes, *e.g.* in cars. For space applications, nuclear fueled and solar converters have already been considered in the past, mainly with a cylindrical geometry (figure 2.2), because this setup enables specifically high power densities [14].

TICs can also be used terrestrially to convert solar heat to electricity. They could be installed in the focal point of parabolic dish concentrators tracking the solar light, analogous to Stirling Dishes [15] used today. They could be used either as stand-alone devices or in a combined cycle to enhance the efficiency of existing solar concentrated power plants. For solar applications, the emission current can furthermore be enhanced by exploiting the photonic character of light [9], leading to significant current densities even for moderate temperatures, and therefore very high conversion efficiencies.

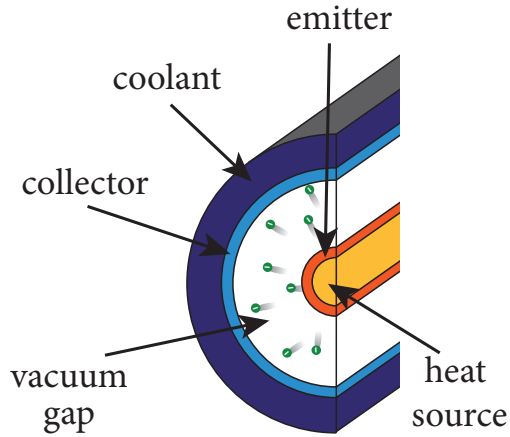


Figure 2.2: Sketch of a cross section of a thermionic energy converter with a cylindrical geometry. This setup is specifically suited for high power densities.

One advantage that is often overlooked is that thermionic energy converters are completely silent, making them interesting, *e.g.*, for microelectronic applications, both for power generation or refrigeration purposes.

### Main Challenges for Efficient Thermionic Energy Conversion

Despite their great potential, the development and application of thermionic converters have been held back in the past by the low efficiency of practical devices. The two main obstacles preventing highly-efficient TICs are the demanding material requirements and the formation of a space-charge region in the inter-electrode space.

For a practical and efficient TIC, longtime stable materials with specific physical and chemical properties are required. Most importantly, emitter and collector need to have work functions in a particular range. To obtain sufficient current densities, the emitter work function  $\phi_e$  has to be sufficiently low, typically below 3 eV. For a high efficiency, the collector work function  $\phi_c$  should be very low, ideally in the range 0.5 eV–1.5 eV.

Over the past 50 years, tremendous progress has been made in material research. Finding a suitable emitter material appears attainable today. The collector material presents a much greater challenge, since not many longtime-stable materials with very low work functions are known. However, in recent years several promising material systems have emerged. Furthermore, coating of the collector surface with few atomic layers of certain elements, such as Ba, La, Cs or metal oxides, thereby significantly reducing the work function [6, 16], remains a possibility. In chapter 6.3, I will briefly discuss possible material systems suited to thermionic energy conversion.

Besides this technical obstacle, the second — intrinsic — challenge, which has proven difficult to overcome until today, is the formation of a space-charge cloud between emitter and collector, which drastically reduces the current density, the output power and the efficiency of the devices. Emitted electrons form a cloud of negative charges close to the emitter surface in the vacuum gap, repelling following electrons. A significant part of the emitted electrons is forced back to the emitter and does not reach the collector. Figure 2.3 shows a sketch of the space-charge formation in a TIC.

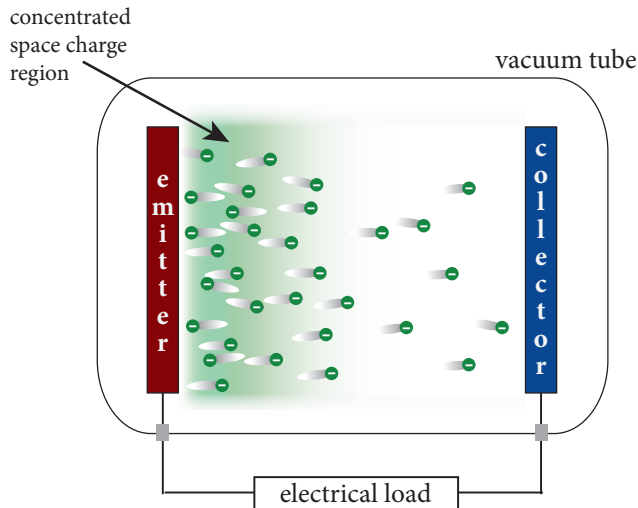


Figure 2.3: Sketch of the space-charge formation in a thermionic energy converter. Electrons in the inter-electrode space form a cloud of negative charges. Following emitted electrons are repelled and pushed back to the emitter. As a consequence, only a fraction of the emitted electrons reach the collector.

The space-charge cloud creates a negative, repulsive potential for the emitted electrons. The size of the potential depends on several experimental parameters, such as the geometrical arrangement of emitter and collector, the emitter work function  $\phi_e$  and the emitter temperature  $T_e$ . As an example, in a TIC with an emitter-collector distance of  $d_{ec} = 500 \mu\text{m}$ , the output current is reduced to a few percent of the saturation value, reducing the output power by the same ratio.

## 2.2 Approaches to Avoid the Influence of the Space Charge

To avoid the detrimental influence of the space charge, three different approaches have been developed: (1) reducing the emitter-collector distance, preventing the formation of a strong charge cloud; (2) inserting positively charged ions into the converter to compensate for the negative charge of the electrons; and (3) applying electric fields to accelerate the electrons out of the space-charge region, possibly in combination with a magnetic guiding field. Below I will briefly discuss the three approaches and their specific advantages and disadvantages.

### Close-Space Technique

Reducing the emitter-collector distance  $d_{ec}$  leads to fewer electrons in the inter-electrode space, which additionally reach the collector faster. As a consequence of this, the space-charge density is reduced. Figure 2.4 shows the maximum height of the space-charge potential  $\Phi_{sc,max}$  and the current density  $J$  plotted as a function of  $d_{ec}$  for a plane-parallel TIC. High current densities can only be achieved for distances of the order of few micrometers.

High efficiencies have been predicted for close-space energy converters. In 1956, Hatsopoulos and Kaye reported of a prototype device with an efficiency of nearly 13 % for

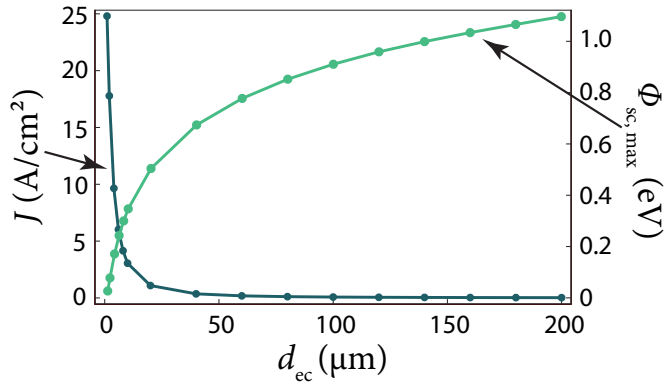


Figure 2.4: Current density  $J$  (blue curve) and space-charge potential maximum  $\Phi_{sc,max}$  (green curve) plotted as a function of the emitter-collector distance  $d_{ec}$  for a plane-parallel TIC. Significant current densities are only obtained for distances of the order of few micrometers. The following typical parameters were used:  $\phi_e = 2.5$  eV,  $T_e = 1500$  °C. The collector back emission was considered to be negligible.

a distance of about  $10 \mu\text{m}$  [17]<sup>1</sup>. Since then, much effort has been put into the development of micro-thermionic converters (MTCs). However, the performance of practical devices has been worse than expected and the close-space technique has, to our knowledge, not been industrially realized until today, despite progress in technical and material research [5, 18, 19]. The main reason for this is the difficulty to mechanically control and maintain the very small distances when high temperature differences are applied.

Recent studies have shown that if the gap size is reduced below  $d_{ec} \lesssim 1 \mu\text{m}$ , additional processes, like electron tunneling or near-field radiative heat loss, come into play [20–22]. Optimal emitter-collector distances have been found to be in the range of  $0.9 \mu\text{m}$ – $3 \mu\text{m}$  [20].

## Vapor Diodes

In a vapor diode positively charged ions are inserted into the inter-electrode space to compensate for the negative charges of the electrons. The value of the space charge is a function of the density of charged particles. It is therefore smaller for higher particle velocities. Due to the much higher mass of the ions, the ion current has to be only a fraction of the electron current. As Cesium exhibits the lowest ionization energy of all stable elements and has a high mass, it has become the standard element used in vapor diodes [23]. A further advantage is the property of Cs to condense on the metallic surfaces, significantly lowering their work functions [24].

When Cs gas is inserted into the converter, ions can be generated by either volume ionization or surface ionization. Although only very little power is expended for surface ionization, it has proven to be impractical, because the electrode work function needs to be at least as high as the Cs ionization energy of 3.9 eV [4]. As I will show in section 2.4, no sufficient emission current can be obtained for such high work functions.

In the volume ionization method — which is called the ‘ignited (arc) mode’,  $\text{Cs}^+$  ions are produced through collisional processes. To maintain the discharge, a voltage drop be-

<sup>1</sup>This value is often cited as a proof for the practicability of close-space converters. It should be mentioned, however, that this prototype model consisted of two metal cylinders with diameters of about 3 mm. The current was measured only at the tips of these cylinders and the efficiency was extrapolated from the measured current.

tween emitter and collector of approximately 0.5 V is needed [4, 24]. This voltage difference lowers the output power by about 50 % [4], significantly lowering the efficiency of the energy converter.

Further disadvantages of the vapor diodes are energy losses through electron collisions and an additional heat transfer through the inserted gas. Despite these drawbacks, ignited-mode TICs have become the basis for most practical devices until today [4, 5, 24].

### Electric and Magnetic Field Approach

The space-charge cloud is formed very close to the emitter surface. Electric fields can be used to accelerate electrons away from the emitter, diffusing the concentrated charge cloud [6]. The space-charge potential is further weakened due to the higher electron velocity. A magnetic guiding field can be applied to prevent electrons from reaching the gate electrode. However, no efficient energy converters using this approach could be built, mainly due to high energy losses on the positively charged gate electrodes, and it has been abandoned completely.

Despite these efforts, no solution for the space-charge problem has yet been found. In the next chapter, I will introduce our new concept, which is based on the electric and magnetic field approach and accomplishes to completely suppress the space charge in thermionic devices.

## 2.3 Work Function and Contact Potential

The work function  $\phi$  of a material is defined as the minimal energy required to remove an electron from inside the material from the electrochemical potential  $\mu$  to an infinite distance, *i.e.*<sup>2</sup>

$$\phi \equiv E_{\text{vac}} - \mu. \quad (2.2)$$

$\phi$  is a material constant and depends on different parameters, including the surface structure, the surface charge distribution, and, for conducting materials, the image force [25, 26]. For many applications, the work function is assumed to be independent from the temperature  $T$ . This assumption is only an approximation, but for many materials, especially metals,  $\phi$  can be considered constant without introducing significant errors. Throughout the course of this work I will neglect the temperature dependence of  $\phi$ , as the exact behavior of the work function is not crucial to the model system I will present.

The work function of pure elements ranges from 2 eV–5 eV [27, p.12-126]. While compound materials can have work functions differing from their single elements, they mostly lie within the same range. However, by modifying the surface structure of a material, the

---

<sup>2</sup>This definition is strictly only valid for metals with uniform surfaces. For certain materials, different surfaces can have differing work functions, leading to surface charges that create an electric field and shift the vacuum levels, analogous to the effect of the contact potential.

work function can be strongly influenced. A commonly applied method is to create a dipole layer of few atomic layers on the surface of a material, thereby significantly reducing  $\phi$ . Pure tungsten for example — a material frequently used in vacuum tubes and TICs due to its high temperature stability — has a work function of approximately 4.5 eV. When coated with barium,  $\phi$  is reduced to about 2 eV [28], while a layer of Cs-atoms can reduce it to even below 1 eV [16].

### Contact Potential

I shall now consider two metals with different work functions  $\phi_1$  and  $\phi_2$ . When no electric potential is applied and the two metals are insulated from each other, no electric field exists between them. Consequently, the vacuum energy level  $E_{\text{vac}}$  has to be the same for both metals (figure 2.5 (a)). Electrons that reach the ‘surface just outside the metal’, as indicated in the figure, are considered to have overcome the work function. This is only an approximation, as the image force scales with  $1/r^2$ . For a distance of more than about 0.1  $\mu\text{m}$ , however, its influence is negligible and the electric potential is equivalent to  $E_{\text{vac}}$  [29]. I will use this notation throughout the course of this work.

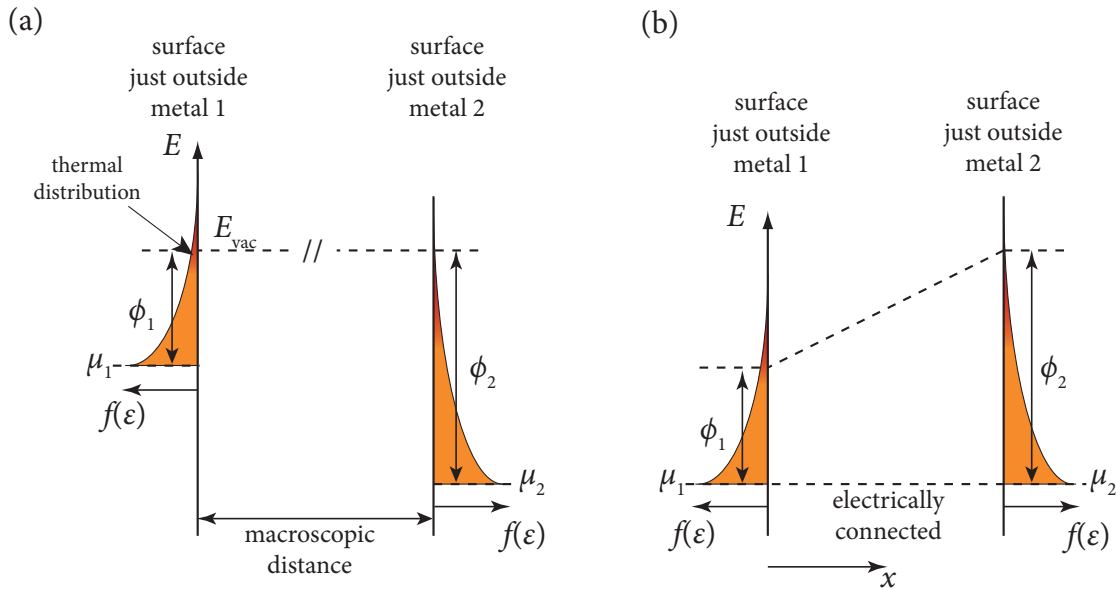


Figure 2.5: Sketch illustrating the electric potentials of two different metals with work functions  $\phi_1$  and  $\phi_2$ . The thermal distribution of the electrons above the electrochemical potential is indicated, too. (a) The two metals are at a macroscopic distance and electrically insulated from each other. If no electric potential is applied and both metals are electrically neutral, no electric field exists between them. (b) When the metals are electrically connected, electrons flow from one metal to the other until the electrochemical potentials are balanced. The charge transport leads to surface charges, which shift the electrical potentials of the metals and induce an electric field between them.

When the two metals are electrically connected, electrons flow from one metal to the other until the electrochemical potentials  $\mu_1$  and  $\mu_2$  are equal (figure 2.5 (b)). Since there

was a transport of charge, the electric potentials of the two metals are no longer equal. There are surface charges on each metal, which shift the electrochemical potentials and create an electric field between the two metals.

The difference of the electric potentials — called the contact potential — can be made evident as follows: an electron is removed from metal 1 into the vacuum by investing the energy  $\phi_1$ . It travels to metal 2. By entering, it gains the energy  $\phi_2$ . The electron can now move freely from metal 1 to metal 2 through the electrical connection. Assuming  $\phi_1 < \phi_2$  — as indicated in figure 2.5 (b), the conservation of energy requires the electron to perform the work  $W = \phi_2 - \phi_1$  to travel from metal 1 to metal 2 in the vacuum space. This is equivalent to a potential difference of  $\phi_2 - \phi_1$ , creating an electric field between the metal surfaces, decelerating electrons traveling from metal 1 to metal 2. This well known effect is used, *e.g.*, in ‘Kelvin Probe force microscopy’ [30] to determine the work functions of materials.

The contact potential is essential for thermionic energy converters. On the one hand, the work function of the emitter  $\phi_e$  has to be low enough to obtain a sufficient emitter current. On the other hand, the collector work function  $\phi_c$  has to be lower than  $\phi_e$  so that all emitted electrons reach the collector. Furthermore, it has to be considered that, when electric power is generated, the load voltage increases the electric potential of the collector. Figure 2.6 illustrates the different potentials in a TIC. As I will show in section 2.5, the ideal configuration for thermionic energy converters is obtained when both emitter and collector are on the same electric potential. In this case — if the space charge could be neglected — all electrons emitted reach the emitter.

Figure 2.6 further demonstrates that a lower collector work function enables a higher load voltage and consequently a higher electrical output power. Electrons leaving the emitter have a kinetic energy  $E_{\text{kin}} \geq \phi_e$ . When the electrons are absorbed by the collector, a certain fraction of their kinetic energy is converted into the energy  $eV_{\text{load}}$ , while the remaining energy heats the collector and is lost<sup>3</sup>. Decreasing  $\phi_c$  directly translates into a higher power output. A low collector work function is thus crucial for an efficient thermionic energy converter.

### Space Charge as Effective Work Function

The space charge creates a negative electric potential  $\Phi_{\text{sc}}$ . Only electrons with sufficient initial kinetic energy to overcome the space-charge maximum  $\Phi_{\text{sc,max}}$  reach the collector. The space charge effectively increases the work function in a TIC to  $\phi_e + e\Phi_{\text{sc,max}}$ , as illustrated in figure 2.7.

---

<sup>3</sup>When the TIC is used as a topping cycle, the energy heating the collector is not lost, but used to power a secondary heat engine.

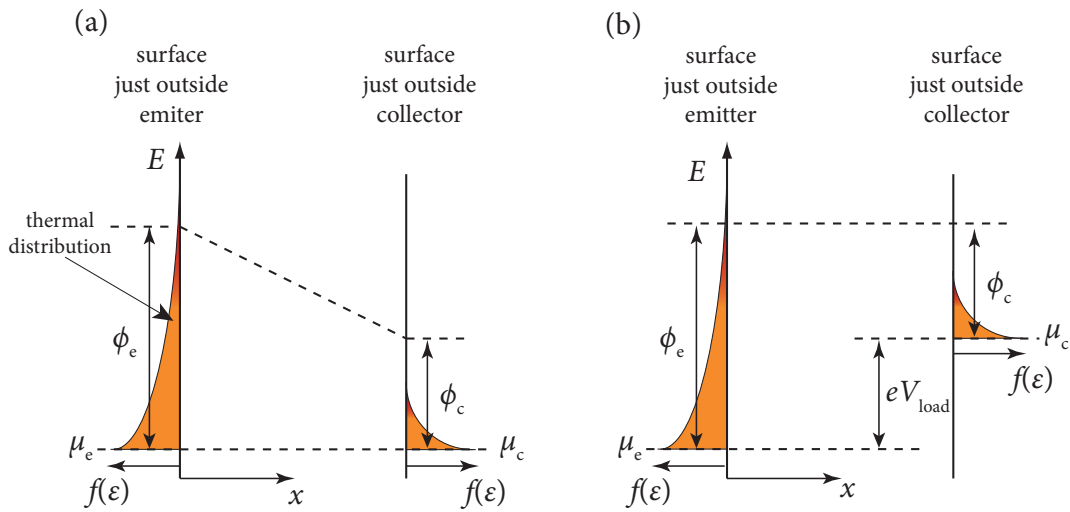


Figure 2.6: Sketch illustrating the consequence of the contact potential on thermionic converters. Emitter and collector with work functions  $\phi_e$  and  $\phi_c$ , respectively, are electrically connected. (a)  $\phi_e$  has to be higher than  $\phi_c$  so that electrons are not accelerated back towards the emitter. (b) When electric power is generated, the load voltage  $V_{load}$  increases the electric potential of the collector. The optimal configuration is obtained when the electric potentials of emitter and collector are equal, so that no electric field exists between them.

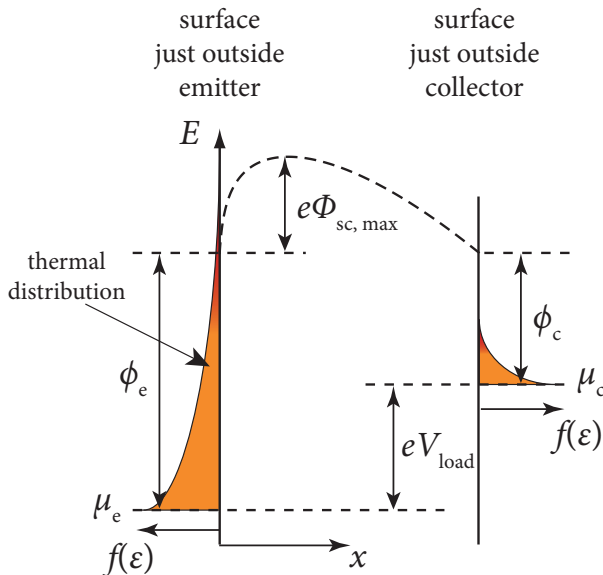


Figure 2.7: The space charge effectively increases the emitter work function in a TIC. Only electrons with an initial kinetic energy of  $\phi_e + e\Phi_{sc,max}$  reach the collector. The space-charge maximum  $\Phi_{sc,max}$  can therefore be treated as an addition to the work function of the emitter.

## 2.4 Electron Emission Phenomena

In this section I will discuss the basic principles of thermionic electron emission, including the emitted current density, the velocity distribution of the electrons and the energy flux. I will further present a method to combine the photoelectric effect with the thermionic emission to increase the emitted current.

### Richardson-Dushman equation

The Richardson-Dushman equation describes the current density emitted from a heated metal surface. To derive the equation, a metal in thermal equilibrium is considered. The spectral density of the electrons is given by the Fermi-Dirac distribution

$$f_{\text{FD}}(\mathbf{v}) = \frac{m_e}{4\pi^3\hbar^3} \frac{1}{\exp\left[\left(\frac{1}{2}m_e v^2 - \mu\right)/(k_B T)\right] + 1}. \quad (2.3)$$

Electrons leaving the metal need to have an energy of least the work function  $\phi$ . Since  $\phi$  is of the order of a few electron volts, their velocity distribution can be approximated by<sup>4</sup>

$$\frac{1}{\exp\left[\left(\frac{1}{2}m_e v^2 + \phi\right)/(k_B T)\right] + 1} \approx \exp\left[-\left(\frac{1}{2}m_e v^2 + \phi\right)/(k_B T)\right].$$

To calculate the current density  $J = nev$  flowing away from the surface, the contributions from all electrons with a positive velocity normal to the metal surface have to be integrated. If the x-direction is chosen as the direction of the current, it follows

$$J_{\text{RD}} = \frac{em_e}{4\pi^3\hbar^3} e^{-\frac{\phi}{k_B T}} \int_0^{\infty} dv_x \int_{-\infty}^{\infty} dv_y \int_{-\infty}^{\infty} dv_z v_x e^{-\frac{m_e v^2}{2k_B T}} = A_{\text{RD}} T^2 e^{-\frac{\phi}{k_B T}}. \quad (2.4)$$

This result is called the Richardson-Dushman [31, 32] equation, with the Richardson-Dushman constant

$$A_{\text{RD}} = \frac{em_e k_B^2}{2\pi^2\hbar^3} = 120 \text{ A}/(\text{cm}^2 \text{ K}^2). \quad (2.5)$$

Figure 2.8 displays the Richardson-Dushman current density plotted as a function of the temperature for different emitter work functions. The graph demonstrates that for materials with work functions typically used in TICs — in the range of 2 eV–3 eV — temperatures of at least 1200 K have to be applied to generate significant emission currents.

The Richardson-Dushman equation is a good approximation for pure metals with a uniform surface. The emitted current density, however, can deviate strongly from this theoretical value, especially for non-metals and inhomogeneous surfaces [33]. Effects like

<sup>4</sup>The fact that velocity distribution of electrons outside a metal surface follows a Maxwell-Boltzmann form has encouraged the belief that the Maxwell-Boltzmann distribution is valid inside a metal, too, and delayed the discovery of the Fermi-Dirac statistic [25].

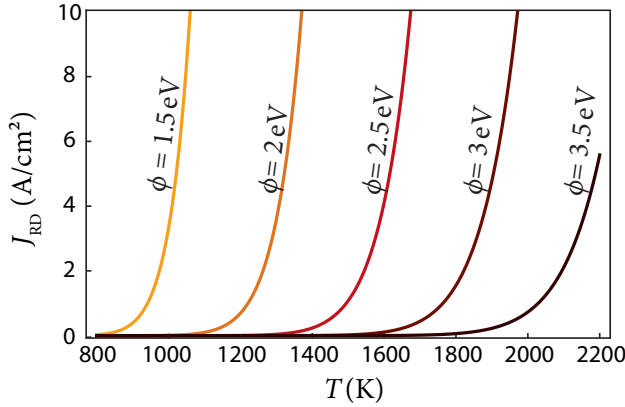


Figure 2.8: Richardson-Dushman current density  $J_{RD}$  as a function of the temperature  $T$  for different material work functions  $\phi$ .

the temperature dependence of the work function, the exact surface structure, the crystallographic plane and electron reflection have to be taken into account. The Richardson-Dushman emission is thus often treated as a phenomenological equation, the modified constant  $A^*$  being determined experimentally.

As an exact formulation of the emission current is not crucial to the investigation of our new concept, I shall not discuss it further here. For a detailed analysis of the emission current and the consequences on thermionic energy converters, please refer, *e.g.*, to references [29] and [33].

### Emission Regimes

The Richardson-Dushman current density represents the saturation value for an emitting metallic surface when no strong accelerating electric fields are applied. The actual measured current, however, depends on the electric field outside the metal, which can be caused, *e.g.*, by the space charge of the emitted electrons or by an externally applied voltage. Depending on the applied electric field, the current density can be divided into different emission regimes, as shown in figure 2.9.

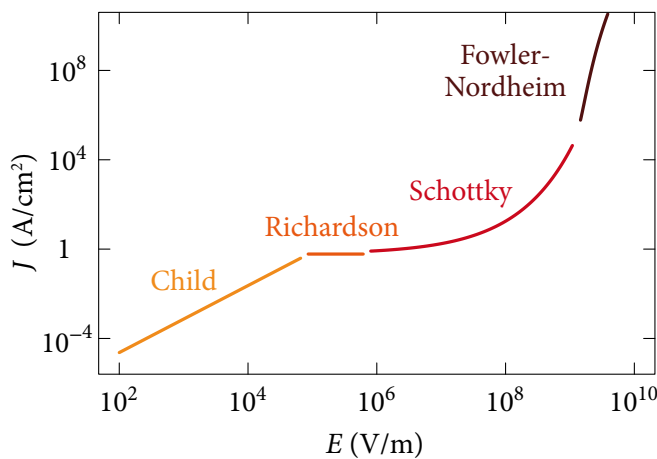


Figure 2.9: Emitted current density  $J$  of a metallic surface as a function of the applied electric field  $E$  for a plane parallel diode configuration with an electrode distance of  $100\ \mu\text{m}$ . Depending on the strength of  $E$ , the qualitative behavior of  $J(E)$  changes. This behavior can be divided into different regimes, which are indicated by the names 'Child', 'Richardson', 'Schottky', and 'Fowler-Nordheim'. Data calculated by Stefan Meir [3].

I will discuss now the emission regimes using the example of a plane-parallel diode. When no electric field is applied, the space charge of the emitted electrons dominates the current density. Only a small fraction of the emitted electrons reaches the second electrode.

The space charge can be reduced by applying an accelerating electric field. The current density is described by the Child-Langmuir Law [34, 35]

$$J = \frac{4}{9}\epsilon_0 \left( \frac{2e}{m_e} \right)^{\frac{1}{2}} \frac{E^{\frac{3}{2}}}{d_{ec}^{\frac{1}{2}}}, \quad (2.6)$$

where  $d_{ec}$  represents the distance between the emitter and collector electrodes.

When the electric field is strong enough to completely suppress the space charge, the current density reaches a saturation level, given by the Richardson-Dushman equation.

Increasing the electric field beyond about  $10^6$  V/m further increases the emitted current. The work function is reduced by the electric field, a process called Schottky effect [36]. By superposition of the electric field and the work function, it can be shown that  $\phi$  is reduced by [29]

$$\Delta\Phi = e \left( \frac{eE}{4\pi\epsilon_0} \right)^{\frac{1}{2}}. \quad (2.7)$$

The emitted current density is derived by modifying the Richardson-Dushman equation accordingly to consider the contribution of  $\Delta\Phi$ , yielding

$$J = A_{RD} T^2 e^{-\frac{\phi - \Delta\Phi}{k_B T}} = A_{RD} T^2 \exp \left[ -\frac{\Phi}{k_B T} \right] \exp \left[ \frac{e(eE/4\pi\epsilon_0)^{\frac{1}{2}}}{k_B T} \right]. \quad (2.8)$$

For electric fields larger than  $10^8$  V/m, electrons start tunneling through the potential barrier into the vacuum. Thereby, electrons without enough kinetic energy to overcome the work function leave the metal and contribute to the emitted current. This regime is called Fowler-Nordheim Emission [37]. This process does not play a role for conventional TICs, but it may be exploited, for example, when using a thermionic energy converter for refrigeration.

### Photon-Enhanced Thermionic Emission

Recently, a group in Stanford [9] investigated the possibility of enhancing thermionic electron emission by exploiting the photonic character of sunlight [38] for thermionic energy conversion. Photon-enhanced thermionic emission (PETE) combines the photoelectric effect [39] with thermionic emission, leading to an increased emitted current density.

In PETE, a p-type semiconductor is used as the emitter. Electrons in the valence band are first excited by solar radiation into the conduction band, where they thermalize and diffuse through the material. After thermalization, the electron energies in the semiconductor are distributed according to the quasi-electrochemical potential  $\mu'$  rather than to

the electrochemical potential  $\mu$ . As indicated in figure 2.10,  $\mu'$  is located just below the conduction band edge. Electrons in the semiconductor have a thermal energy distribution that is similar to the thermal energy distribution in a metal, but their average energy is higher.

Electrons reaching the emitter surface with enough energy to leave the semiconductor are emitted and contribute to the current density. These electrons were excited by both the photon energy to overcome the band gap and the thermal energy to leave the emitter. The current density achieved is higher than for normal thermionic emission.

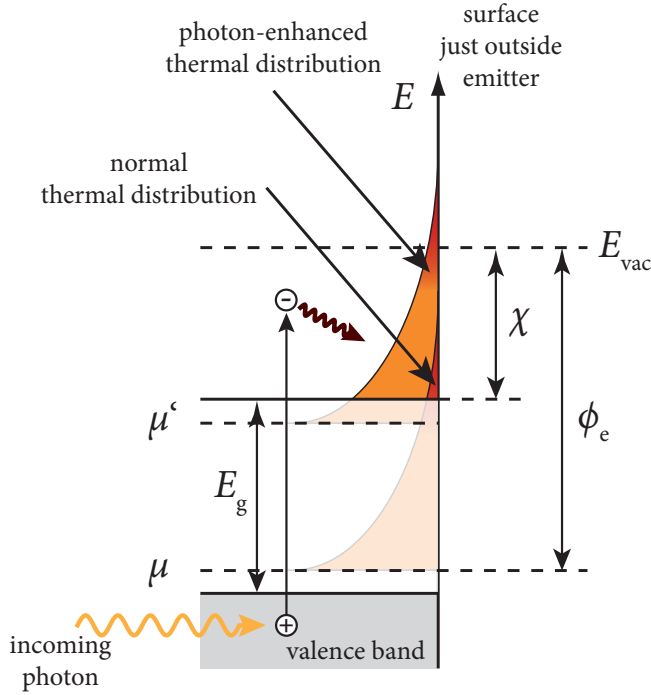


Figure 2.10: Schematic diagram of the processes contributing to the photon-enhanced thermionic emission, following reference [9]. A p-type semiconductor with a band gap  $E_g$  is used as emitter. Electrons in the valence band are excited by photons with sufficient energy into the conduction band, where they thermalize. To leave the emitter surface, the electrons need enough energy to overcome the electron affinity  $\chi$ , which is given by the difference between the conduction band minimum and the vacuum energy level  $E_{\text{vac}}$ . Through the photoelectric excitation, the thermal energy contribution is modified as shown. The electrochemical potential  $\mu$  and the quasi-electrochemical potential  $\mu'$  are indicated, too.

The emitted current density can be calculated analogous to the Richardson-Dushman equation and is given by

$$J = en\langle v_x \rangle e^{-\chi/k_B T}, \quad (2.9)$$

where  $n$  is the electron density in the conduction band and  $\langle v_x \rangle$  the average velocity perpendicular to the surface [9]. The electron affinity  $\chi$  indicates the energy difference between the conduction band minimum and the vacuum energy level  $E_{\text{vac}}$  (see figure 2.10). The parameters  $n$ ,  $\langle v_x \rangle$  and  $\chi$  depend on material characteristics, such as the effective electron mass  $m^*$ , the band gap  $E_g$  or the electrochemical potential  $\mu$ . The conduction-band population  $n$  has to be calculated by balancing the rate of charge carrier generation, including photoelectric and thermal excitation, recombination and thermionic emission.

Although the current density is increased by directly using the photon energy  $h\nu$ , the energy distribution of the emitted electrons is the same as for conventional thermionic emission, following a Maxwell distribution.

For a detailed investigation and analysis of the photon-enhanced emission and the consequences and possibilities for thermionic energy conversion, please refer to reference [9].

### Energy Flux

Every electron emitted from a metallic surface carries a thermal energy, thereby cooling the emitting surface. The energy carried away by the emitted electrons can be calculated by integrating the contributions of all electrons with enough energy to overcome the work function  $\phi$  — analogous to the calculation of the emitted current density. The energy flux  $\omega$  describes the energy carried away by the electrons per unit area. It is given by

$$\omega = \int_0^{\infty} dv_x \int_{-\infty}^{\infty} dv_y \int_{-\infty}^{\infty} dv_z \left( \phi + \frac{m_e v^2}{2} \right) v_x f_{\text{FD}}(\mathbf{v}) = \frac{J_{\text{RD}}}{e} (2k_B T + \phi). \quad (2.10)$$

### Velocity Distribution of Emitted Electrons

As shown earlier, thermally emitted electrons follow a distribution with a Maxwell-Boltzmann form. The distribution can be approximated by [29]

$$f_h(\mathbf{v}) = \begin{cases} 2 \left( \frac{m_e}{2\pi k_B T} \right)^{3/2} e^{-\frac{m_e v^2}{2k_B T}} & v_x \geq 0 \\ 0 & v_x < 0 \end{cases}. \quad (2.11)$$

Since the contribution of all electrons with  $v_x < 0$  is zero, this distribution is often called ‘Half-Maxwellian’. The mean velocity in x-direction is given by  $\bar{v}_x = \sqrt{2k_B/m\pi}$ , the mean kinetic energy in x-direction by  $\bar{E}_{\text{kin},x} = 1/2k_B T$ .

When a space-charge potential is considered, only electrons with sufficient initial kinetic energy overcome the space-charge maximum  $\Phi_{\text{sc,max}}$ . However, these electrons also follow a ‘Half-Maxwellian’ distribution with the same mean energy and same mean velocity as before. Again, the space-charge potential acts as an effective work function.

## 2.5 Ideal Output Characteristics and Efficiency

In an ideal thermionic converter the space charge is assumed to be absent. Its influence on the performance of the TIC is therefore completely neglected. The calculation of the ideal output characteristics and the ideal efficiency represent an upper limit for all thermionic energy converters. In this context, the basic loss mechanisms and fundamental processes can be understood.

In chapter 6.2, I will calculate the efficiency of our newly developed model based on the principles presented here.

### Current Density and Output Power of an Ideal Thermionic Energy Converter

When no space charge is present, all electrons evaporated from the emitter reach the collector, as long as the electric potential of the collector is smaller or equal to the potential of the emitter — *i.e.*  $\phi_c + eV_{\text{load}} \leq \phi_e$ . In this case, the current density is described by the Richardson-Dushman equation.

If  $\phi_c + eV_{\text{load}} > \phi_e$ , only electrons with sufficient initial energy reach the collector. Since the energy distribution of the emitted electrons follows a Maxwellian form, the current density  $J$  decreases exponentially for increasing load voltage  $V_{\text{load}}$ . Figure 2.5 displays the relative potentials for these different cases.

The output power  $P_{\text{load}}$  is given by

$$P_{\text{load}} = JV_{\text{load}}. \quad (2.12)$$

It increases linearly with  $V_{\text{load}}$ , as long as  $\phi_c + eV_{\text{load}} \leq \phi_e$ . The output power reaches a maximum for

$$eV_{\text{load}} = \phi_e - \phi_c, \quad (2.13)$$

because the current density decreases exponentially for higher  $V_{\text{load}}$ . Equation (2.13) therefore indicates the optimal converter configuration (figure 2.12).

Figure 2.11 shows the current density and the output power density as functions of  $V_{\text{load}}$  for an ideal TIC.

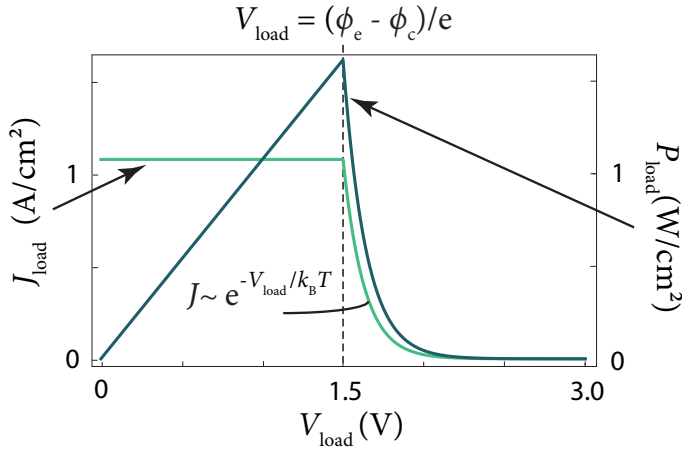


Figure 2.11: Current density  $J$  and output power density  $P_{\text{load}}$  plotted as functions of the load voltage  $V_{\text{load}}$  for an ideal TIC. The ideal output power reaches a maximum for  $V_{\text{load}} = \phi_e - \phi_c$ . The typical parameters  $\phi_e = 2.5$  eV,  $\phi_c = 1$  eV and  $T = 1500$  K were used for this example.

The output characteristics are slightly modified, if back emission from the collector is included [6]. However, the shift in the load voltage defining the optimal output configuration (2.13) is small and can be neglected.

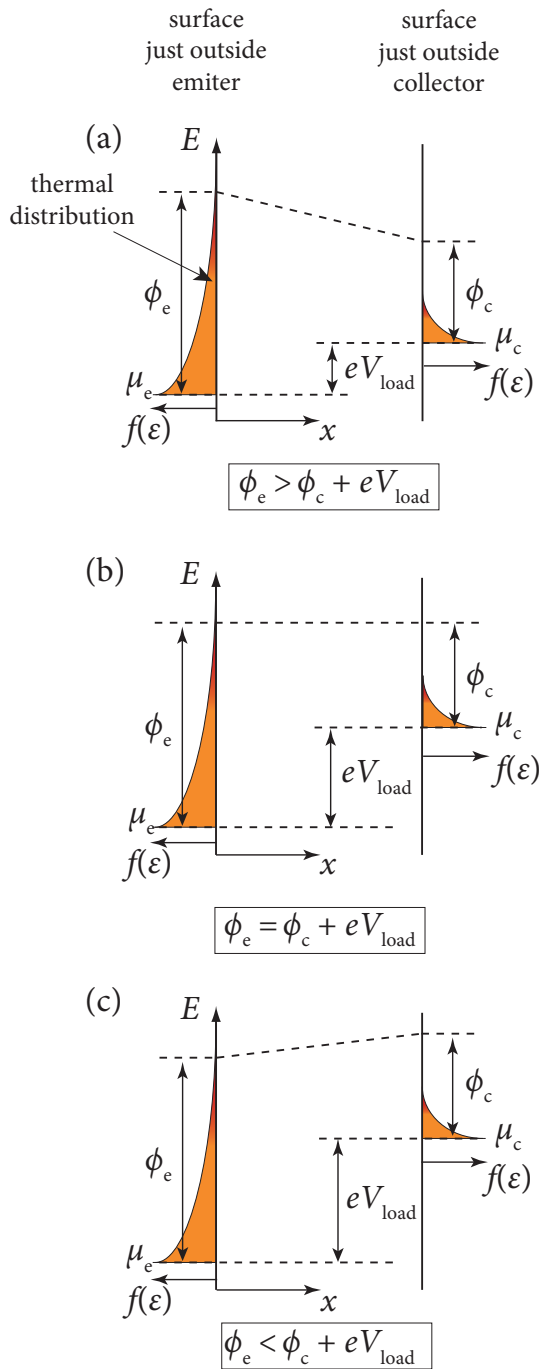


Figure 2.12: Electric potentials of emitter and collector shown for different load voltages  $V_{\text{load}}$  for an ideal thermionic energy converter. The inter-electrode potential is indicated by a dashed line. (a)  $V_{\text{load}}$  is chosen so that the electric potential of the collector is smaller than the potential of the emitter. All electrons from the emitter reach the collector. (b) Emitter and collector are on the same potential. The ideal output power reaches a maximum for this configuration. (c) When  $V_{\text{load}}$  is further increased, only electrons with sufficient initial energy reach the collector. The current density and the output power are decreased.

### Efficiency of an Ideal Thermionic Energy Converter

Based on the preceding considerations, I will now calculate the efficiency of an ideal thermionic energy converter. The ideal efficiency constitutes an upper limit for all thermionic energy converters. Only the fundamental loss mechanisms, present in every converter, are considered. If a certain type of converter is studied, *e.g.*, a vapor diode, its efficiency can be determined by including the additional loss channels into the calculations discussed below.

The calculation of the ideal efficiency  $\eta$  is based on the considerations presented in references [6,40–43]. Additionally, I will include the influence of the collector back emission.

The first step of calculating the efficiency is to quantify the power densities transferred to and from the system and to determine the load current. Figure 2.13 illustrates the power fluxes and current densities in an ideal TIC, while figure 2.14 displays the electric potentials. All power quantities considered here are power densities, normalized to the emitter surface area  $A_e$ .

The load-current density  $J_{\text{load}}$  is determined by the electrons evaporated from the emitter  $J_e$  and the back emission from the collector  $J_{\text{be}}$ , given by

$$J_{\text{load}} = J_e - J_{\text{be}}, \quad (2.14)$$

with the current densities

$$J_e = A_{\text{RD}} T_e^2 e^{-\frac{\phi_e}{k_B T_e}} \quad \text{and} \quad J_{\text{be}} = A_{\text{RD}} T_c^2 e^{-\frac{\phi_c}{k_B T_c}}. \quad (2.15)$$

The power output depends on the load voltage  $V_{\text{load}}$ , which can be expressed in terms of  $\phi_e$ ,  $\phi_c$  and  $V_{\text{lwe}}$ , as illustrated in figure 2.13. With  $V_{\text{lwe}} = R_{\text{lwe}} J_{\text{load}} A_e$ ,

$$P_{\text{load}} = J_{\text{load}} V_{\text{load}} = J_{\text{load}} \left( \frac{\phi_e - \phi_c}{e} - J_{\text{load}} A_e R_{\text{lwe}} \right) \quad (2.16)$$

is obtained.

To achieve high efficiencies, the collector must be cold. The lead wire connecting the collector to the load resistance can therefore be optimized for a low electric resistivity, neglecting the heat transport away from the collector. Consequently, the ohmic loss in the collector lead wire is small. I will therefore neglect the voltage drop in the collector lead wire.

The heat delivered to the emitter is  $Q_{\text{in}}$ . As we consider steady-state situations, it is chosen so that the emitter temperature  $T_e$  remains constant at all times. The heat removed from the emitter consists of three contributions: the electron cooling  $P_{\text{ec}}$ , the heat radiation  $P_{\text{r}}$  and heat transport through the lead wire  $P_{\text{lwe}}$ .

In practical converters, further heat loss channels exist, such as heat transferred by the structure or transported by gas molecules or electron collisions. However, these losses can, in principle, be kept small. The heat transport by gas molecules as well as electrons collisions do, however, play a role in vapor diodes.

## 2 Introduction to Thermionic Energy Conversion

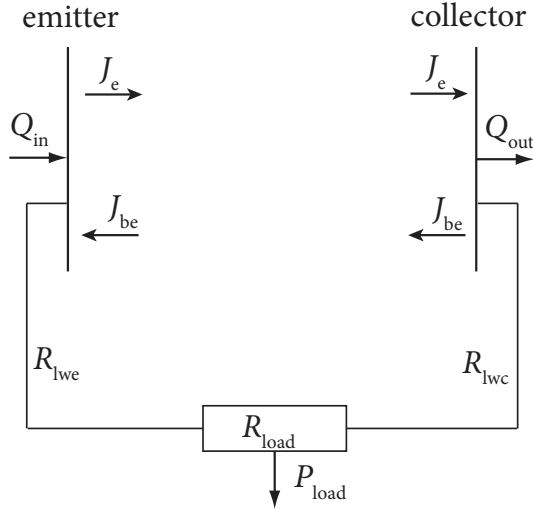


Figure 2.13: Sketch showing the contributions relevant to calculating the ideal efficiency of a TIC. The heat quantities inserted into and rejected from the system are indicated as  $Q_{in}$  and  $Q_{out}$ , respectively, the current densities of emitter and collector as  $J_e$  and  $J_{be}$ , the resistance of the lead wires connecting emitter and collector to the load resistance as  $R_{lwe}$  and  $R_{lwc}$ , respectively.

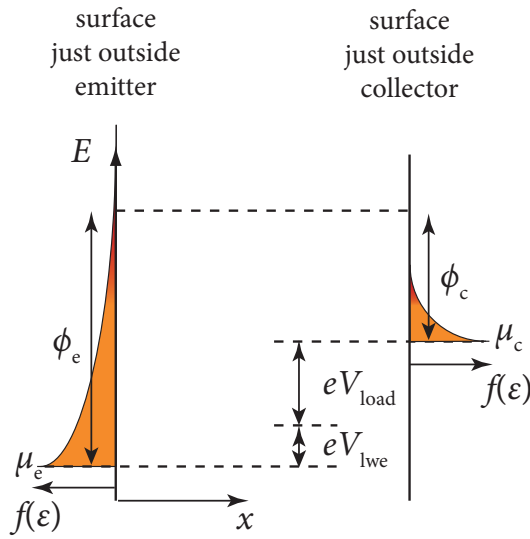


Figure 2.14: Sketch showing the different electric potentials in an ideal TIC, including the voltage drop due to the emitter lead wire  $V_{lwe}$ . The collector lead wire is not considered here.

The electron cooling term describes the energy carried away by the electrons. Using the energy flux according to equation (2.10), including the contribution of the collector back emission, leads to

$$P_{ec} = \frac{J_e}{e} (\phi_e + 2k_B T_e) - \frac{J_{be}}{e} (\phi_e + 2k_B T_c). \quad (2.17)$$

The heat loss due to radiation is described by the Stefan-Boltzmann law. Again, the contribution from the collector has to be taken into account, yielding

$$P_r = \varepsilon_{eff} \sigma (T_e^4 - T_c^4), \quad (2.18)$$

with the Stefan-Boltzmann constant  $\sigma = 5.67 \times 10^{-8} \text{ J s}^{-1} \text{ m}^{-2} \text{ K}^{-4}$  and the effective emissivity of the system  $\varepsilon_{\text{eff}}$ . For practical converters,  $\varepsilon_{\text{eff}}$  usually lies in the range of 0.1–0.2 [24].

The heat transported through the emitter lead wire can be determined by solving the one-dimensional heat flow equation. If no work is performed, it is given by

$$\frac{\partial T}{\partial t} - \alpha \frac{\partial^2 T}{\partial x^2} = 0, \quad (2.19)$$

where  $\alpha$  represents the thermal diffusivity  $\alpha = \kappa/(c_{\text{sp}}\rho)$ , with the thermal conductivity  $\kappa$ , the specific heat capacity  $c_{\text{sp}}$  and the electrical resistivity  $\rho$ .

For a TIC, only the stationary case is relevant. However, a current flowing through the lead wire performs work by heating the wire. Accounting for this work — the Joule heating — the stationary heat equation is given by

$$\frac{d}{dx} \kappa \frac{dT}{dx} = -J_{\text{load}}^2 \frac{A_e^2}{A_{\text{lwe}}^2} \rho. \quad (2.20)$$

The heat transport is obtained by integrating this equation twice and using the Wiedemann-Franz law

$$\frac{\kappa\rho}{T} = \frac{\pi^2}{3} \left( \frac{k_{\text{B}}}{e} \right)^2 \equiv L, \quad (2.21)$$

with the Lorenz number  $L = 2.44 \times 10^{-8} \text{ W/ K}^2$ .

The temperature  $T$  in formula (2.21) is the average temperature in the lead wire, given by  $T = \frac{1}{2}(T_e - T_0)$ .  $T_0$  is the temperature of the electrical load, which is assumed to be at room temperature  $T_0 = 300 \text{ K}$ .

The heat transfer through the emitter lead wire is then finally given by

$$P_{\text{lwe}} = \frac{1}{2} \frac{L}{R_{\text{lwe}} A_e} (T_e - T_0)^2 - \frac{1}{2} J_{\text{load}}^2 A_e R_{\text{lwe}}. \quad (2.22)$$

The first part represents the heat transported away from the emitter through the lead wire. The second part describes the consequence of the Joule heating, which returns heat to the emitter.

Summing up all the contributions leads to the ideal efficiency of

$$\eta = \frac{P_{\text{load}}}{P_{\text{ec}} + P_{\text{r}} + P_{\text{lwe}}}. \quad (2.23)$$

The efficiency  $\eta$  depends on various parameters —  $\phi_e$ ,  $T_e$ ,  $\phi_c$ ,  $T_c$ ,  $R_{\text{lwe}}$  and  $\varepsilon_{\text{eff}}$ . This makes the analysis of the maximal efficiency challenging, especially because the different terms are intercorrelated.

One approach, which has been used in the literature, is to define a collector work function  $\phi_c$  and determine the collector temperature  $T_c$  accordingly as a first step. As I discussed earlier, and is made evident by equation (2.16), a low collector work function leads

to a high output power. For a specific value of  $\phi_c$ , the optimal collector temperature can be determined. A high  $T_c$  leads to a heat transfer back to the emitter through radiation and electron heat transport. However,  $T_c$  has an upper limit. It has to be low enough to prevent significant back emission from the collector, as a strong back emission is detrimental for an efficient TIC. Rasor [42] showed that the optimal collector temperature can be determined using the equation

$$T_c/\phi_c \approx (640 \pm 6\%) \text{ K/V.} \quad (2.24)$$

If a  $T_c$ -value close to the calculated optimal value is being used, the back emission can, in a good approximation, be neglected.

Equation (2.24) further illustrates that the collector work function has a lower limit for efficient TICs, which is caused and determined by the back emission. If room temperature ( $T_0 = 300 \text{ K}$ ) is considered as the minimum possible collector temperature,  $\phi_c$  needs to exceed approximately 0.5 eV.

In a next step, the optimal lead geometry is determined. It can be shown that the lead resistance  $R_{lwe}$  is a function of  $\eta$ . The optimal lead characteristics can be calculated analytically [6, 42, 43].

After defining the effective emissivity  $\varepsilon_{\text{eff}}$ , the ideal efficiency can be calculated in dependence of  $T_e$  and  $\phi_e$ .

One important result of this analysis is that for a chosen collector work function  $\phi_c$ , there always exists an optimal value of the emitter work function  $\phi_e$ . A low emitter work function enables a high current density. However, the energy the emitted electrons carry, and that can be converted into the electrical power, increases with  $\phi_e$ .

In my thesis, I will use a different approach to determine the ideal efficiency. I will consider all parameters mentioned above, including the collector back emission. First, the efficiency for different values of all parameters is calculated, except for the lead wire resistance. After calculating  $\eta$ , the optimal value for  $R_{lwe}A_e$  is evaluated numerically. From this, the optimal lead wire resistance can be obtained, depending on the emitter surface  $A_e$ .

This procedure generates large datasets. However, the optimal efficiency can be determined by identifying the maximum values within the calculated data. The numerical calculations have been performed by Stefan Meir. For a more detailed explanation, please refer to reference [3].

Figure 2.15 shows the optimized efficiency for an ideal TIC as a function of the emitter temperature for different values of the collector work function. Efficiencies greater than 60 % can be achieved with realistic parameter sets of  $\phi_e \approx 3 \text{ eV}$ ,  $T_e = 2500 \text{ }^\circ\text{C}$ ,  $\phi_c = 0.55 \text{ eV}$  and  $T_c = 100 \text{ }^\circ\text{C}$ .

The dashed lines represent the efficiencies if the current density was limited to  $10 \text{ A/m}^2$ . In an ideal TIC, the space charge is assumed to be absent. However, this could be possible only up to a certain current density. We chose  $10 \text{ A/m}^2$  as an example.

Figure 2.16 shows the share of the different contributions, the electron cooling  $P_{ec}$ , the heat radiation  $P_r$  and heat transport through the lead wire  $P_{lwe}$ , in the total heat removed from the emitter. The results show that for high efficiencies, the energy loss on the emitter

## 2.5 Ideal Output Characteristics and Efficiency

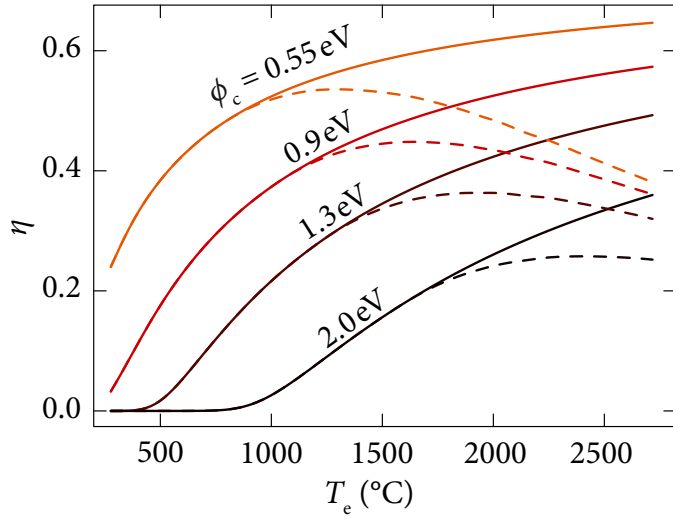


Figure 2.15: Ideal efficiency  $\eta$  as a function of emitter temperature  $T_e$  for different collector work functions  $\phi_c$ . The emitter work function  $\phi_e$  and the collector temperature  $T_c$  have been optimized to yield the highest efficiency. The dashed lines represent efficiency values for the case that only current densities up to  $10 \text{ A/m}^2$  were possible. For  $\epsilon_{\text{eff}}$  a value of 0.1 was used [24]. Data calculated by Stefan Meir [3].

is mostly due to the energy the electrons need to overcome the emitter work function  $\phi_e$ . The other contributions, including the thermal energy of the electrons, yield significantly smaller contributions.

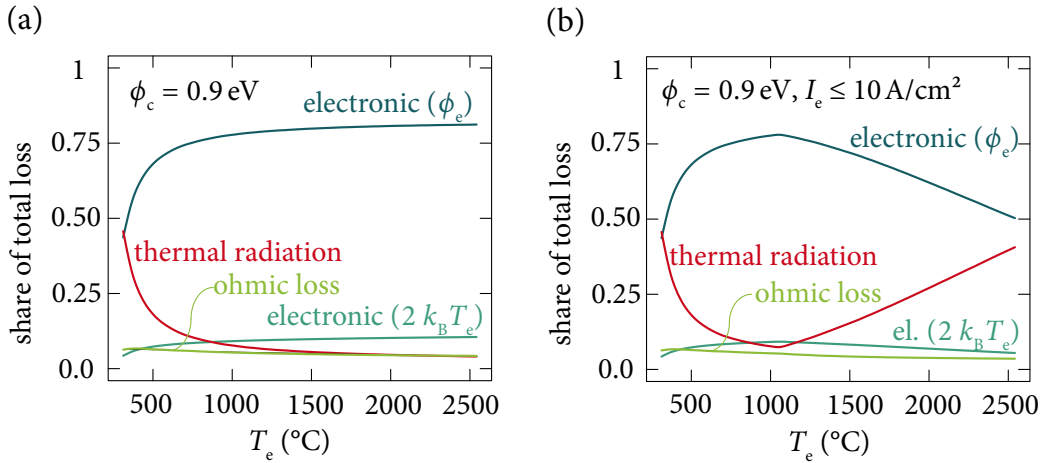


Figure 2.16: Share in the total heat removed from the emitter of the electron cooling, the heat radiation and the heat transported through the lead wire as functions of the emitter temperature  $T_e$ . The electron cooling  $P_e$  is divided into the two parts: the first part ( $\phi_e$ ) indicates the energy the electrons need to overcome the work function; the second part ( $2k_B T_e$ ) indicates the thermal energy the electrons carry; compare equation (2.17). The data correspond to the curves shown in figure 2.15 for a collector work function of 0.9 eV. Panel (a): the current density is defined by the Richardson-Dushman equation (continuous line in figure 2.15). For high emitter temperatures, the electron cooling yields the greatest contribution, as the current density increases exponentially with  $T_e$ . Panel (b): The current density is limited to  $10 \text{ A/cm}^2$ . As soon as this value is reached, only thermal radiation increases for increasing  $T_e$ . The heat loss through the radiation therefore becomes important in this case. Data calculated by Stefan Meir [3].

Equation (2.23), defining the ideal efficiency, and the obtained results, are consistent with the results in the literature [6, 40–43].

### Carnot Efficiency and the Ultimate Efficiency Limit

To estimate the ultimate physical limit for the conversion efficiency, only the processes directly involved into the energy conversion have to be considered. Assuming the heat transfer through the connection wires and radiation and ohmic losses could be prevented, only the electronic processes, the electron emission and concomitant electron cooling, remain. The resulting efficiency is always smaller than  $\eta_{\text{Carnot}}$  [6, 44].

Further assuming the electrons could be emitted only at the vacuum energy level, without any thermal distribution, the efficiency would be given by

$$\eta = \frac{J_{\text{load}}(\phi_e - \phi_c)}{J_{\text{load}}\phi_e} = \frac{\phi_e - \phi_c}{\phi_e} = 1 - \frac{\phi_c}{\phi_e}, \quad (2.25)$$

for  $J_{\text{load}} > 0$ . Equation (2.25) constitutes the ultimate limit for thermionic energy conversion.  $\phi_c$  has a lower limit and cannot approach zero, as the collector back emission would otherwise dominate the current density. For  $J_{\text{load}} \rightarrow 0$ , the efficiency approaches the Carnot efficiency. However, no output power would be generated.

### Efficiency of a TIC combined with Photon-Enhanced Thermionic Emission

When the emission current is enhanced by PETE, the energy converter is no longer a pure heat engine. It is therefore not limited by the Carnot efficiency. Considering the arguments leading to the ultimate efficiency limit, it is evident that the conversion efficiency can be higher than  $\eta_{\text{Carnot}}$ , if the load current is increased without increasing the emitter temperature.

Remarkably, equation (2.25) still constitutes the upper limit for the conversion efficiency. In the case of PETE, however, the collector work function has a smaller lower limit than conventional TICs.

### Efficiency in a Combined Cycle

If a TIC is used as a topping cycle, the heat rejected from the collector is used to power a second heat engine. For a high efficiency of the combined cycle, the collector is not operated at low temperatures, because this would reduce the efficiency of the secondary heat engine. As a consequence, the efficiency of the TIC cannot be as high as in uncoupled operation. To achieve a high overall efficiency, the TIC has to be combined with a heat engine that is specifically efficient in the low temperature range. Good examples are steam turbines or Stirling Motors [45–47].

To calculate the efficiency  $\eta_{\text{tot}}$  of the entire system, the heat rate rejected from the collector  $Q_{\text{out}}$  has to be determined.  $Q_{\text{out}}$  is equivalent to the heat transfer to the collector, which consist of three parts: the electron heating  $P_{\text{eh}}$ , the heat radiation  $P_r$  and the heat transport through the collector lead wire  $P_{\text{lwc}}$ .

The contributions are derived analogous to the previous calculations, yielding

$$P_{\text{eh}} = \frac{J_e}{e}(\phi_c + 2k_B T_e) - \frac{J_{\text{be}}}{e}(\phi_c + 2k_B T_c), \quad (2.26)$$

$$P_r = \varepsilon_{\text{eff}} \sigma (T_e^4 - T_c^4), \quad (2.27)$$

$$P_{\text{lwc}} = -\frac{L}{2R_{\text{lwc}}A_e}(T_c - T_0)^2 + \frac{1}{2}(J_e - J_{\text{be}})^2 A_e R_{\text{lwc}}, \quad (2.28)$$

$$Q_{\text{out}} = P_{\text{eh}} + P_r + P_{\text{lwc}}. \quad (2.29)$$

The power generated by the secondary heat engine with the efficiency  $\eta_s$  is given by

$$P_{\text{heat engine}} = Q_{\text{out}} \eta_s. \quad (2.30)$$

As the heat transfer from the collector is essential in the combined cycle, the collector lead wire connecting has to be optimized for both current and heat transport. Therefore, the ohmic loss in the collector lead wire can not be neglected. The load voltage has to be modified accordingly to

$$V_{\text{load}} = \frac{\phi_e - \phi_c}{e} - J_{\text{load}} A_e (R_{\text{lwe}} + R_{\text{lwc}}). \quad (2.31)$$

This leads to an overall efficiency of

$$\eta_{\text{tot}} = \frac{J_{\text{load}} V_{\text{load}} + Q_{\text{out}} \eta_s}{P_{\text{ec}} + P_r + P_{\text{lwe}}}. \quad (2.32)$$

Figure 2.15 shows the efficiency of a TIC used as a topping cycle in combination with a steam turbine or a Stirling motor. The steam turbine is considered to work with an inlet temperature of 400 °C and an efficiency of 35 %, whereas the Stirling Motor is considered to work with an inlet temperature of 700 °C and an efficiency of 35 %. These values are taken from references [45, 46]. The overall efficiency exceeds 60 % for both systems, much larger than the 35 % achieved only with the steam turbine or the Stirling motor.

A distinct advantage of using the TIC as a topping cycle is that the collector work function does not have to be as low as for the uncoupled operation. The efficiencies shown in figure 2.17 are obtained for an optimized collector work function of 1.2 eV for the Stirling Motor and 0.8 eV for the steam turbine. For higher inlet temperatures of the secondary heat engine,  $\phi_c$  can have even higher values.

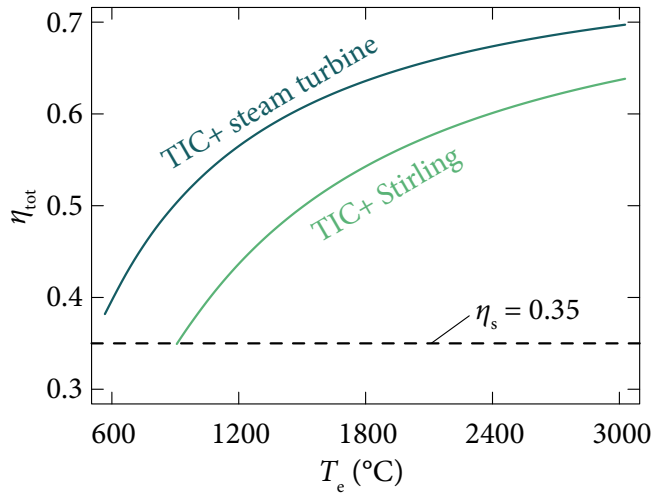


Figure 2.17: Overall efficiency  $\eta_{\text{tot}}$  of a combined cycle system with a TIC as topping cycle in combination with a steam turbine or a Stirling Motor. The steam turbine and the Stirling Motor both work with an efficiency of  $\eta_s = 35\%$  and inlet temperatures of  $400^\circ\text{C}$  and  $700^\circ\text{C}$ , respectively. The optimal collector work functions for the combined systems are  $0.8\text{ eV}$  and  $1.2\text{ eV}$ , respectively.

## 2.6 Analogy and Comparison of Thermionic and Thermoelectric Converters

Thermoelectric energy converters have drawn much interest in recent years. They have been seen as a valuable addition for renewable and clean energy generation as well as a chance to increase the efficiency of existing conversion processes, *e.g.*, by utilizing waste heat in car combustion engines. Below I will draw analogies between thermionic and thermoelectric devices and show that the physical principles of both techniques are very similar. It will become evident that thermionic converters offer the same possibilities and advantages as thermoelectric devices, while operating at significantly higher efficiencies.

Remarkably, the advantages of thermionic over thermoelectric converters have already been pointed out by Ioffe in 1957 in his book on semiconductor thermoelements [48], in which he proposed a vacuum thermoelement based on thermionic emission.

Thermoelectric devices are based on the Seebeck effect. A temperature gradient induces a voltage — called the Seebeck voltage or Seebeck coefficient  $\alpha$  — in a metal or semiconductor. The coefficient  $\alpha$  is a material constant, which depends strongly on the band structure of the material. Metals usually have very low Seebeck voltages — in the range of some  $\mu\text{V/K}$  —, whereas semiconductors can reach values in the range of  $100\ \mu\text{V/K}$  [48]. The thermo voltage is a consequence of diffusion currents of hot and cold charge carriers, and can be greatly enhanced by doping in a semiconductor. Thermoelectric energy converters are usually built of thermocouples that consist of pairs of n-type and p-type semiconductors (figure 2.18).

The efficiency of thermoelectric energy converters is given by [50]

$$\eta = \eta_{\text{Carnot}} \frac{\sqrt{ZT + 1} - 1}{\sqrt{ZT + 1} + (T_{\text{cold}}/T_{\text{hot}})}. \quad (2.33)$$

## 2.6 Analogy and Comparison of Thermionic and Thermoelectric Converters

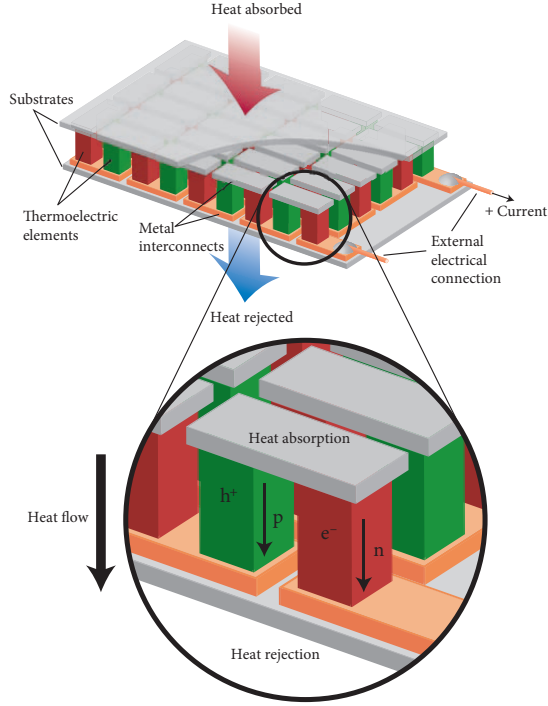


Figure 2.18: Sketch of a thermoelectric cell, consisting of several thermocouples connected in series. Each thermocouple consists of a  $p$ -type and an  $n$ -type semiconductor. From [49]. Reprinted with permission from AAAS.

The  $Z$  factor is defined by

$$Z = \frac{\alpha^2}{\kappa\rho}, \quad (2.34)$$

where  $\kappa$  is the thermal conduction and  $\rho$  the resistivity of the material. The  $Z$  factor is often called the figure of merit, as a high value indicates a high conversion efficiency. A high thermal conduction lowers the efficiency due to the heat transport from the hot to the cold end, while a low resistivity is crucial for the transport of charge carriers. The efficiency of a thermoelectric energy converter approaches  $\eta_{\text{Carnot}}$  for  $ZT \rightarrow \infty$  [51].

$\kappa$  can be divided into an electronic and a lattice contribution  $\kappa = \kappa_e + \kappa_l$ . Using the Wiedemann-Franz law (2.21) for the electronic part yields [49]

$$ZT = \frac{\alpha^2(q/k_B)^2}{L(1 + \kappa_l/\kappa_e)}. \quad (2.35)$$

For a thermocouple, the  $ZT$  factor is expanded to include both branches with the positive Seebeck coefficient  $\alpha_+$  and the negative Seebeck coefficient  $\alpha_-$

$$ZT = \left( \frac{\alpha_- - \alpha_+}{\sqrt{\kappa_- \rho_-} + \sqrt{\kappa_+ \rho_+}} \right)^2 T. \quad (2.36)$$

‘Best practice’ thermoelectric devices reach  $ZT$  values close to 1, while a value of 2 seems realistic — though ambitious — in the near future [52]. This results in an efficiency be-

tween 15 % and 30 % of the Carnot efficiency, respectively. A value of 40 % may be achievable with optimized thermoelectric materials.

These  $ZT$  values are only valid in specific temperature ranges. The suitable materials therefore vary for different applications and temperatures. Thermoelectric materials with sufficiently high  $ZT$  values for temperatures up to about 1000 °C are known [49].

The efficiencies can be compared directly to the values possible with thermionic devices (compare figure 2.15), revealing that the possible efficiencies of thermionic converters are significantly larger.

An alternative for comparing both techniques is to explore their physical analogies. The fundamental physical principles of thermionic and thermoelectric energy converters are very similar. Both are heat engines that convert thermal energy into electrical energy through the transport of charge carriers from the hot to the cold end of the devices, thereby inducing a voltage difference. In both converters, the charge carriers need to overcome an energy barrier to reach the other end — in a semiconductor the band gap  $E_g$ , in a thermionic energy converter the emitter work function  $\phi_e$ .

One significant difference, however, is the actual heat transport from the hot to the cold part aside from the electronic contribution. In thermoelectric energy converters, heat is transported through phononic processes in the bulk material. In thermionic energy converters, the two electrodes are separated by vacuum. The dominant heat transport in a TIC, the Stefan-Boltzmann radiation, is significantly smaller than the lattice heat transport in the temperature ranges considered.

Moyzhes and Geballe [4] make use of these analogies to determine an effective  $ZT$  factor for thermionic converters. They calculate the Seebeck voltage of a TIC, obtaining values of the order of 1500  $\mu\text{V}/\text{K}$ , resulting in a  $ZT$  value of 150–200. As a next step, they consider the thermionic converter as a vacuum branch of a thermoelectric couple. They find the  $ZT$  factor of the total device to be at least about 40, far exceeding the values of thermoelectric materials. Also accounting for the Stefan-Boltzmann radiation in a TIC, the obtained  $ZT$  values result in efficiencies in the range  $0.55 \eta_{\text{Carnot}} - 0.65 \eta_{\text{Carnot}}$ . This efficiency could be even higher, as Moyzhes and Geballe only consider collector temperatures between 800 K–900 K. Lower values of  $T_c$  would lead to even higher efficiency values.

The reason for the high  $ZT$ -factor of TICs can be understood on the basis of formula (2.34) and by considering the following: the back current from the cold to the hot end in a thermionic energy converter can be kept smaller than in a thermoelectric device — the back emission from the collector and the diffusion current through the valence band, respectively. This results a higher Seebeck voltage in thermionic devices. Furthermore, the ratio of electric to thermal conductivity in thermoelectric devices is very high, equivalent to the ratio in metals, as it is dominated by the electronic contribution. This combination results in high  $ZT$  values for thermionic converters.

Summing up, the main advantage of thermionic converters over thermoelectric devices is the absence of a parasitic lattice heat transport, leading to higher possible efficiencies. Furthermore, thermionic energy converters can be operated at significantly higher temperatures, enabling higher Carnot efficiency limits.

## 2.7 Brief Historical Overview

Thermionic emission was discovered by Edison in 1884. It is described in the article ‘On a Peculiar Behaviour of Glow-Lamps When Raised to High Incandescence’ [53]. Edison found that an electric current is generated between two metal electrodes in vacuum when one of them is heated. Although electrons are responsible for the current, the phenomenon was soon called thermionic emission, as it was not well understood at that time. After some experimental work and analysis by Richardson [31, 54–56], Schlichter proposed to convert heat to electric energy by means of thermionic emission [7].

The role of the work functions was not understood in the beginning, which made an efficient energy conversion impossible. It was not until the 1950s, that the influence of the contact potential on thermionic energy converters was discovered [57]. The correct understanding of the physical processes and theoretical considerations on thermionic converters triggered a strong interest, both in research and industry, fueled by the promise of highly efficient heat engines generating electrical power [17, 23, 40–43, 58–76].

I specifically want to point out the contributions of George N. Hatsopoulos, who performed a considerable amount of pioneering work in the field over many years [6, 17, 29, 59, 62, 70, 77]. He also wrote two incredibly detailed and extensive textbooks of ‘thermionic energy conversion’, which are still the standard literature for today.

Thermionic energy converters were considered for a broad field of applications, including nuclear and combustion power plants, combustion motors, as well as solar and nuclear fueled converters for space travel and satellites [6, 75, 78]. However, as no highly efficient devices could be produced, the interest ceased and research was concentrated on space application, done almost exclusively in the USA and the Soviet Union [5, 79].

In the USA, the research on thermionic energy converters was not pursued strongly, as other priorities, especially the development of photovoltaics, emerged. In the Soviet Union, however, significant progress was made, leading to two successful test flights of satellites equipped with 5 kW nuclear-fueled thermionic energy converters within the ‘TOPAZ’ program (a Russian acronym for thermionic power from the active zone) in 1988 [5, 8]. Despite its success, the program was not continued, presumably due to the collapse of the Soviet Union. The TOPAZ project was resumed in the 1990s in a collaboration of American and Russian researchers. However, due to political decisions and low funding, the project was scaled down continuously and only little progress was achieved [5, 14, 79]<sup>5</sup>.

Another thermionic space project, the ‘HPALM’ program (High Power Advanced Low Mass), concentrating on solar converters, was launched by General Atomics Inc. in the 1990s and later joined by NASA. Several prototype devices were built and ground tested [81–83]. Unfortunately, despite intensive research, we were not able to find further publications after reference [81] from 2006, in which further testing was announced.

<sup>5</sup>TwoTICs built in the former Soviet Union were sold to the USA and were supposed to be launched in satellite test flights in the mid-1990s. However, after the protest of other research groups, the launch was delayed and ultimately cancelled. The researchers complained about the formation of a radiation belt, blocking the observations of astrophysical satellites. The effects of such belts could be observed during the earlier test flights within the TOPAZ program [80].

## *2 Introduction to Thermionic Energy Conversion*

In recent years, the interest in thermionic energy conversion has been renewed, mainly fueled by the general interest in alternative energy generation methods. But it was also due to the discovery of new materials specifically suited to thermionic energy converters [4,12, 13, 19–21, 84–89]. Terrestrial application for solar heat has not been seriously considered before [5, 6], but the possibility of enhancing the thermionic emission by exploiting the photoelectric effect enables highly efficient thermionic solar power conversion [9].

Moreover, progress in research using thermionic devices for refrigeration purposes was made in recent years [10, 21, 84, 90–94].

During all this time, no solution to avoid the detrimental effect of the space charge has been found. In the next chapters, I will show how the space charge problem can be solved, opening up the way to efficient thermionic energy conversion .

# 3 Concept of Thermoelectronic Energy Converters

Our new concept of thermionic energy converters uses electric and magnetic fields to suppress the space-charge. It enables a virtually space-charge free electron transport by converting previously static charges into a useful output current.

After introducing the model setup in detail, I will discuss the electron motion in crossed electric and magnetic fields to clarify the electron behavior in the system. Based on these considerations, I shall present several issues that should be considered when designing thermionic converters with applied electric and magnetic fields and illustrate the disadvantages of previously developed models. I will further show that the radiated power due to the acceleration of the electrons in the system is small and can be neglected.

At the end of the chapter, I will discuss how the strength of the space-charge potential and possible current densities in the system can be determined and show that the three-dimensional electron motion can be reduced to a one-dimensional model.

## 3.1 Working Principle and Introduction of the New Model

The basic concept of thermoelectronic energy converters is to use gate electrodes generating an electric field that accelerates the electrons away from the emitter to prevent the formation of a strong space-charge cloud. A magnetic guiding field can be applied to impede electrons from reaching the gate and guide them to the collector. Different models and geometric setups have been proposed, but none of them have proven successful [6,59,67,77,95], mainly due to flaws in the design, which have led to high loss currents and low output powers.

Our new model solves these problems. It is set up as follows: Emitter and collector are two plane-parallel metal plates. The gate electrode is a metal grid, mounted between the two plates. A positive voltage  $V_g$  is applied to the gate, generating a potential trough, which accelerates the electrons away from the emitter towards the gate. A homogenous magnetic guiding field  $B$ , oriented perpendicular to the surfaces of emitter and collector, forces the electrons on helical paths along the magnetic field lines, thus channeling them through the grid holes towards the collector. Figure 3.1 shows a sketch of the essential parts and displays the basic concept.

### 3 Concept of Thermoelectronic Energy Converters

This concept involves exclusively electrons, but no ions. Devices based on this model are therefore best characterized as ‘thermoelectronic energy converters’ (TEC), in contrast to the term ‘thermionic’ devices.

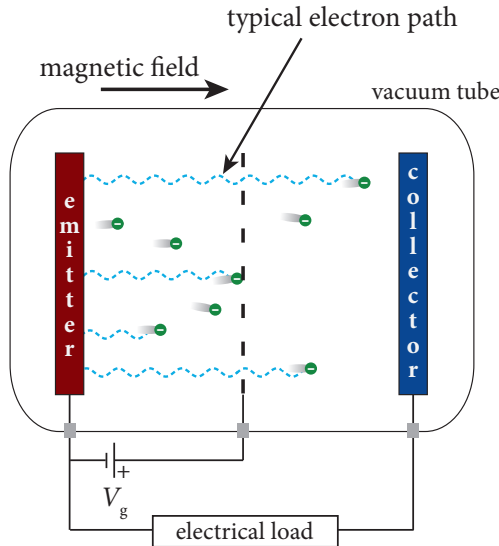


Figure 3.1: Schematic diagram of a thermoelectronic energy converter with a positively charged gate electrode between emitter and collector and a magnetic guiding field. The electrons are accelerated away from the emitter to avoid the formation of a strong space-charge cloud. The magnetic field prevents most of the electrons from reaching the gate by forcing them on helical paths along the field lines, thereby channeling them through the gate holes. In the figure, four electron paths are indicated by dashed blue lines. The radii of the electron paths are amplified for better visibility.

Electrons reaching the collector do not gain energy, neither from the electric nor the magnetic field. A static magnetic field does not change the kinetic energy of charged particles [96]. Although the electric field accelerates the electrons leaving the emitter, it decelerates the electrons as soon as they pass the gate. If emitter and collector are on the same electrostatic potential, the electrons have the same kinetic energy when reaching the collector as they had leaving the emitter.

Figure 3.2 shows the electrostatic potential  $\Psi(x)$  in the inter-electrode space for three different cases. If no gate voltage is applied,  $\Psi(x)$  is caused only by the space charge. When  $V_g$  is switched on, the space-charge potential is reduced by the potential of the gate electrode. For strong voltages, the space-charge is reduced enough that all electrons leaving the emitter reach the collector.

The figure further illustrates the space-charge density  $\rho_{sc}(x)$  for the three cases.  $\rho_{sc}(x)$  can be divided into contributions from electrons returning to the emitter and from electrons reaching the collector. The positively charged gate electrode converts previously static charges, preventing a strong current flow, into a useful output current.

#### Optimal Gate Structure

Electrons reaching the gate cause a current density  $J_g$ . To maintain the gate voltage, a power density of  $P_g = J_g V_g$ , has to be provided, leading to an additional energy loss in the TEC.

### 3.1 Working Principle and Introduction of the New Model

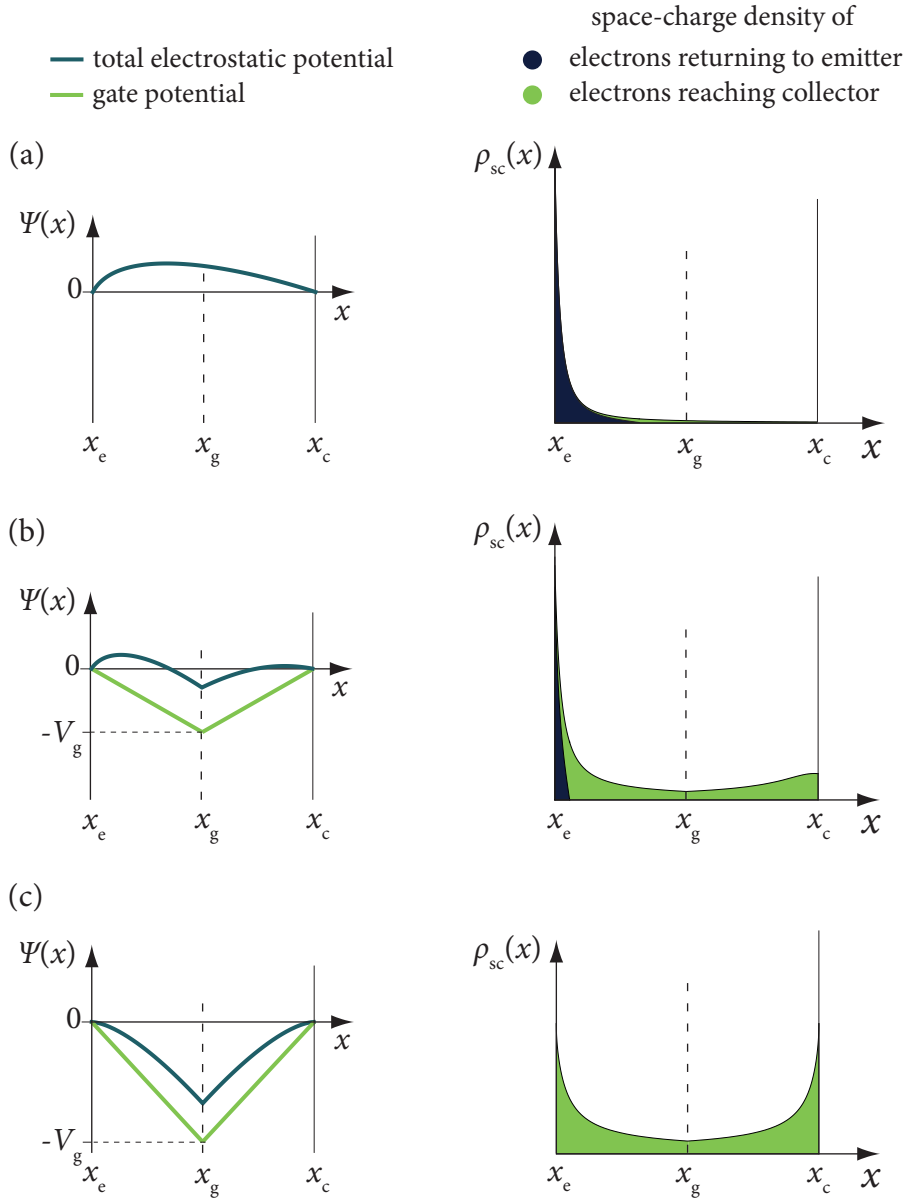


Figure 3.2: Sketch of the inter-electrode electrostatic potential  $\Psi(x)$  and the space-charge density  $\rho_{sc}(x)$  for three different gate voltages  $V_g$ . The space-charge density can be divided into contributions from electrons turned back to the emitter and electrons reaching the collector.  $x_e$ ,  $x_g$  and  $x_c$  indicate the positions of emitter, gate and collector, respectively. (a) For  $V_g = 0$ ,  $\Psi(x)$  is only caused by the space charge.  $\rho_{sc}(x)$  is dominated by electrons returning to the emitter. (b) For  $V_g > 0$ , the space-charge density at the emitter surface is reduced, as more electrons reach the collector. (c) For high values of  $V_g$ , typically in the range 2 V–20 V, depending on the setup, the space-charge potential is reduced enough so that all emitted electrons reach the collector. In this case,  $\Psi(x)$  does not form a maximum in the inter-electrode space. The potentials and space-charge densities were calculated at the example of the following parameters:  $\phi_e = 2.5$  eV,  $T_e = 1500$  K,  $d_{ec} = 100$   $\mu\text{m}$ ,  $V_g = 0$  V, 3 V and 6 V.

### 3 Concept of Thermoelectronic Energy Converters

To minimize this energy loss,  $J_g$  has to be kept small. The fraction of the electrons reaching the gate depends on the geometrical transparency  $t$  of the gate, which is defined as the ratio of the opening surface of the gate to the total surface, *i.e.*

$$t = \frac{A_{\text{openings}}}{A_{\text{total}}}. \quad (3.1)$$

If the radius of gyration of the electron paths is small compared to the grid bar diameter, the ratio of the electrons reaching the collector to the emitted electrons is approximately  $t$ .

If a surface is divided into regions of equal area, the partition has at least the perimeter of a regular, hexagonal grid [97]. A honeycomb pattern consisting of regular shaped hexagons (figure 3.3) therefore represents the optimal solution for our setup. To characterize the honeycomb gate, the mesh diameter  $w$  is used, corresponding to twice the length of one edge of a hexagon defining the structure.

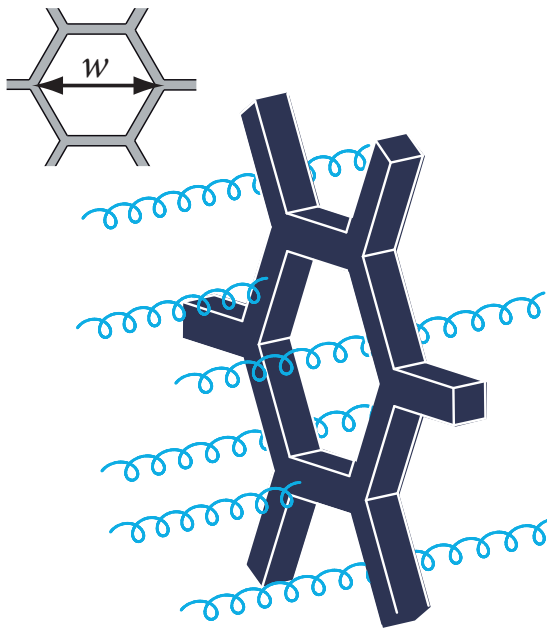


Figure 3.3: Sketch of a section of a honeycomb structured gate electrode with mesh diameter  $w$ . A honeycomb pattern represents the optimal structure for the gate electrode due to its high geometrical transparency  $t$ , equivalent to the ratio of the opening surface to the total surface. Typical electron paths are indicated. The fraction of the electrons hitting the gate depends on  $t$ . Drawing by Stefan Meir.

#### Electron Collisions and Mean Free Path in Thermoelectronic Energy Converters

In thermoelectronic converters, electron collisions should be avoided. In conventional thermionic converters, these processes can be ignored, as they lead to only small energy losses [6]. In thermoelectronic converters, however, some electrons that lose energy due to collisions may not be able to reach the collector. These electrons travel back and forth between emitter and collector, as they do not have enough kinetic energy to reach either electrode and eventually hit the gate. This process significantly increases the space charge and leads to a higher gate loss current.

To estimate the collision frequency, the mean free path of the electrons  $\lambda_e$  needs to be considered.  $\lambda_e$  depends on the pressure and the temperature in the vacuum — *i.e.*  $\lambda \propto \frac{T}{p}$

— as well as the type of the residual gases. Table 3.1 shows  $\lambda_e$  in vacuum for different pressures and temperatures, calculated using the formula given in reference [98].

	300 K	1000 K
1000 mbar	$6 \cdot 10^{-7}$ m	$2 \cdot 10^{-6}$ m
1 mbar	$6 \cdot 10^{-4}$ m	$2 \cdot 10^{-3}$ m
$10^{-3}$ mbar	0.6 m	2 m
$10^{-6}$ mbar	600 m	2000 m

Table 3.1: Mean free path of electrons  $\lambda_e$  calculated for different values of pressure and temperature [98]. The values shown are a good approximation for most residual gases including air.

The calculations show that a relatively high vacuum pressure of the order  $10^{-1}$  mbar is sufficient to avoid a strong influence of electron collisions. Assuming a gap width in the TEC of 100  $\mu$ m, only 1 % of the electrons are involved in collisions.

## 3.2 Electrons in Electric and Magnetic Fields

I will now recall the motion of electrons in electric and magnetic fields (E- and B-fields, respectively) on the basis of homogenous and static fields. The behavior of charged particles in E- and B- fields is well understood and the solutions presented below have been known for many years. However, these consideration provide an important insight into the electron behavior in our model system, even though the electric field is not homogenous. Furthermore, an upper limit for the radius of gyration can be calculated, which is crucial for our concept.

Electrons approach relativistic velocities if their kinetic energy is greater than 1 keV. The mean thermal energy of the electrons is of the order 100 meV. Through the gate field, electrons in a thermoelectronic converter can gain a maximum energy of  $eV_g$ . As gate voltages of the order of 10 V are applied, the electron velocities are only a fraction of the speed of light. I will therefore only consider non-relativistic electron motion.

In the following sections, I will derive the electron motions in combined electric and magnetic fields in several consecutive steps, before discussing the implications for the operation of thermoelectronic converters. As metric system, I am using the ‘International System of Units’ (SI).

Electrons with a velocity  $\boldsymbol{v}$  in an electric field  $\boldsymbol{E}$  and a magnetic field  $\boldsymbol{B}$  experience the Lorentz force<sup>1</sup>

$$\boldsymbol{F}_L = -e(\boldsymbol{E} + \boldsymbol{v} \times \boldsymbol{B}). \quad (3.2)$$

<sup>1</sup>The name ‘Lorentz force’ is not always used consistently. In some textbooks, the Lorentz force refers to the force due the magnetic field, whereas the force induced by the electric field is called the Coulomb force. Throughout this work I will use the term Lorentz force for the total force particles experience in electromagnetic fields.

### 3 Concept of Thermoelectronic Energy Converters

The equations of motion are given by [96]

$$\frac{d\mathbf{v}}{dt} = -\frac{e}{m_e} (\mathbf{E} + \mathbf{v} \times \mathbf{B}), \quad (3.3)$$

$$\frac{dE_{\text{kin}}}{dt} = -e\mathbf{v}\mathbf{E}. \quad (3.4)$$

#### Static and Homogenous Magnetic Fields

To begin with, I will consider a static, homogenous magnetic field without an electric field. The equations of motion (3.3) and (3.4) reduce to

$$\frac{d\mathbf{v}}{dt} = -\frac{e}{m_e} \mathbf{v} \times \mathbf{B}, \quad (3.5)$$

$$\frac{dE_{\text{kin}}}{dt} = 0. \quad (3.6)$$

Equation (3.6) indicates that the kinetic energy of the electrons remains constant at all times.

Choosing the z-axis in direction of the magnetic field, the solution of (3.5) is given by

$$x(t) = A \cos(\omega_B t + \phi) - \frac{v_{y0}}{\omega_B}, \quad (3.7)$$

$$y(t) = A \sin(\omega_B t + \phi) + \frac{v_{x0}}{\omega_B}, \quad (3.8)$$

$$z(t) = v_{z0} t, \quad (3.9)$$

where  $v_{x0}$ ,  $v_{y0}$  and  $v_{z0}$  represent the initial velocities in x,y,z-direction, respectively, whereas  $\phi = \arctan(-v_{x0}/v_{y0})$  represents the phase shift. The precession frequency  $\omega_B$ , also called the gyrofrequency, is given by

$$\omega_B = \frac{eB}{m_e}. \quad (3.10)$$

The radius of gyration, or gyradius,  $r_{\text{gyr}}$  is constant and depends on the initial velocity of the electrons and the magnetic field strength

$$r_{\text{gyr}} = A = \frac{\sqrt{v_{x0}^2 + v_{y0}^2}}{\omega}. \quad (3.11)$$

Equations (3.7), (3.8) and (3.9) describe a helical motion with the gyradius  $r_{\text{gyr}}$  along the magnetic field lines with a constant velocity  $v_{z0}$  parallel to the field. For electrons, the gyration is clockwise. Figure 3.4 shows a typical electron path in a static B-field.

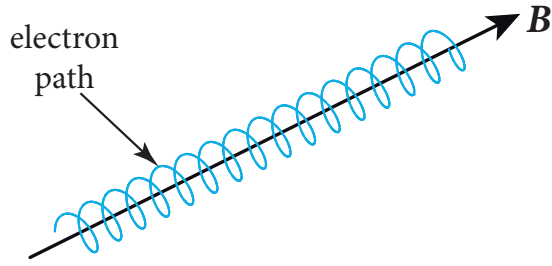


Figure 3.4: Sketch of a typical electron path in a homogenous, static magnetic field  $\mathbf{B}$ . Electrons perform a helical motion with a constant radius along the field lines.

### Combined Static and Homogenous Electric and Magnetic Fields

As a next step, I will analyze the electron motion in combined static and homogenous electric and magnetic fields. The following approach is partially based on considerations that are given in reference [96].

If both fields are parallel, the influences of the fields on the electron motion do not interact. The electric field accelerates the electrons in the direction that is unaffected by the magnetic field. The resulting trajectory is a helical path with a constant radius and varying pitch.

If the fields are not parallel, the effects cannot be considered separately. At first I will consider the specific case in which the electric and the magnetic fields are perpendicular. The generalization to fields with an arbitrary angle can be obtained by a slight modification of the results.

#### *Perpendicular Electric and Magnetic Fields*

The problem of perpendicular electric and magnetic fields can be divided into two cases, leading to qualitatively different electron behavior:  $|\mathbf{E}| < c|\mathbf{B}|$  and  $|\mathbf{E}| > c|\mathbf{B}|$ , where  $c$  represents the speed of light. As shown below, the second case should be avoided in TECs.

*Case (1):  $|\mathbf{E}| < c|\mathbf{B}|$*

In this case, the magnetic field dominates the electron motion. A Lorentz transformation can be performed into a coordinate system  $C'$ , which moves with a velocity  $\mathbf{u}_B$  relative to the original coordinate system  $C$ .  $\mathbf{u}_B$  is perpendicular to both  $\mathbf{E}$  and  $\mathbf{B}$  and is given by

$$\mathbf{u}_B = \frac{\mathbf{E} \times \mathbf{B}}{B^2}, \quad \text{with} \quad |\mathbf{u}_B| = \frac{E}{B}. \quad (3.12)$$

In  $C'$ , the only effective field is a magnetic field  $\mathbf{B}'_{\perp}$  perpendicular to  $\mathbf{u}_B$ .  $\mathbf{B}'_{\perp}$  is weaker than the original field, but points in the same direction as  $\mathbf{B}$

$$\mathbf{B}'_{\perp} = \left( \frac{B^2 - c^2 E^2}{B^2} \right)^{\frac{1}{2}} \mathbf{B}. \quad (3.13)$$

### 3 Concept of Thermoelectronic Energy Converters

This means that electrons in  $C'$  follow the magnetic field lines in helical paths, analog to the case when no electric field is present. From the view of the original coordinate system, the gyration is combined with a drift perpendicular to the electric and the magnetic field.

The same result can be obtained by directly solving equation (3.3). The z-direction is chosen to be parallel to the direction of the magnetic field and the x-direction parallel to the electric field. This leads to

$$x(t) = A \cos(\omega_B t + \phi) - \frac{m_e B}{e E^2} - \frac{v_{y0}}{\omega_B}, \quad (3.14)$$

$$y(t) = A \sin(\omega_B t + \phi) - \frac{E}{B} t + \frac{v_{x0}}{\omega_B}, \quad (3.15)$$

$$z(t) = v_{z0} t, \quad (3.16)$$

with the phase shift

$$\phi = \arctan\left(-\frac{v_{x0}}{v_{y0} + E/B}\right), \quad (3.17)$$

and

$$A = \frac{(v_{x0}^2 + (v_{y0} + E/B)^2)^{\frac{1}{2}}}{\omega_B}. \quad (3.18)$$

These equations describe a precession about the magnetic field lines with the radius of gyration  $r_{\text{gyr}} = A$ , accompanied by a shift in y-direction — perpendicular to the E- and B-field — with the velocity  $u = E/B$ . The frequency of gyration  $\omega_B$  does not depend on the electric field. The velocity in z-direction also remains unaffected.

The motion can be understood by considering the following: electrons are forced on helical paths by the magnetic field. The electric field accelerates the particles when they fly in the direction of the E-field and decelerates them when they fly in the opposite direction. Consequently,  $r_{\text{gyr}}$  is larger for one half of the turn than for the other half. This leads to a shift of the center of gyration.

Summing up, the only effect resulting from a perpendicular electrostatic field in addition to the magnetostatic field is a drift velocity perpendicular to both fields, but no drift in direction of the electric field. This result is valid if the magnetic field dominates the electron motion, *i.e.*  $|E| < c|B|$ . It has important implications for thermoelectronic converters, as I will demonstrate below.

*Case (2):  $|E| > c|B|$*

In this case, the electric field dominates the electron motion. A Lorentz transformation can be performed into the coordinate system  $C''$ , moving with the velocity

$$\mathbf{u}_E = c^2 \frac{\mathbf{E} \times \mathbf{B}}{E^2}, \quad \text{with} \quad |\mathbf{u}_E| = c^2 \frac{B}{E}. \quad (3.19)$$

Again,  $\mathbf{u}_E$  is perpendicular to both E- and B-field. In this case, however, the only effective field in  $C''$  is an electric field  $E''_{\perp}$  perpendicular to  $\mathbf{u}_E$

$$E''_{\perp} = \left( \frac{E^2 - \frac{1}{c^2} B^2}{E^2} \right)^{\frac{1}{2}} E. \quad (3.20)$$

Electrons in  $C''$  are accelerated in the direction of  $E''_{\perp}$ . In the original coordinate system  $C$ , the motion is accompanied by the drift velocity  $\mathbf{u}_E$ . The resulting motion is a hyperbolic trajectory.

The consequence of a dominant electric field in thermoelectronic converters would be that electrons are accelerated towards the gate electrode, away from the collector, ruining the converter's performance. This case should therefore be avoided.

### *Non-Perpendicular Electric and Magnetic Fields*

If the electric and magnetic fields have parallel components, the solution of the equation of motion is more difficult to solve. No Lorentz transformation into a coordinate system, in which one of the fields is effectively zero, exists, since the vector product  $\mathbf{E} \cdot \mathbf{B}$  is Lorentz-invariant. However, the equation of motion can be solved by a slight modification to the previous solutions.

The electric field can be divided into a component  $E_{\parallel}$  parallel to and a component  $E_{\perp}$  perpendicular to  $\mathbf{B}$ . Here, I will only consider the case  $|E_{\perp}| < c|B|$ , which corresponds to case (1) of the previous section.

The effect of  $E_{\perp}$  can be determined in analogy to the case of perpendicular fields. The electrons perform a helical motion along the magnetic field lines with an additional drift perpendicular to both  $\mathbf{B}$  and  $E_{\perp}$ , with the drift velocity

$$\mathbf{u}_B = \frac{\mathbf{E}_{\perp} \times \mathbf{B}}{B^2}, \quad \text{with} \quad |\mathbf{u}_B| = \frac{E_{\perp}}{B}. \quad (3.21)$$

The radius of gyration is given by

$$r_{\text{gyr}} = \frac{\left( v_{x0}^2 + (v_{y0} + E_{\perp}/B)^2 \right)^{\frac{1}{2}}}{\omega_B}. \quad (3.22)$$

$E_{\parallel}$  accelerates the electrons parallel to the magnetic field lines. The electron motion in this direction is unaffected by the magnetic field. This results in a modification of the pitch of the helical path. Figure 3.5 illustrates a typical electron path for combined, non-perpendicular fields.

### **Implications for Thermoelectronic Energy Converters**

In a thermoelectronic energy converter, the electric field  $E$  generated by the gate electrode is not homogeneous. Nonetheless, the preceding discussion can be used to qualitatively describe the electron motion in the system.

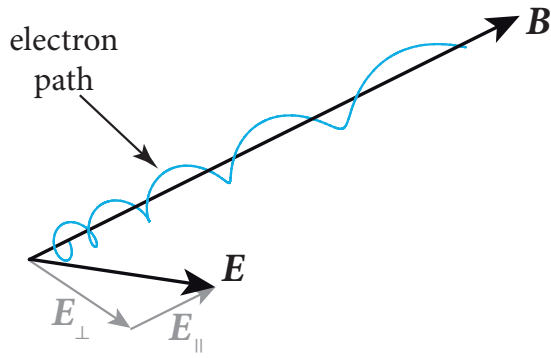


Figure 3.5: Sketch of a typical electron path in combined, non-perpendicular electric and magnetic fields. The electron follows the magnetic field line along a helical path. The pitch of the path increases, as the parallel component  $E_{\parallel}$  of the electric field accelerates the electron in direction of the magnetic field. The drift velocity, caused by the perpendicular component  $E_{\perp}$ , is not shown.

Figure 3.6 shows a sketch of the field lines for a cross-section of the converter. At any point,  $E$  can be divided into two components:  $E_{\parallel}$ , which is parallel to the magnetic field, and  $E_{\perp}$ , which is perpendicular to the magnetic field. The components  $E_{\parallel}$  and  $E_{\perp}$  are not constant, but vary with the position. Near the emitter and collector surfaces, the electric field is mainly parallel to  $B$ , whereas the perpendicular term  $E_{\perp}$  is small. The closer the electrons are to the gate, the stronger is  $E_{\perp}$ .

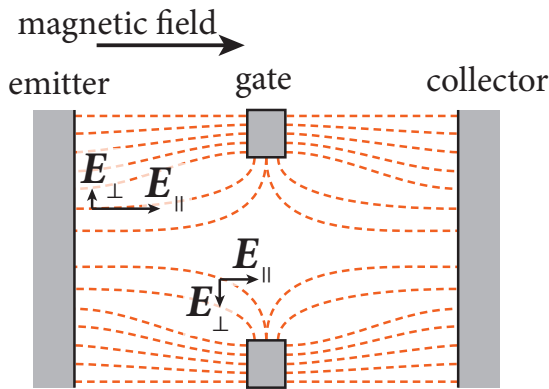


Figure 3.6: Sketch of the electric field lines inside a TEC with a gate electrode for a cross-section of the setup. At any point, the electric field can be divided in a parallel component  $E_{\parallel}$  and a perpendicular component  $E_{\perp}$ . The strength of the components varies with the position.

If  $B > E_{\perp}$ , the electrons follow the magnetic field lines on helical paths and are mainly guided through the openings. As I have shown above, electrons do not move in the direction of  $E_{\perp}$ , but perform a drift with velocity  $u_B$  perpendicular to  $E_{\perp}$ .

This effect is important for thermoelectronic converters. The electric field component  $E_{\perp}$  always points towards the nearest grid bar. As a result, the electrons perform a drift in the direction perpendicular to  $E_{\perp}$  (figure 3.7), but not towards the gate. If the electrons move closer to another grid bar, the direction of  $E_{\perp}$  changes and therefore also the direction of the drift velocity. This effect always ‘guides’ electrons away from the gate. The resulting drift motion follows a circular-like path. As a consequence, only few electrons reach the gate. The radius of gyration and the drift velocity vary with the strength of  $E_{\perp}$ .

The radius of gyration  $r_{\text{gyr}}$  can be computed using formula (3.22). To estimate an upper limit for  $r_{\text{gyr}}$  the maximum value for  $E_{\perp}$  can be used. If  $r_{\text{gyr}}$  is small, only electrons emitted on the emitter area exactly facing the grid bars reach the gate.

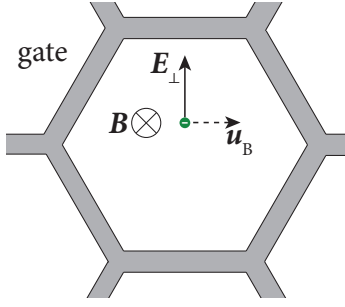


Figure 3.7: Sketch showing the effect of the perpendicular component  $E_{\perp}$ , which is pointing towards the grid bars. Due to the magnetic field, electrons perform a drift with velocity  $u_B$  in the direction perpendicular to  $E_{\perp}$ , but not in the direction of  $E_{\perp}$ . Consequently, these electrons do not reach the gate.

The parallel component of the electric field  $E_{\parallel}$  controls the electron velocity in longitudinal direction. It is responsible for accelerating the electrons away from the emitter and reducing the space-charge potential. As the velocity of the electrons varies, so does the pitch of the path.

The charge of the electrons alters the electric field distribution. However, in an efficient TEC, the electric field generated by the gate has to be strong enough to reduce the space charge so that electrons are mainly controlled by the gate electric field. In this case, the space charge only yields a small contribution.

These considerations show that the applied magnetic field must fulfill the condition  $cB > E_{\perp}$  to force the electrons on helical paths along the magnetic field lines. The radius of gyration can be determined by using formula (3.22). An important effect of the combined fields is that electrons perform a drift in the direction perpendicular to both fields, but not towards the gate bars. The electric field component  $E_{\parallel}$  parallel to the magnetic field is responsible for accelerating the electrons away from the emitter and must be considered when determining the required electric field strength to suppress the space-charge potential.

### Energy Loss Due to Radiation of Accelerated Electrons

The power radiated by an accelerated electron is given by the Lamor formula [96]

$$P = \frac{e^2}{6\pi\epsilon_0 c^3} |\dot{\mathbf{v}}|, \quad (3.23)$$

where  $\mathbf{v}$  is the velocity of the electron and  $\epsilon_0$  the vacuum permittivity.

An upper limit for the radiated power can be estimated by approximating the gate electrode by a metal plate, which is transparent for electrons. In this case, the generated electric field  $E = V_g/x_g$  is homogeneous and constant between emitter and collector with the gate voltage  $V_g$  and the emitter-gate distance  $x_g = d_{ec}/2$ . The acceleration of the electrons due to the electric field is then given by

$$a_E = \frac{eE}{m_e}. \quad (3.24)$$

### 3 Concept of Thermoelectronic Energy Converters

The time an electron needs to travel through the vacuum gap is

$$t_{ec} = 2\sqrt{\frac{2x_g m_e}{eE}}. \quad (3.25)$$

During that time, according to equation (3.23), the electron radiates the energy

$$E_{e,rad} = Pt_{ec} = \frac{e^4 E^2}{3\pi\epsilon_0 c^3 m_e^2} \sqrt{\frac{2x_g m_e}{eE}}. \quad (3.26)$$

The power radiated by a current  $I$  of electrons is consequently obtained through

$$E_{e,rad} \frac{I}{e} = \frac{e^4 E^2}{3\pi\epsilon_0 c^3 m_e^2} \sqrt{\frac{2x_g m_e}{eE}} \frac{I}{e}. \quad (3.27)$$

The acceleration due to the magnetic field  $B$  is given by

$$a_B = \frac{e}{m_e} v_{\perp} B = \frac{e}{m_e} \sqrt{\frac{2E_{kin,\perp}}{m_e}} B, \quad (3.28)$$

where  $v_{\perp}$  represents the velocity of the electrons perpendicular to the magnetic field lines.

Analogous to the electric field, the total radiation of an electron current can be calculated, yielding

$$\frac{2e^4 B^2 E_{kin,\perp}}{3\pi\epsilon_0 c^3 m_e^3} \sqrt{\frac{2x_g m_e}{eE}} \frac{I}{e}. \quad (3.29)$$

Neglecting the mean thermal energy of order 100 meV, the maximum kinetic energy of the electrons is given by  $eV_g$ . Assigning this energy to all electrons as the kinetic energy perpendicular to the magnetic field constitutes an upper limit for the radiated energy due to the magnetic-field acceleration.

Assuming a gate voltage of 10 V, an emitter-collector distance of 100  $\mu\text{m}$ , a magnetic field of 1 T and a current of 10 A, the total power emitted by all electrons due to the acceleration of both magnetic and electric fields is of order  $10^{-11}$  W. The radiated power therefore plays no role in a thermoelectronic converters and can be neglected.

## 3.3 Guidelines for Efficient Energy Converters with Gate Electrodes

The following issues sum up the conclusions of diverse questions and discussion that arose during the course of our project. Although not all of them can be analytically proven and there can be exceptions in certain cases, they provide a guideline for designing new

models of TECs using electric fields to suppress the space-charge potential. Considering these issues will further help to clarify why previous models have failed.

- It is generally advantageous to apply a magnetic guiding field in combination with the electric field. Not only does the magnetic field prevent electrons from reaching the gate, it can also be used to guide them to the collector.
- The time it takes the electrons to travel from the emitter to the collector should be kept as short as possible to avoid the formation of a strong space-charge potential. This condition is equivalent to short electron paths. With increasing electron path-lengths, the gate voltage required to suppress the space charge increases, increasing the power loss on the gate.
- Creating crossover points of the electron paths should be avoided. These points constitute regions of concentrated negative charges, which repel electrons and may force them away from the desired paths. Furthermore, if high space charge regions are generated, a high voltage has to be applied to suppress the space charge. A good example for a TEC model with cross over points is the ‘magnetic triode’ [6,59,76,77] that will be discussed below.
- The required magnetic field strength on the emitter surface should be constant and all electrons should, in principle, follow the same magnetic field distribution, irrespective of where they are emitted from. It is impractical to use inhomogeneous magnetic fields in real devices. Furthermore, if certain parameters of the setup are modified, such as the emitter temperature or the gate voltage, the magnetic field has to be adjusted. The electron paths are thus unstable against changes in the setup.
- There are two ways of using a magnetic field to guide the electrons: either the electrons directly follow the magnetic field lines on helical paths with a relatively small radius of gyration (as in the model presented in this work) or the magnetic field forces the electrons to perform rather large circles leading them from the emitter to the collector without performing one full circle (as, *e.g.*, in the ‘magnetic triode’ discussed below). The second scenario has several disadvantages.

In the second case, the magnetic field will be weaker than in the first case, as the radii of gyration need to be larger. Therefore, only smaller electric fields can be applied before electrons are accelerated towards the gate (compare chapter 3.2).

Furthermore, the electron-circle radius has to be perfectly adjusted to the setup parameters for the electrons to reach the collector. If the magnetic field is too weak, electrons do not reach the collector. If the magnetic field is too strong, electrons perform more than one circle in the vacuum gap, leading to electron-path cross sections that should be avoided. Moreover, changing the setup parameters, such as the emitter temperature or the gate voltage, would require an adjustment of the magnetic field, which is impractical for real devices, especially if permanent magnets are used.

### Review of the Previous, Unsuccessful Models

The issues presented above can also be used to illustrate the disadvantages of previous models of thermionic converters using gate electrodes. Hatsopoulos was the first to propose the concept of using electric and magnetic fields in TICs in the 1950s [6]. He presented two models, which he called the ‘electrostatic triode’ and the ‘magnetic triode’ [6, 59,76,77]. The ‘electrostatic triode’ was quickly abandoned, whereas the ‘magnetic triode’ was considered as a promising approach and was subject of several years of research.

The ‘electrostatic triode’ uses a plane-parallel setup with a positively charged grid between emitter and collector. The model bears some similarity to our model. However, as a big difference, no magnetic guiding field was applied. Experimental tests revealed a very high gate current. This model therefore did not work [6].

Figure 3.8 shows a schematic diagram of the ‘magnetic triode’. Emitter and collector are two parallel metal plates positioned side by side, while the gate electrode is metal plate placed face to face with them. A magnetic field is applied perpendicular to the emitter and collector surfaces, forcing electrons on circular-like paths. Experimental test devices have been built and theoretical calculations of the electrostatic potential, the electron paths and the possible current densities have been performed. In test models voltages of order 100 V were applied, and a gate current of about 10 % of the total current was measured [6, 73]. However, due to the high power consumed by the gate electrode and the load current being small, the ‘magnetic triode’ was ultimately also abandoned.

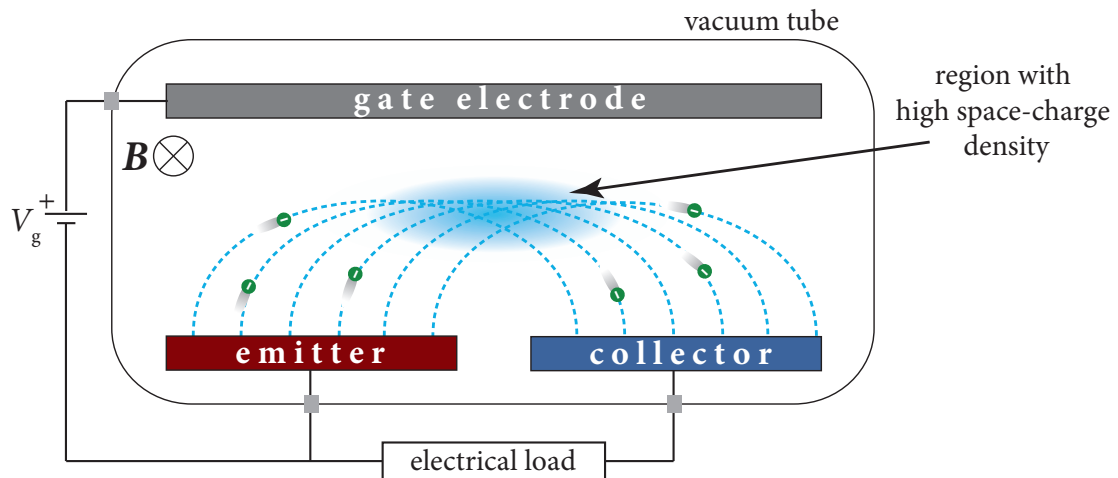


Figure 3.8: Sketch of the ‘magnetic triode’ and typical electron trajectories in the system. The model was proposed by Hatsopoulos in the 1950s [59]. The applied magnetic field leads to cross sections of the electron paths, creating a region with a high space-charge density.

The drawbacks of the ‘magnetic triode’ can be understood by considering the issues discussed in the previous section. The setup leads to cross sections in the electron paths, creating a region with a high space-charge density (figure 3.8). Furthermore, in practical devices, emitter and collector need to have surfaces at least of the order of millimeters. The

electrons paths are of the same order of magnitude, leading to a very strong space-charge potential. As I will show in chapter 4, the distances covered by the electrons even with an accelerating electric field should be below about  $100\ \mu\text{m}$  for no dominant space-charge potential to be formed.

Further disadvantages are the use of a relatively weak magnetic field, which allows only weak electric fields before the electrons are accelerated towards the gate electrode (compare section 3.2), and the instability of the circular-like paths.

Figure 3.9 shows a modification of ‘magnetic triode’, which avoids the formation of a concentrated space-charge region. However, other disadvantages, such as the long electron paths, the weak magnetic field (allowing only weak electric fields) and the instability of the electron paths, remain. Furthermore, the B-field has to be stronger for electrons emitted closer to the collector than for electrons emitted further from the collector. Such a magnetic field is impractical for real devices.

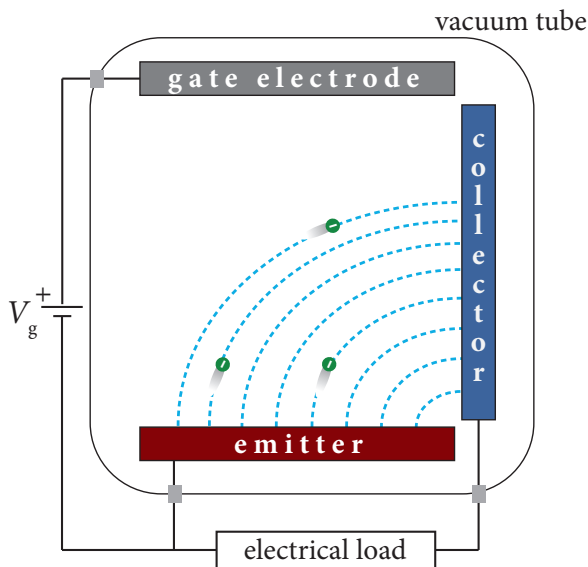


Figure 3.9: Sketch of a variant of the thermionic triode, avoiding a concentrated space-charge region. However, this model has several disadvantages, such as the requirement of an inhomogeneous magnetic field.

Other setups using electric and magnetic fields have been proposed, for example by Laing [95]. All his models, however, have clear drawbacks, which will be illuminated by considering the issues discussed above.

## 3.4 Model Calculations for Thermoelectronic Energy Converters

The first step for modeling TECs is to gain an elementary understanding of the electron behavior in the system, as has been done in chapter 3.2. The next step is to estimate the space-charge potential in the inter-electrode space and the possible current densities.

An exact analytical approach, determining the space-charge potential by solving the three-dimensional Poisson equation, is virtually impossible.

Our first approach was to use a particle traction software with integrated electric and magnetic field solvers for the model calculations. Below I will give a brief introduction to the software package and present simulations illustrating the electron behavior in the system. Although the space charge of the emitted particles can be included in the calculations, this approach proved to be not conducive to calculate the current density, because the computational effort is too high and in many cases the solutions do not converge.

However, by investigating the electric field distribution, it became evident that the electron motion can be mapped onto a one-dimensional system. As I will demonstrate in the following chapter, this enables us to estimate the space-charge potential and the current densities by using a one-dimensional electrostatic approach.

### Field Calculations and Particle Tracing with a Three-Dimensional Simulation Software

After testing several software packages, we decided to use the three-dimensional particle trajectory simulation software 'Lorentz', developed by 'Integrated Engineering Software' (IES) [99]. It includes the three-dimensional magnetic field solver 'Amperes' and electric field solver 'Coulomb'. The software offers a CAD-import, enabling the user to draw complex geometrical setups for the simulations in specific CAD-programs.

IES provides both the 'finite element method' (FEM) and the 'boundary element method' (BEM) for the calculation of electric and magnetic fields. In FEM, the volume is divided into discrete finite elements. The electro-magnetic partial differential equations are solved for every element in relation to the other elements. In BEM, not the volume, but the surface of the geometrical objects is discretized. The partial differential equations are solved in the integral form, by trying to fit the given boundary conditions to the boundary elements. For electric fields for example, surface charges are assigned to each surface element. When a solution is found, the exact fields can be calculated at any given points in the volume directly from the BEM solution.

The boundary element method holds advantages over the finite element method for certain applications. For example, BEM is more efficient for geometries with high surface to volume ratio. Another example is the calculation of electric and magnetic fields in vacuum. For a detailed discussion about the concept, advantages and applications of the boundary element method, please refer to, *e.g.*, reference [100]. All calculations presented in this work exclusively use BEM.

IES offers various options for the field solvers, the particle tracing solvers and overall physical boundary conditions which can be chosen for each model to obtain the most efficient computational process and high precision results. I will not discuss these options here. More detailed information is given in [99].

To calculate the electric field distribution in our model system, I drew only a section of the setup, making use of the symmetry options provided by IES. It is possible to define symmetric and periodic boundary conditions in the geometrical setup, significantly reducing the computational effort.

Our model can be reduced to 1/6 of the total system due to its angular periodicity. Figure 3.10 shows a screenshot of the section drawn and its symmetry planes<sup>2</sup>. As a basis for the model, I used our experimental setup described in chapter 5.

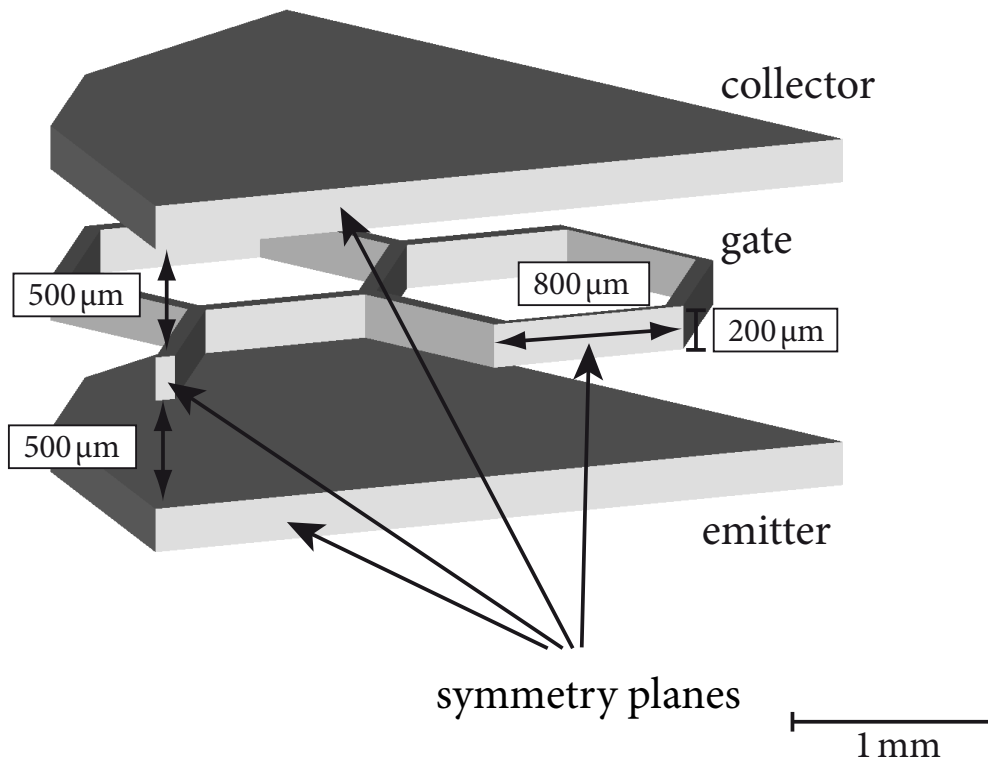


Figure 3.10: Screenshot of a drawn section of the system, consisting of the emitter, collector and the gate, which is used for model calculations in IES. By exploiting the angular symmetry of the system, only 1/6 of the model has to be defined. The symmetry planes on the front side are indicated in the image.

<sup>2</sup>Unfortunately, the image export function in IES is very limited, as it does not enable high-quality, high-resolution images.

### 3 Concept of Thermoelectronic Energy Converters

After defining the materials<sup>3</sup> and assigning a voltage to all three components, the electric field can be calculated. The field solver assigns two-dimensional boundary elements to all surfaces, their density depending on the preset precision. Figure 3.11 shows an example of the assigned boundary elements.

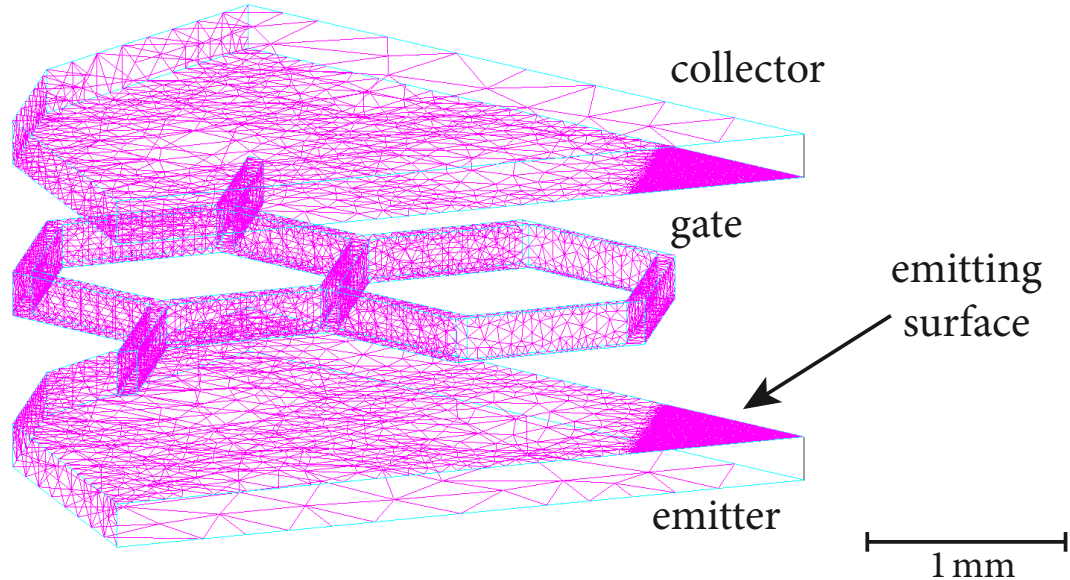


Figure 3.11: Illustration of boundary elements assigned to each surface. The density of the elements depends on the predefined precision. The surface that will be used to emit particles is indicated. The precision has been set very high for this surface.

Figure 3.12 shows the calculated electric field at the emitter surface for a gate voltage of 10 V. The electric field reflects the structure of the gate electrode; in the meshes it is weaker than at the grid bars. To calculate the electric field distribution, a voltage has to be assigned to all three components. In the following figures, I will indicate the voltages assigned to emitter, gate and collector using  $V_e$ ,  $V_g$  and  $V_c$ , respectively.

As a next step, electrons are emitted from a designated surface. The electric field solution is used to determine the electron trajectories. Figure 3.13 shows the calculated paths of four electrons emitted at different positions on the emitter surface, with an applied longitudinal magnetic field of 1 T. The radius of gyration is not visible here, as it is too small.

Figure 3.14 shows the electrons trajectories from different perspectives to illustrate the helical motion and the drift velocity, as discussed in chapter 3.2.

<sup>3</sup>IES offers several materials that can be assigned to all components. Additional materials with specific characteristics can be defined. However, for the calculations performed here, the exact materials are not essential, provided that a metal with a sufficiently high conductivity is chosen. I chose copper as the standard material for all calculations.

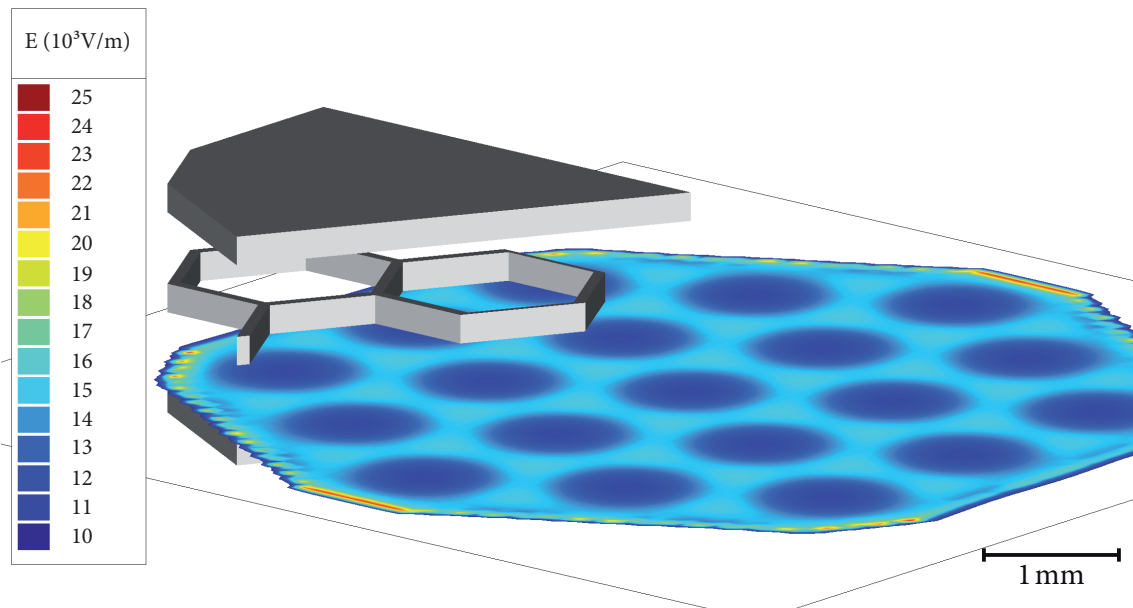


Figure 3.12: Calculated electric field at the emitter surface for an applied gate voltage of 10 V. The field has been determined not only for the section drawn, but for the total model. Parameters used:  $V_e = 0 \text{ V}$ ,  $V_g = 10 \text{ V}$ ,  $V_c = 0 \text{ V}$ .

### 3 Concept of Thermoelectronic Energy Converters

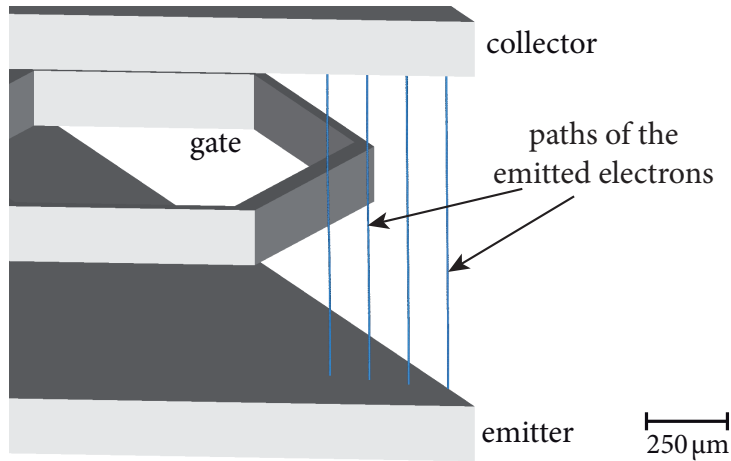


Figure 3.13: Screenshot of the calculated trajectories of four electrons emitted from different positions on the emitter surface. A longitudinal magnetic field of 1 T is applied. The helical motion of the electrons along the magnetic field lines cannot be seen here, as the radius of gyration is too small. The electrons started with an initial kinetic energy of 0.1 eV. Parameters used:  $V_e = 0$  V,  $V_g = 10$  V,  $V_c = 0$  V.

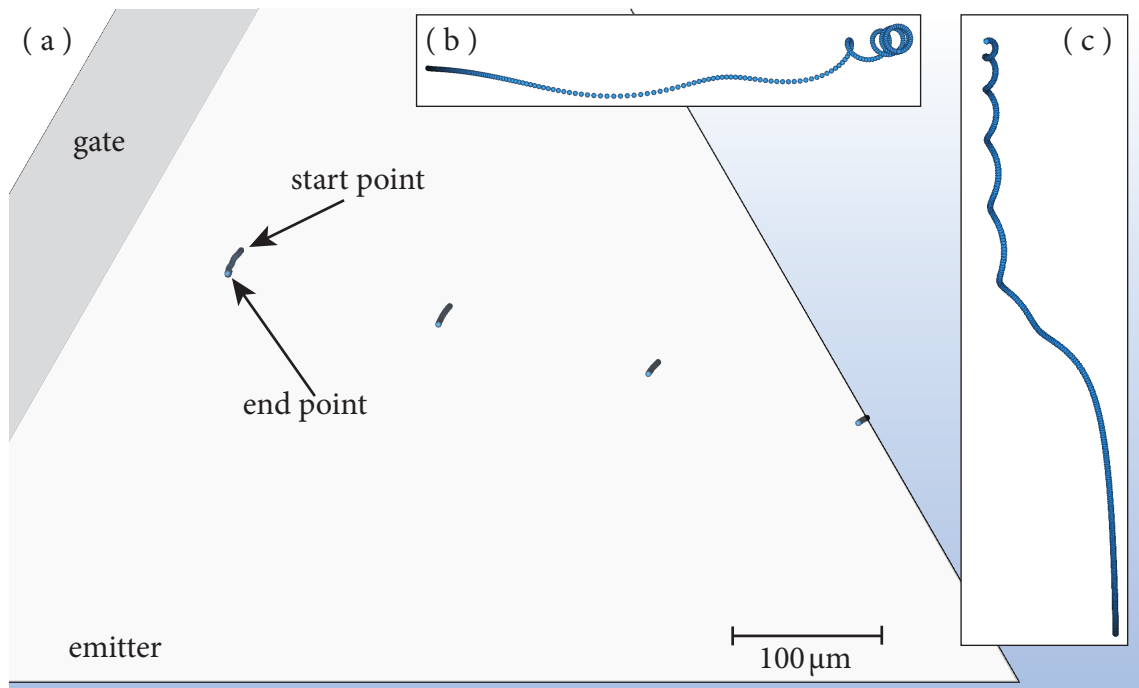


Figure 3.14: Screenshot of the same electron paths as in figure 3.13, shown from different perspectives. (a) Top view: the drift velocity of the electrons perpendicular to the electric and magnetic fields can clearly be observed, consistent with the considerations in section 3.2. The velocity is greater for electrons closer to the gate, as the electric field is stronger. (b) Side view: the helical motion of the electrons is visible from this perspective. (c) Side view: the drift velocity is strong in the middle of the path, corresponding to the region where the electrons pass the gate and the electric field is strong. Parameters used:  $V_e = 0$  V,  $V_g = 10$  V,  $V_c = 0$  V.

Figures 3.15 and 3.16 show the trajectories for 30 emitted electrons without and with an applied magnetic field of 1 T, respectively, demonstrating the channeling effect of the magnetic field, which forces the electrons on quasi-one-dimensional paths.

The results of these simulations, describing the electron behavior in the system, are consistent with my previous considerations, which were based on homogeneous and static fields. This shows that the simplified scenario of homogeneous fields provides a reliable basis for predicting the electron behavior in the model system.

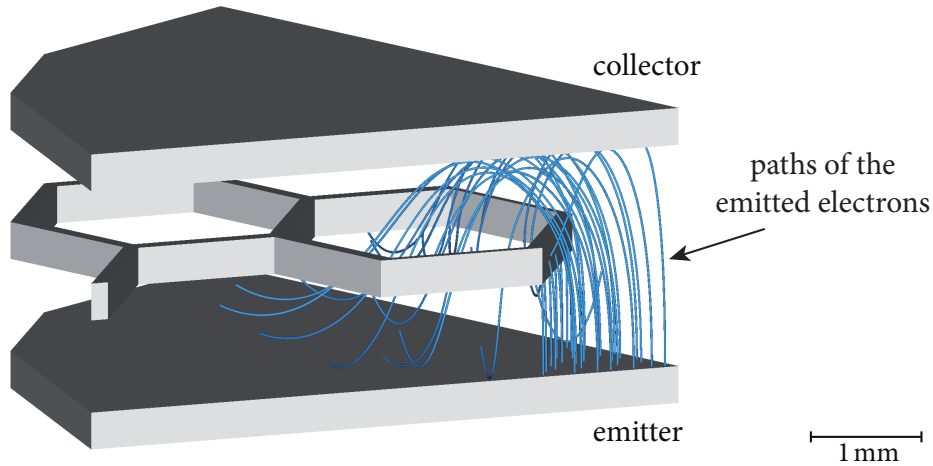


Figure 3.15: Illustration of the trajectories of 30 electrons emitted with no magnetic field applied. Parameters used:  $V_e = 0\text{ V}$ ,  $V_g = 10\text{ V}$ ,  $V_c = 0\text{ V}$ .

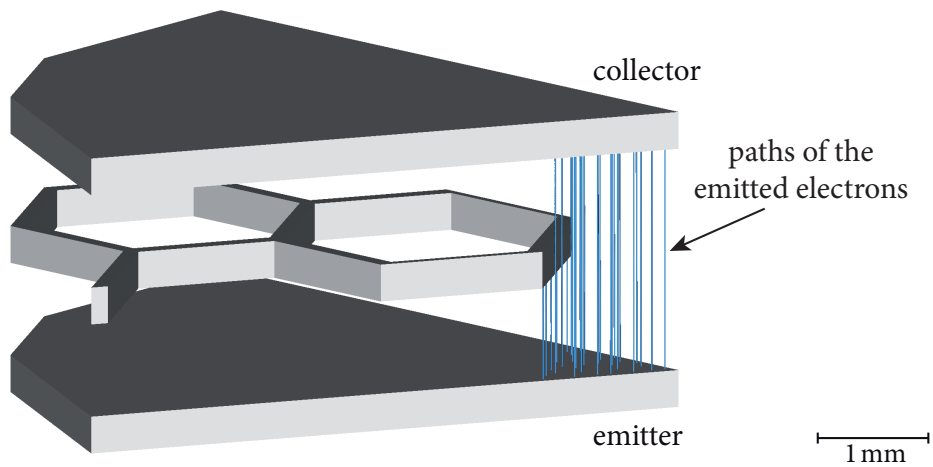


Figure 3.16: Illustration of the trajectories of 30 electrons emitted with an applied longitudinal magnetic field of 1 T. The magnetic field does not only prevent electrons from hitting the gate but also channels them onto the collector by forcing them on quasi-one-dimensional paths. Parameters used:  $V_e = 0\text{ V}$ ,  $V_g = 10\text{ V}$ ,  $V_c = 0\text{ V}$ .

### **Limitations of the Three-Dimensional Field Approach**

To determine the current density in the system, the space charge needs to be included in the calculations. ‘Lorentz’ offers the possibility to calculate the space-charge density of the emitted particles by assigning a charge to each electron path depending on the velocity of the particles and the predefined current.

The current density in a given system can, in principle, be determined in an iterative process. By combining the space-charge density with the external potential, the total electric potential is calculated. The electrons are then reemitted and the fields are recalculated, until the solutions converge within a defined error limit.

Introducing the space charge into the simulations showed that for high current densities, many electrons are not able to reach the collector. Depending on the strength of the magnetic field, the electrons are either forced back to the emitter or escape in various directions.

However, these calculations proved problematic for the following reasons:

- For high defined currents, the calculations converge only very slowly or not at all. The emitted electrons describe complex trajectories — helical paths with varying radii and pitches. Even a small fluctuation in the electric field changes the paths and prevents the solutions from converging. Furthermore, if electrons start to escape in different directions, the calculations do not converge at all, as the paths change significantly for every iteration.
- The electrons are accelerated to high velocities (near the gate) before they are decelerated down to their initial velocity. A small error when the electrons are fast leads to a big error when they are slow again. For this reason, the precision has to be set very high, significantly increasing the computational effort.
- For a sufficient precision of the results, a high number of electrons has to be emitted. When including a thermal distribution of the initial electron velocities, this number is furthermore multiplied by a factor of at least 10–20, resulting in a very high number of electron trajectories to be calculated.

These effects lead to a very high computational effort and render the simulations extremely time consuming. One simulation with a predefined current density already takes several hours. Many such runs are required to determine the actual current density for one specific set of parameters. To investigate a converter setup with a given geometry for different temperatures and applied voltages, these simulations would have to be repeated for many different values.

For these reasons, I had to find a different approach to determine the space-charge potential and current density in thermoelectronic energy converters.

### Transition to One-Dimensional Model Calculations

The space-charge cloud is mainly formed close to the emitter surface. I therefore performed various calculations to determine the electric field generated by the gate near the emitter surface for different geometry setups.

As already illustrated earlier, the electric field at the emitter surface reflects the structure of the gate electrode. If the distance between emitter and gate  $d_{eg}$  is increased, however, the pattern of the electric field vanishes until it becomes almost completely uniform and resembles the field created by a metal plate.

I illustrated this effect in figure 3.17 and 3.18. Figure 3.17 shows the calculated electric field at the emitter surface, while figure 3.18 shows the electric field along a line on the emitter surface, both for different emitter-gate distances.

The distance, at which the electric field at the emitter surface becomes homogeneous, depends on the gate geometry, foremost the mesh diameter  $w$ . As a rule of thumb, the distance is given by  $d_{eg} \approx 1/2w$ , which corresponds to an emitter-collector distance of  $d_{ec} \approx w$  for a symmetrical setup.

I further investigated the electric field between emitter and gate for the case  $d_{ec} \gtrsim w$ . The field is not only uniform at the emitter surface, but almost in the entire inter-electrode space, except for very close to the gate. Figure 3.19 shows the electric-field component in  $z$ -direction at three different positions between emitter and gate. The electric field in  $z$ -direction represents the component parallel to the magnetic field  $E_{\parallel}$  and is responsible for accelerating the electrons away from the emitter surface (compare to section 3.2). At the emitter surface, the total electric field and the  $z$ -component are equivalent, as the electric field must be perpendicular to the metal surface.

These observations suggest that the gate electrode can be approximated by a metal plate for  $d_{ec} \gtrsim w$ . As most of the electrons are channeled through the gate openings and do not reach the gate, this plate can be considered transparent for electrons. Furthermore, the magnetic field forces the electrons onto quasi one-dimensional paths, provided that the radius of gyration is small compared to the mesh diameters.

A current flow between plane-parallel metal plates can be described by a one-dimensional model [29]. In our system, the electrons follow quasi-one-dimensional paths and the electric field can be considered to be generated by a transparent metal plate. I will therefore use a one-dimensional approach in the next chapter to determine the space-charge potential and the current densities in our model system.

### 3 Concept of Thermoelectronic Energy Converters

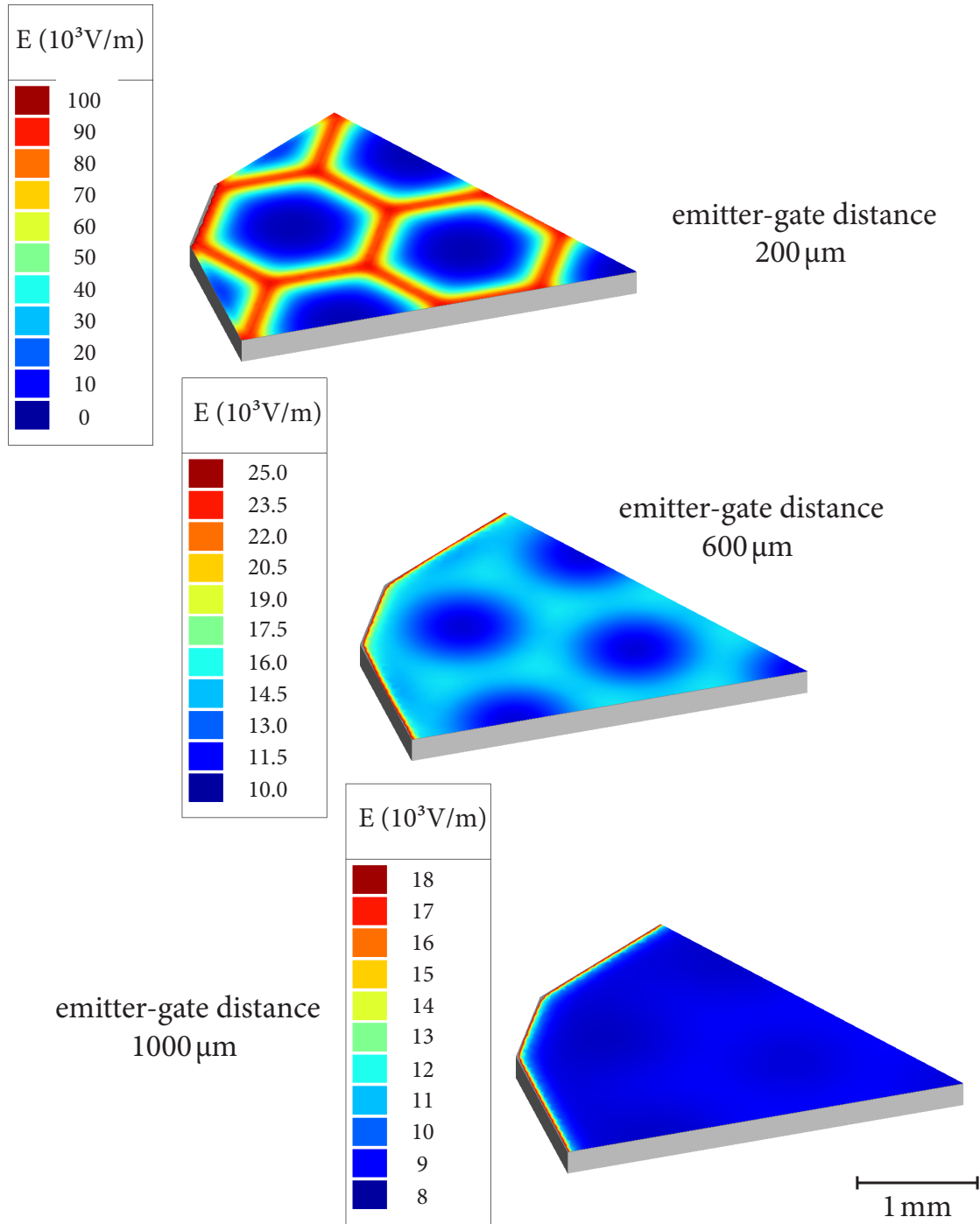


Figure 3.17: Electric field at the emitter surface for three different emitter-gate distances  $d_{eg}$ . The distance is measured from the emitter surface to the center of the gate. The dimensions of the setup are equivalent to the ones used in figure 3.10. The gate-mesh diameter is  $w = 1600 \mu\text{m}$ , the thickness of the gate is  $200 \mu\text{m}$ . For  $d_{eg} = 200 \mu\text{m}$ , the electric field clearly reflects the gate structure. For increasing distances, the field becomes more homogeneous. For a distance of  $d_{eg} = 1000 \mu\text{m}$  the field is virtually uniform on the emitter surface and is equivalent to the field generated by a metal plate. Parameters used:  $V_e = 0 \text{V}$ ,  $V_g = 10 \text{V}$ ,  $V_c = 0 \text{V}$ . A symmetrical setup was considered.

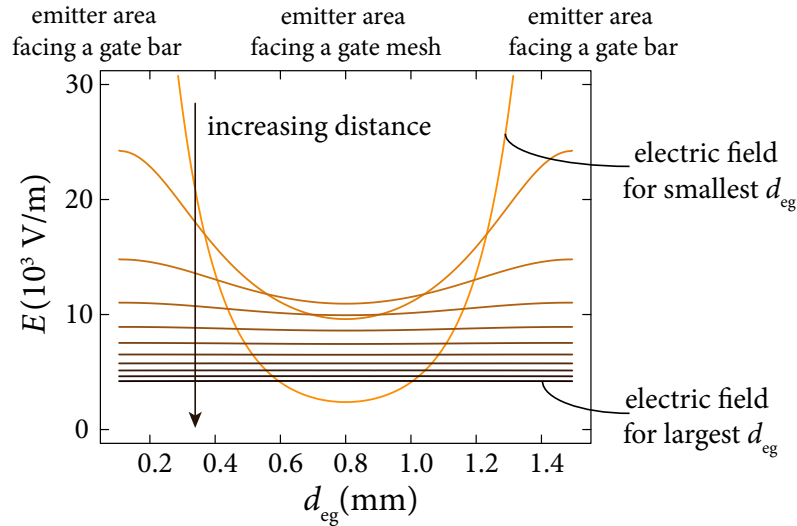


Figure 3.18: Electric field calculated along a line on the emitter surface for different emitter-gate distances  $d_{eg}$ . The distance varies from 200  $\mu\text{m}$  to 2000  $\mu\text{m}$  in steps of 200  $\mu\text{m}$ , measured from the emitter surface to the center of the gate. For very small distances, the electric field at the emitter surface area, which faces the center of the meshes, starts to decrease. Parameters used:  $V_e = 0\text{ V}$ ,  $V_g = 10\text{ V}$ ,  $V_c = 0\text{ V}$ . A symmetrical setup was considered.

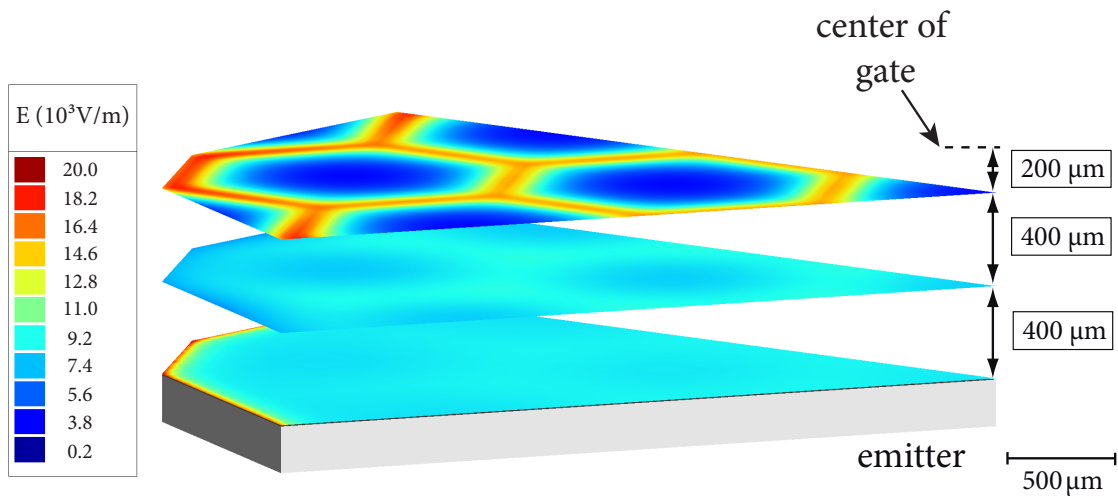


Figure 3.19: Electric field component in longitudinal direction  $E_{\parallel}$  between emitter and gate for a fixed emitter-gate distance of 1000  $\mu\text{m}$ . The mesh width of the gate is 1600  $\mu\text{m}$ . The distance is measured from the emitter surface to the center of the gate.  $E_{\parallel}$  is the field component responsible for accelerating the electrons away from the emitter (see section 3.2). The electric field is virtually uniform in the inter-electrode space, except close to the gate electrode. Parameters used:  $V_e = 0\text{ V}$ ,  $V_g = 10\text{ V}$ ,  $V_c = 0\text{ V}$ . A symmetrical setup was considered.



# 4 One-Dimensional Current Model

A three-dimensional approach has proven to be impractical and not conducive to calculating the space charge and possible current densities in our model system. However, as illustrated in the previous chapter, the electron motion can be mapped onto a one-dimensional system consisting of emitter and collector and a transparent metal plate between them.

In this chapter, I will show how a one-dimensional space-charge model for a transparent gate electrode can be developed, based on established space-charge theories, which have shown great agreement with experimental results. Building on these theories, I will derive the transparent-gate model in several consecutive steps.

Finally, I will present a possible approach to how the model can be expanded to account for inhomogeneities in the electric field generated by the three-dimensional gate electrode.

## 4.1 Basic Principles of One-Dimensional Electrostatic Calculations

The models presented below are based on electrostatic considerations. I consider the magnetic field only to confine the electron motion on quasi one-dimensional paths in the inter-electrode space.

The electrostatic potential, which also defines the electron motion, can be found by solving the Poisson equation

$$\Delta\Phi(x, y, z) = -\frac{\rho_{sc}(x, y, z)}{\epsilon_0}. \quad (4.1)$$

The space-charge density  $\rho_{sc}$  represents the density of charged particles in a volume  $V$  and is given by

$$\rho_{sc}(x, y, z) = \frac{Q(x, y, z)}{V}, \quad (4.2)$$

where  $Q(x, y, z)$  is the total charge.

The space-charge density  $\rho_{sc}(x, y, z)$  on the one hand determines the electrostatic potential  $\Phi(x, y, z)$  and on the other hand is a function of  $\Phi(x, y, z)$  itself. Equation (4.1) is therefore a self consistent differential equation. The solution further depends on the boundary conditions.

#### 4 One-Dimensional Current Model

If the electrostatic potential and the space-charge density are uniform in two directions in space, the Poisson equation can be reduced to one dimension, yielding

$$\frac{d^2\Phi(x)}{dx^2} = -\frac{\rho_{sc}(x)}{\epsilon_0}. \quad (4.3)$$

In this case, the space-charge density is given by

$$\rho_{sc}(x) = \int \frac{j(v_x)}{v_x(x)} dv_x. \quad (4.4)$$

For a uniform velocity  $v_x(x) = \text{const}$ , this equation reduces to

$$\rho(x) = \frac{J}{v_x(x)}. \quad (4.5)$$

$J$  represents the total current density, whereas  $j(v_x)$  represents the contribution to  $J$  of electrons with a specific velocity  $v_x$ .

Equation (4.5) can be understood by considering the well known relation for the current density

$$J = n_e(x)ev_x(x), \quad (4.6)$$

with the electron density  $n_e(x)$ . Combining equations (4.6) and (4.2), while considering  $Q(x) = en_e(x)$ , yields the space-charge density (4.4).

The current density  $J$  in a one-dimensional, electrostatic system is constant, if the charge density is time-independent. This is a direct consequence of the continuity equation

$$\frac{\partial\rho(x, y, z)}{\partial t} + \nabla\mathbf{J} = 0 \quad \xrightarrow{1D} \quad \frac{\partial J}{\partial x} = -\frac{\partial\rho(x)}{\partial t} = 0. \quad (4.7)$$

A plane-parallel thermionic converter can be modeled by two plane-parallel infinite metal plates. In this case, the electrostatic potential and the space charge are uniform in two directions in space and the system can therefore be reduced to a one-dimensional model. Space-charge theories based on this approach have shown great agreement with experimental results [6, 29]. Below I will introduce these theories, which form the basis for the transparent-gate model.

All calculations in this chapter are performed for collisionless, ballistic electron transport. The back emission from the collector is neglected, as its contribution to the current density for efficient TECs is very small (compare chapter 2.5).

To solve the numerical calculations presented, I used Mathematica, version 8.0.1.0 [101]. The according source code is shown in appendix A.1.

## 4.2 Established Space-Charge Theories for Plane-Parallel Converters

### The Child-Langmuir Law

The Child-Langmuir Law, often called Child's Law, describes the space-charge limited current density between two plane-parallel metallic plates when an accelerating voltage is applied to the collector. It was the first space-charge theory to be developed [6]. Although several simplifying assumptions are made, the predicted current densities agree closely with experimental results. The Child-Langmuir Law has become the basis for many algorithms modeling the space charge and electron behavior between metallic electrodes.

The most important result of the Child-Langmuir Law is the dependency of the current density on the applied voltage  $V$  and the distance  $d_{ec}$  between the two plates, *i.e.*

$$J \propto \frac{V^{\frac{3}{2}}}{d_{ec}^2}.$$

Child was the first to derive this relation. In 1911 he published a paper in which he calculated the current of positive ions between two plane-parallel metal plates [34]. Two years later, Langmuir showed that electron current in such a setup shows the same behavior [35].

To calculate the current density, the emitter is considered to be an infinite electron reservoir and the electrons are considered to have no initial kinetic energy. Figure 4.1 shows the inter-electrode potential  $\Phi(x)$  for different current densities. As described in the figure caption, the current density in such a setup adjusts itself so that the derivative of  $\Phi(x)$  at the emitter surface is zero.

The boundary conditions of the Poisson equation are thus given by<sup>1</sup>

$$\Phi(0) = 0 \quad \Phi(d_{ec}) = V \quad \left. \frac{\partial \Phi(x)}{\partial x} \right|_0 = 0. \quad (4.8)$$

The electron velocity  $v_x(x)$  is defined by the kinetic energy  $E_{kin}$ , which depends on the inter-electrode potential

$$v_x(x) = \sqrt{-\frac{2e}{m_e} \Phi(x)}. \quad (4.9)$$

<sup>1</sup>The Poisson equation is a second-order differential equation and can be solved with two boundary conditions. However, the solution for  $\Phi(x)$  would be a function of the current density  $J$ . Applying the condition discussed in figure 4.1, however, leads to a single solution of  $\Phi(x)$  with a specific current density.

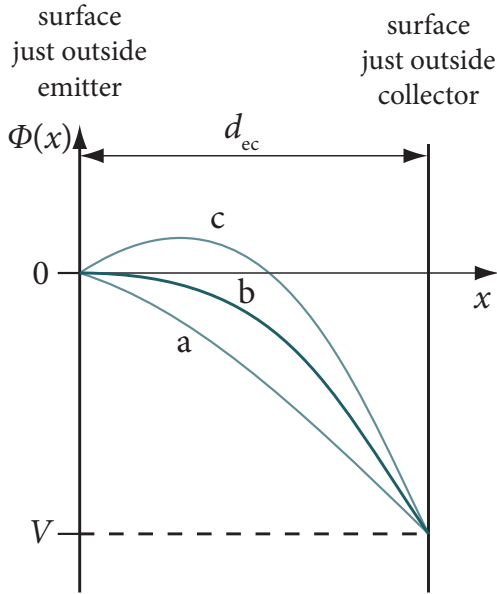


Figure 4.1: Sketch of the inter-electrode potential  $\Phi(x)$  between emitter and collector, to which an accelerating voltage  $V$  is applied. The curves a, b and c represent  $\Phi(x)$  for different current densities  $J$ . If  $J$  is small (curve a), the current increases, as more electrons from the reservoir are accelerated towards the collector. If  $J$  is high (curve c), the electrons cannot overcome the potential maximum, as they have no initial kinetic energy, and  $J$  decreases. The current density therefore adjusts itself so that the derivative of  $\Phi(x)$  at the emitter surface is zero (curve b).

By virtue of equation (4.5), the space-charge density is then given by

$$\rho_{sc}(x) = J \left( -\frac{2e}{m_e} \Phi(x) \right)^{-\frac{1}{2}}. \quad (4.10)$$

Inserting (4.10) into the Poisson equation (4.3) yields the differential equation

$$\Delta \Phi(x) = -\frac{J}{\epsilon_0} \left( -\frac{2e}{m_e} \Phi(x) \right)^{-\frac{1}{2}}. \quad (4.11)$$

This differential equation can be solved by using the identity

$$\frac{\partial}{\partial x} \left( \frac{\partial \Phi(x)}{\partial x} \right)^2 = 2 \frac{\partial \Phi(x)}{\partial x} \frac{\partial^2 \Phi(x)}{\partial x^2},$$

and defining the help function

$$\frac{\partial f}{\partial \Phi(x)} := -\frac{J}{\epsilon_0} \left( -\frac{2e}{m_e} \Phi(x) \right)^{-\frac{1}{2}}.$$

By integrating over  $x$  and applying the third boundary condition of (4.8), it follows that

$$\frac{\partial \Phi}{\partial x} = f^{\frac{1}{2}} = \frac{4J}{\epsilon_0} \left( \frac{m_e \Phi(x)}{2e} \right)^{\frac{1}{4}}.$$

Separation of variables, integration and the use of the other two boundary conditions finally leads to

$$\Phi(x) = \frac{V_d}{d_{ec}^{\frac{4}{3}}} x^{\frac{4}{3}}, \quad (4.12)$$

$$J = \frac{4}{9} \epsilon_0 \left( \frac{2e}{m_e} \right)^{\frac{1}{2}} \frac{V_d^{\frac{3}{2}}}{d_{ec}^2}. \quad (4.13)$$

The Child-Langmuir Law has several limitations. Because it treats the emitter as an infinite electron reservoir, it does not describe the transition into the saturation current density, which is given by the Richardson-Dushman equation (2.4). Furthermore, it is clearly wrong for  $V = 0$ , because it predicts no current to flow in this case. Assuming the electrons to have no initial velocity is a good approximation for strong voltages, as the kinetic energy in this regime is dominated by the generated electric field. For small accelerating voltages, however, the initial velocity is an important part of the electron energy. In this voltage regime, the Child-Langmuir Law is not a good approximation.

### Introducing the Velocity Distribution - The Langmuir Theory

Langmuir expanded the model to include the velocity distribution of the emitted electrons [102]<sup>2</sup>. As Hatsopoulos illustrates in reference [29], the values calculated using the Langmuir theory show close agreement with experimental results.

To derive the space-charge potential and the current density, I will partly follow the course of Langmuir [102] and Hatsopoulos [29]. I will further present an alternative way of approaching the model and deriving the differential equation for the space-charge potential. The considerations in this chapter are fundamental to the ‘ideal gate’ model, which I will introduce later in this chapter.

I shall consider a plane-parallel setup with emitter and collector on the same electrostatic potential, corresponding to the ideal converter configuration (2.13). The inter-electrode electrostatic potential is caused only by the charges of the electrons and is therefore equivalent to the space-charge potential  $\Phi_{sc}(x)$ .

The starting point is the Poisson equation, given by

$$\Delta \Phi_{sc}(x) = -\frac{\rho_{sc}(x)}{\epsilon_0}. \quad (4.14)$$

---

<sup>2</sup>A space-charge theory between two plane-parallel infinite metallic plates including the electron velocity distribution was first developed by Epstein and Fry, but there were several errors in their derivations (according to Langmuir [102]). The first correct calculations were performed by Adams, at the request of Langmuir. Adams, however, failed to publish his results, which Langmuir then did in 1923.

#### 4 One-Dimensional Current Model

To solve the Poisson equation, the first step is to express the space-charge density  $\rho_{sc}$  in terms of  $\Phi_{sc}$ . The space-charge density at a point  $x$  can be calculated by integrating the velocity distribution  $f_e(v_x, x)$  over all velocities

$$\rho_{sc}(x) = en_0 \int f_e(v_x, x) dv_x, \quad (4.15)$$

where  $n_0$  is the particle density at  $x = 0$ .

Hatsopoulos shows that the electron distribution function  $f_e(v_x, x)$  is a solution of the Boltzmann equation [29]. He obtains the space-charge density

$$\rho_{sc}(x) = 2 \left( \frac{m_e}{2\pi k_B T} \right)^{\frac{1}{2}} \int dv_x e^{-\frac{e\Phi(x)}{k_B T} - \frac{v_x^2}{2k_B T}}. \quad (4.16)$$

I will now demonstrate that the space-charge density can also be obtained by a more direct approach, based solely on fundamental principles discussed earlier.

The velocity distribution of thermally emitted electrons, as shown in chapter 2.4, is given by a 'Half-Maxwellian' distribution. For a one-dimensional system, the distribution reduces to

$$f_h(v_x) = \begin{cases} 2 \left( \frac{m_e}{2\pi k_B T} \right)^{\frac{1}{2}} e^{-\frac{m_e v_x^2}{2k_B T}} & \text{for } x \geq 0 \\ 0 & \text{for } x < 0 \end{cases}. \quad (4.17)$$

This distribution is only valid directly at the emitter surface. In the inter-electrode space, it is modified by the space-charge potential  $\Phi_{sc}(x)$ . As a consequence,  $f_e(v_x, x)$  is only normalized at  $x = 0$ .

The space charge  $\rho_{sc}$  is given by

$$\rho_{sc}(x) = \int \frac{j(v_x)}{v_x(x)} dv_x. \quad (4.18)$$

The differential current density  $j(v_x)$  is defined by

$$j(v_x) = e\eta_e(v_x, x)v_x(x), \quad (4.19)$$

where  $\eta_e(v_x, x)$  represents the electron density at a point  $x$  of electrons with the velocity  $v_x(x)$

$$\eta_e(v_x, x) = n_0 f_e(v_x, x). \quad (4.20)$$

The electron velocity  $v_x(x)$  is defined by the kinetic energy, which depends on the inter-electrode potential and the initial electron velocity

$$v_x(x) = \sqrt{-\frac{2}{m_e} e\Phi(x) + v_0^2}. \quad (4.21)$$

Changing the integration variable in equation (4.18) from  $dv_x$  to  $dv_{x0}$  by using the identity

$$dv_x j(v_x) = en_0 v_x(x) f_e(v_x, x) dv_x = en_0 f_e(x, v_{x0}) v_{x0} dv_{x0} = en_0 v_{x0} f_h(v_{x0}) dv_{x0}, \quad (4.22)$$

allows me to introduce the Half Maxwellian velocity distribution (4.17)  $f_h(v_{x0})$  into the space-charge density.

Changing the integration variable back again leads to

$$\rho_{sc}(x) = 2 \left( \frac{m_e}{2\pi k_B T} \right)^{\frac{1}{2}} \int dv_x e^{-\frac{e\Phi(x)}{k_B T} - \frac{v_x^2}{2k_B T}}. \quad (4.23)$$

Through these steps, I replaced the unknown velocity distribution in the inter-electrode space by the known velocity distribution  $f_h(v_{x0})$ , which is independent of  $x$ . The resulting space-charge density (4.23) is equivalent to expression (4.16) derived by Hatsopoulos.

The next step in calculating  $\rho_{sc}$  is to determine the integration limits. The Poisson equation (4.14) indicates that the curvature of  $\Phi_{sc}(x)$  is always downwards. As  $\Phi_{sc}(x)$  is fixed at the emitter and the collector surface, it always forms a maximum  $\Phi_{sc,max}$  at  $x = x_{max}$  (figure 4.2).

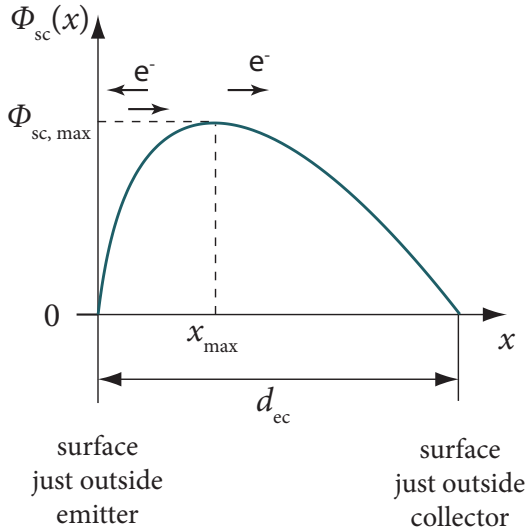


Figure 4.2: Typical form of the space-charge potential  $\Phi_{sc}(x)$ , when emitter and collector are on the same electrostatic potential.  $\Phi_{sc}(x)$  always forms a maximum  $\Phi_{sc,max}$  at  $x = x_{max}$ . For  $x < x_{max}$  electrons move in both directions, as part of the electrons are turned back. For  $x > x_{max}$  electrons move only in positive  $x$ -direction. The potential was calculated using the typical parameters  $\phi_e = 2.5$  eV,  $T_e = 1500$  K,  $d_{ec} = 100$   $\mu\text{m}$ .

A fraction of the electrons lacks the energy to overcome the space-charge maximum and turns back to the emitter. For  $x < x_{max}$ , electrons therefore move in both directions, whereas for  $x > x_{max}$  electrons move only in positive  $x$ -direction.

For  $x > x_{max}$ , electrons with the lowest velocity in positive  $x$ -direction are those that reach  $\Phi_{sc,max}$  with zero velocity and are then accelerated towards the collector. These electrons have the velocity

$$v_{x,min}(x) := \left( \frac{2e}{m_e} (\Phi_m - \Phi(x)) \right)^{\frac{1}{2}}. \quad (4.24)$$

#### 4 One-Dimensional Current Model

It follows that for  $x \geq x_{\max}$ , electrons have velocities in the range of

$$v_{x,\min}(x) < v_x(x) < \infty \quad \text{for } x \geq x_{\max}. \quad (4.25)$$

For  $x < x_{\max}$ , electrons with the highest velocity in negative x-direction are those that reach  $\Phi_{\text{sc,max}}$  with zero velocity and are then accelerated towards the emitter. These electrons have the velocity  $-v_{x,\min}(x)$ . This means that for  $x < x_{\max}$ , electrons have velocities in the range of

$$-v_{x,\min}(x) < v_x(x) < \infty \quad \text{for } x < x_{\max}. \quad (4.26)$$

By virtue of equation (4.23) and using the integration limits (4.25) and (4.26), the space-charge density in the inter-electrode space is therefore given by

$$\rho_{\text{sc}}(x) = 2en_0 \left( \frac{m_e}{2\pi k_B T} \right)^{\frac{1}{2}} e^{-\frac{e\Phi(x)}{k_B T}} \begin{cases} \int_{-v_{x,\min}(x)}^{\infty} dv_x e^{-\frac{v_x^2}{2k_B T}} & \text{for } x < x_{\max} \\ \int_{v_{x,\min}(x)}^{\infty} dv_x e^{-\frac{v_x^2}{2k_B T}} & \text{for } x \geq x_{\max} \end{cases}. \quad (4.27)$$

Using the substitutions

$$t^2 = \frac{m_e v_x(x)^2}{2k_B T}, \quad (4.28)$$

$$\gamma(x) = \frac{e}{k_B T} (\Phi_{\max} - \Phi(x)), \quad (4.29)$$

leads to

$$\rho_{\text{sc}}(x) = 2en_0 \frac{1}{\pi^{\frac{1}{2}}} e^{-\frac{e\Phi(x)}{k_B T}} \begin{cases} \int_{-\gamma(x)^{\frac{1}{2}}}^{\infty} dt e^{-t^2} & \text{for } x < x_{\max} \\ \int_{\gamma(x)^{\frac{1}{2}}}^{\infty} dt e^{-t^2} & \text{for } x \geq x_{\max} \end{cases}. \quad (4.30)$$

This equation can be simplified by using the Gaussian integral and the error function [103]

$$\int_0^{\infty} dt e^{-t^2} = \frac{\pi^{\frac{1}{2}}}{2} \quad \text{and} \quad \int_0^{\gamma(x)^{\frac{1}{2}}} dt e^{-t^2} = \frac{\pi^{\frac{1}{2}}}{2} \text{erf} \left[ \gamma(x)^{\frac{1}{2}} \right]. \quad (4.31)$$

Inserting the space-charge density into the Poisson equation (4.14) finally yields the self-consistent differential equation

$$\Delta\Phi_{\text{sc}}(x) = -\frac{en_0}{\epsilon_0} \exp\left[-\frac{e}{k_{\text{B}}T}\Phi(x)\right] \left\{1 \pm \operatorname{erf}\left[\left(\frac{e}{k_{\text{B}}T}(\Phi_{\text{max}} - \Phi(x))\right)^{\frac{1}{2}}\right]\right\}. \quad (4.32)$$

The plus and minus signs indicate  $x \leq x_{\text{max}}$  and  $x \geq x_{\text{max}}$ , respectively.

The boundary conditions for equation (4.32) are given by the electrostatic potentials of emitter and collector

$$\Phi_{\text{sc}}(0) = 0 \quad \text{and} \quad \Phi_{\text{sc}}(x_{\text{c}}) = 0. \quad (4.33)$$

The electron density  $n_0$  at  $x = 0$  can be computed by considering that the saturation current density  $J_{\text{s}}$ , defined by the Richardson-Dushman current density  $J_{\text{RD}}$ , can be calculated by

$$J_{\text{s}} = en_0 \int_0^{\infty} dv_{x0} f_{\text{h}}(v_x) v_{x0} = en_0 \left(\frac{2k_{\text{B}}T}{\pi m_{\text{e}}}\right)^{\frac{1}{2}}. \quad (4.34)$$

Solving equation (4.34) for  $n_0$  with  $J_{\text{s}} \equiv J_{\text{RD}}$  yields

$$n_0 = \frac{J_{\text{RD}}(\phi_{\text{e}}, T_{\text{e}})}{e} \left(\frac{\pi m_{\text{e}}}{2k_{\text{B}}T_{\text{e}}}\right)^{\frac{1}{2}}. \quad (4.35)$$

$n_0$  depends on the saturation current, and is thus a function of the emitter temperature  $T_{\text{e}}$  and the emitter work function  $\phi_{\text{e}}$ .

The differential equation (4.32) can be solved numerically, yielding the space-charge potential  $\Phi_{\text{sc}}(x)$ . The current density in the system can then be calculated by the fraction of the electrons overcoming the space-charge maximum  $\Phi_{\text{sc,max}}$ , leading to

$$J = J_{\text{s}} e^{-e\Phi_{\text{sc,max}}/k_{\text{B}}T_{\text{e}}}. \quad (4.36)$$

These calculations enable us to predict the current density for plane-parallel converters for different setup parameters: the collector temperature  $T_{\text{c}}$ , the collector work function and the emitter-collector distance  $d_{\text{ec}}$ . As back emission is not considered, the collector work function and temperature do not influence the results. They do, however, influence the output power, as the load voltage depends on  $\phi_{\text{c}}$ .

The Langmuir theory can be used to show that  $J$  increases for decreasing  $d_{\text{ec}}$ . The values displayed in figure 2.4 in chapter 2.1, illustrating the ‘close-space approach’, were calculated using this theory.

Within the Langmuir theory, it is also possible to investigate the influence of the emitter temperature and the emission properties on the current density for conventional vacuum converters. Figure 4.3 shows  $J$  as a function of  $T_{\text{e}}$  for an emitter-collector distance of 100  $\mu\text{m}$ . Although  $J$  increases with  $T_{\text{e}}$ , no significant current can be generated.

#### 4 One-Dimensional Current Model

To investigate the current density for materials with different emission characteristics, a coefficient  $\epsilon_{RD}$  is introduced. This coefficient is a simple factor modifying the Richardson-Dushman constant  $A_{RD}$  (2.5). A high value of  $\epsilon_{RD}$  therefore indicates a material with high emission properties. Figure 4.4 shows  $J$  as a function of  $\epsilon_{RD}$  for a setup with an emitter-collector distance of  $d_{ec} = 100 \mu\text{m}$ . The graph illustrates that no significant currents can be obtained for such a setup, even with an emitter material that yields an emission current 20 times higher than the conventional Richardson-Dushman current.

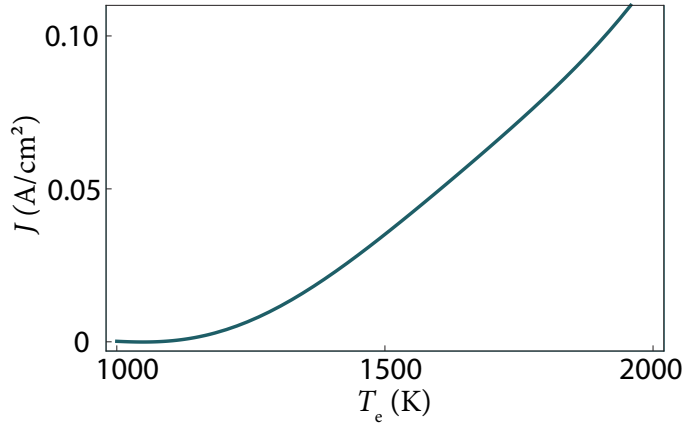


Figure 4.3: Current density  $J$  as a function of the emitter temperature  $T_e$  for a converter with emitter-collector distance  $d_{ec} = 100 \mu\text{m}$  and emitter work function of  $\phi_e = 2.5 \text{ eV}$ . Even for high applied temperatures, no significant current density is obtained.

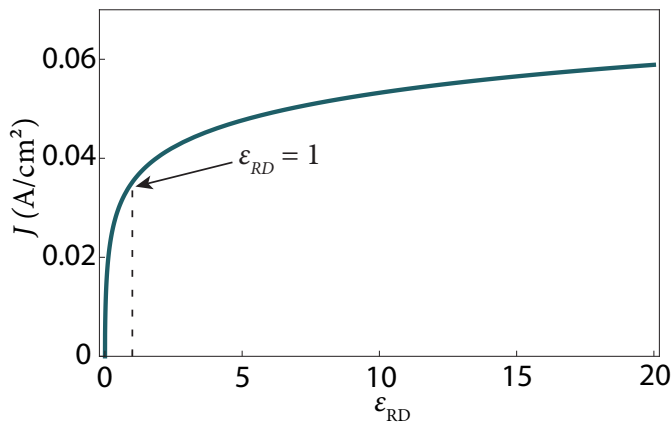


Figure 4.4: Current density  $J$  as a function of a Richardson-Dushman coefficient  $\epsilon_{RD}$  for a converter with emitter-collector distance  $d_{ec} = 100 \mu\text{m}$ , an emitter work function  $\phi_e = 2.5 \text{ eV}$  and an emitter temperature of  $T_e = 1500 \text{ K}$ . Even for high values of  $\epsilon_{RD}$ , indicating high electron emission currents, no significant current density is obtained.

These results clearly demonstrate that a high current density cannot be achieved in conventional vacuum converters by simply optimizing the emitter characteristics or increasing the temperature.

### 4.3 Model for an Ideal Gate

An ideal gate is a metal plate that is transparent for electrons and creates a homogeneous electric field. This model is a theoretical idealization, since electrons cannot pass through a metal plate. However, as shown in chapter 3.4, a metal grid in sufficient distance from the emitter can be approximated by an ideal gate model.

I shall consider emitter and collector to be two plane-parallel infinite metal plates on the same electrostatic potential. An ideal gate with the applied voltage  $V_g$  at the position  $x_g$  creates the potential

$$\Phi_g(x) = \begin{cases} -\frac{V_g}{x_g}x & \text{for } x \leq x_g \\ -\frac{V_g}{x_c - x_g}(x_c - x) & \text{for } x \geq x_g \end{cases}, \quad (4.37)$$

where  $x_c$  indicates the collector position. Figure 4.5 shows the gate potential for a symmetrical configuration with  $x_g = d_{ec}/2$ .

The total inter-electrode electrostatic potential  $\Psi(x)$  consists of the gate potential  $\Phi_g(x)$  and the space-charge potential  $\Phi_{sc}(x)$

$$\Psi(x) = \Phi_g(x) + \Phi_{sc}(x). \quad (4.38)$$

It is found by solving the one-dimensional Poisson equation (4.3). The gate potential  $\Phi_g(x)$  is not continuously differentiable at  $x = x_g$ . The space-charge potential, however, must be continuously differentiable at  $x = x_g$ .

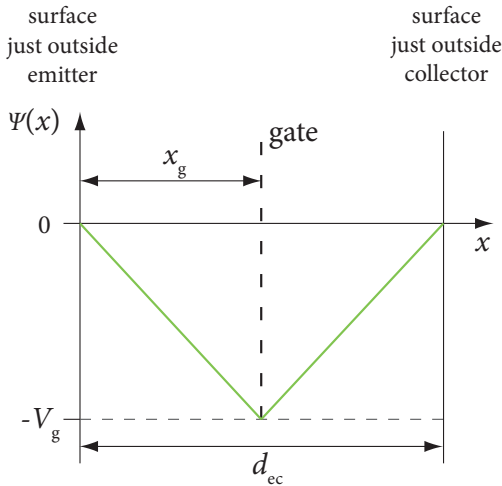


Figure 4.5: Potential of an ideal transparent gate for a geometrical symmetrical setup, which represents the optimal geometrical configuration for thermoelectronic energy converters.

The symmetrical setup, with the gate electrode mounted exactly in the middle between emitter and collector, represents the optimal geometrical configuration for thermoelectronic converters<sup>3</sup>. This can be understood from the following example:

A converter with a symmetrical setup is considered. The gate potential is chosen just strong enough so that the inter-electrode potential  $\Psi(x)$  does not form a maximum. In this case,  $\Phi_g(x)$  and  $\Psi(x)$  are symmetrical (figure 4.6 (a)). It further needs to be considered that the space-charge density determines the curvature of the inter-electrode electrostatic potential  $\Psi(x)$ , as shown by the Poisson equation (4.3), and that increasing the electron velocity results in a weaker space-charge potential.

- If the gate is moved closer to the emitter, while the emitter-collector distance  $d_{ec}$  is kept constant (figure 4.6 (b)), the gate electric field between emitter and gate is increased, leading to a weaker space-charge potential  $\Phi_{sc}(x)$ . On the other hand, the electric field in the gray-shaded area in figure 4.6 (b) is weaker than before, leading to a higher space-charge density in this region. The curvature of  $\Psi(x)$  is therefore increased. As  $\Psi(x)$  is fixed at the emitter and collector surfaces and the gate potential is weaker in the gray-shaded area, the total potential is stronger than before and forms a maximum, which leads to a lower current density. Moving the gate closer to the collector while keeping  $d_{ec}$  constant, leads to the same effect.
- If  $d_{ec}$  is increased while the emitter-gate distance is kept constant (figure 4.6 (c)), the gate electric field in the grey shaded area in figure 4.6 (c) becomes weaker. This again leads to a maximum of the total potential and consequently to a lower current density.

The maximum current density is therefore obtained for the symmetrical configuration.

In the calculations presented below, I will only consider the symmetrical setup. The gate potential in this case is given by

$$\Phi_g(x) = \begin{cases} -\frac{V_g}{x_g}x & \text{for } x \leq x_g \\ -\frac{V_g}{x_g}(x_c - x) & \text{for } x \geq x_g \end{cases}. \quad (4.39)$$

The resulting electric field is constant

$$E_g = -\frac{\partial\Phi}{\partial x} = \begin{cases} \frac{V_g}{x_g} = \text{const} & \text{for } x \leq x_g \\ -\frac{V_g}{x_g} = \text{const} & \text{for } x \geq x_g \end{cases}. \quad (4.40)$$

In the following sections, I will develop the transparent model in several consecutive steps, to arrive at a formulation that includes the electron velocity distribution and represents the full description of the system within an electrostatic approach.

<sup>3</sup>For a strong space-charge potential, the optimal configuration can deviate slightly from the symmetrical configuration. However, the gate position  $x_g = d_{ec}/2$  is very close to the optimal gate position.

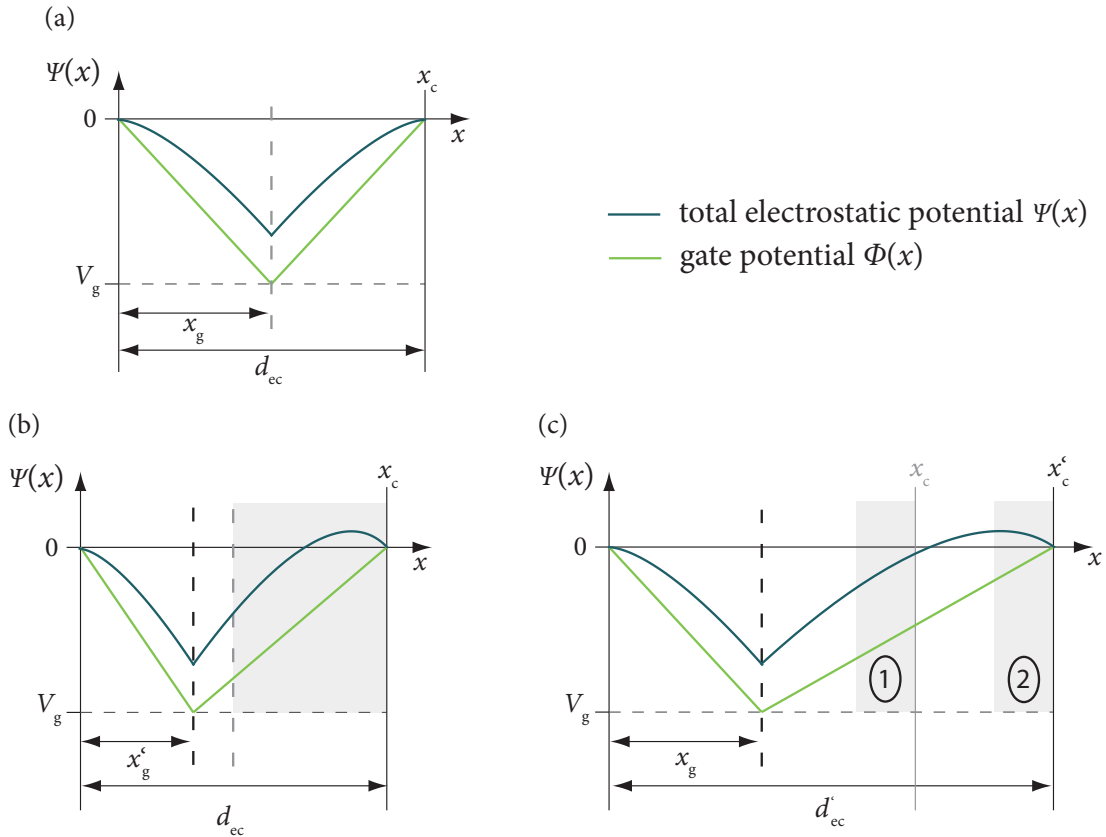


Figure 4.6: The electrostatic potential of the gate  $\Phi_g(x)$  and the total electrostatic potential  $\Psi(x)$  shown for different geometrical configurations. (a) symmetrical setup; the gate potential is just strong enough so that  $\Psi(x)$  forms no peak in the inter-electrode space. (b) If the gate is moved closer to the emitter, while the total distance  $d_{ec}$  is kept constant, a peak in  $\Psi(x)$  is formed, leading to a lower current density. (c) If the collector is moved away from the gate, while the emitter-gate distance is kept constant, a peak in  $\Psi(x)$  is formed, leading to a lower current density. The optimal geometrical configuration, which yields the highest current density, therefore corresponds to the symmetrical setup shown in case (a).

### A First Approach - Neglecting the Influence of the Space Charge on the Electron Velocity

As a first step, I shall consider the simplified case that the electron motion is only determined by the electric field generated by the gate electrode, neglecting the influence of the space-charge potential. This approximation can be valid for very strong applied voltages. Analogous to the considerations leading to the Child-Langmuir Law, I assume the emitter to be an infinite electron reservoir with no initial kinetic energy.

The symmetrical gate potential implies a symmetrical space-charge potential. It is therefore sufficient to solve the Poisson equation for only half of the setup, e.g., for  $x \leq x_g$ . The solution for the second part is obtained by substituting  $x \rightarrow (x_c - x)$ .

#### 4 One-Dimensional Current Model

The electron velocity is given by

$$v_x(x) = \sqrt{2ax}, \quad (4.41)$$

where  $a$  is the acceleration by the electric field

$$a = \frac{eE_g}{m_e}. \quad (4.42)$$

By virtue of (4.5), the space-charge density is given by

$$\rho_{sc}(x) = \frac{J}{v_x(x)} = \frac{J}{\sqrt{2ax}}. \quad (4.43)$$

The Poisson equation (4.3) then becomes

$$\frac{\partial^2 \Psi(x)}{\partial x^2} = -\frac{J}{\epsilon_0} \frac{1}{\sqrt{2ax}}. \quad (4.44)$$

Analogous to the arguments discussed on page 59, the current density adjusts itself so that

$$\left. \frac{\partial \Psi(x)}{\partial x} \right|_0 = 0. \quad (4.45)$$

The other boundary conditions are defined by the electrostatic emitter potential and the symmetrical configuration, leading to

$$\Psi(x) = \Phi_{sc}(0) = 0 \quad (4.46)$$

$$\left. \frac{\partial \Phi_{sc}(x)}{\partial x} \right|_{x_g} = 0 \Rightarrow \left. \frac{\partial \Psi(x)}{\partial x} \right|_{x_g} = -E_g. \quad (4.47)$$

Using these boundary conditions, equation (4.44) can be solved, yielding the the space-charge potential and the current density

$$\Phi_{sc}(x) = \begin{cases} -\frac{2}{3} \frac{V_g}{x_g^{\frac{3}{2}}} x^{\frac{3}{2}} + \frac{V_g}{x_g} x & \text{for } x \leq x_g \\ -\frac{2}{3} \frac{V_g}{x_g^{\frac{3}{2}}} (x_c - x)^{\frac{3}{2}} + \frac{V_g}{x_g} (x_c - x) & \text{for } x \geq x_g \end{cases}, \quad (4.48)$$

$$J = \epsilon_0 \left( \frac{e}{2m_e} \right)^{\frac{1}{2}} \frac{V_g^{\frac{3}{2}}}{x_g^2}. \quad (4.49)$$

The current density shows the same behavior  $J \propto V_g/x_g^2$  as the Child-Langmuir Law.

### Electrons With Uniform Velocity

As a next step, I will include the influence of the space-charge potential on the electron velocity. I will not yet include the thermal velocity distribution, but consider all electrons to have a uniform velocity. This simplification is similar to the considerations leading to the Child-Langmuir Law and yields important results for the ideal-gate model.

Analogous to the previous section, it is sufficient to calculate only half of the symmetrical solution, while the second half can be obtained by substituting  $x \rightarrow (x_c - x)$ . The emitter is again considered to be an infinite electron reservoir.

Analogous to the considerations for the Child-Langmuir Law (see section 4.2 on page 59), the current adjusts itself so that<sup>4</sup>

$$\left. \frac{\partial \Psi(x)}{\partial x} \right|_0 = 0. \quad (4.50)$$

The other boundary conditions are defined by the electrostatic potential of the emitter and the symmetrical setup

$$\Psi(x) = \Phi_{sc}(0) = 0, \quad (4.51)$$

$$\left. \frac{\partial \Phi_{sc}(x)}{\partial x} \right|_{x_g} = 0 \Rightarrow \left. \frac{\partial \Psi(x)}{\partial x} \right|_{x_g} = -E_g. \quad (4.52)$$

The kinetic energy of the electrons is given by

$$E_{kin}(x) = -e\Psi(x) + E_{kin,0}, \quad (4.53)$$

which leads, by virtue of (4.5), to the space-charge density

$$\rho_{sc}(x) = \frac{J}{\sqrt{2/m_e (-e\Psi(x) + E_{kin,0})}}, \quad (4.54)$$

and the Poisson equation

$$\Delta \Psi(x) = -\frac{J}{\varepsilon_0} \left( \frac{2e}{m_e} (-\Psi(x)) + \frac{2}{m_e} E_{kin,0} \right)^{-\frac{1}{2}}. \quad (4.55)$$

### Electrons without Initial Kinetic Energy

First, I shall consider electrons with no initial velocity, the same case as considered in the Child-Langmuir Law. Equation (4.53) shows that this assumption is a good approximation for strong gate fields, *i.e.*  $e\Psi(x) \gg E_{kin,0}$ .

<sup>4</sup>For a finite initial kinetic energy, the current density could be higher. The condition is strictly correct for  $E_{kin,0} = 0$ . For  $E_{kin,0} > 0$ , it leads to a current density  $J$  that slightly underestimates the actual current density in the system.

#### 4 One-Dimensional Current Model

In this case, equation (4.55) can be solved analogous to equation (4.11). By the use of an auxiliary function, separation of variables and integration by parts, the following general solution is obtained

$$\frac{\sqrt{\frac{4A}{\sqrt{B}} \sqrt{-\Psi(x)} + C_1} (C_1 B - 2A \sqrt{B} \sqrt{-\Psi(x)})}{6A^2} = x + C_2, \quad (4.56)$$

where  $A = J/\varepsilon_0$ ,  $B = 2e/m_e$  and  $C_1$  and  $C_2$  represent the two integration constants.

This equation can be solved for  $\Psi(x)$ , leading to a very complex expression. However, using the boundary conditions (4.50), (4.51) and (4.52), the two integration constants  $C_1$  and  $C_2$  both vanish, *i.e.*  $C_1 = C_2 = 0$ , leading to the solution

$$\Psi(x) = -\frac{3}{4} \frac{V_g}{x_g^{\frac{4}{3}}} x^{\frac{4}{3}}, \quad (4.57)$$

$$\Phi_{sc}(x) = \frac{V_g}{x_g} x - \frac{3}{4} \frac{V_g}{x_g^{\frac{4}{3}}} x^{\frac{4}{3}}, \quad (4.58)$$

$$J = \frac{\varepsilon_0}{\sqrt{6}} \left( \frac{e}{m_e} \right)^{\frac{1}{2}} \frac{V_g^{\frac{3}{2}}}{x_g^2}. \quad (4.59)$$

Remarkably, the current density shows the same behavior as the Child-Langmuir Law (4.13)

$$J \propto \frac{V_g^{\frac{3}{2}}}{x_g^2}. \quad (4.60)$$

The strength of the current density is only weaker by a factor of  $\sqrt{3} \approx 1.73$ .

The current density (4.59) is a very important result within the ideal-gate model. It constitutes a lower limit for  $J$  in the model system for a given emitter-collector distance and an applied gate voltage. The electrons are assumed to have no initial kinetic energy. Accounting for the initial electron velocity would result in a lower space charge. Furthermore, for this value of  $J$ , all emitted electrons reach the collector, as the inter-electrode motive does not form a maximum due to the boundary condition (4.50). Increasing  $J$  would result in a potential peak and a fraction of the electrons would not reach the collector, even considering the thermal velocity distribution.

Equation (4.59) further enables us to calculate the voltage  $V_g$  that is needed to reduce the space charge so that all electrons reach the collector in a thermoelectronic converter for a given current density.

$$V_g = \left( \frac{J}{\varepsilon_0} \right)^{\frac{2}{3}} \left( \frac{6m_e}{e} \right)^{\frac{1}{3}} x_g^{\frac{4}{3}}. \quad (4.61)$$

This result can also be expressed in terms of the electric field

$$E_g = \frac{V_g}{x_g} = \left( \frac{J}{\epsilon_0} \right)^{\frac{2}{3}} \left( \frac{6m_e}{e} \right)^{\frac{1}{3}} x_g^{\frac{1}{3}}. \quad (4.62)$$

Figure 4.7 shows the electric field required to reduce the space-charge potential so that all emitted electrons reach the collector as a function of  $d_{ec}$ . The electric field is shown for the examples of current densities of  $10 \text{ A/cm}^2$  and  $20 \text{ A/cm}^2$ . The electric field decreases for decreasing distance. This means that for decreasing distances, lower applied gate voltages are required for all emitted electrons to reach the collector.

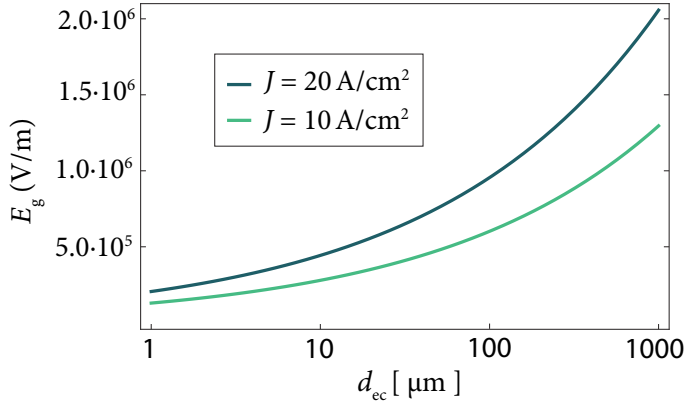


Figure 4.7: Electric field  $E_g$  that is required to reduce the space-charge potential so that all emitted electrons reach the collector, shown as a function of the emitter-collector distance  $d_{ec}$  for two different current densities. The electric field decreases for decreasing distance.

### Electrons with a Uniform Initial Velocity

If a finite, uniform initial velocity is included, equation (4.55) cannot be solved analytically. By using the boundary conditions (4.50), (4.51) and (4.52), however, a numerical solution can be found.

To determine the initial velocity, I used the thermal mean value of the kinetic energy of emitted electrons (compare chapter 2.4). Using this mean value only yields a first approximation. For a correct thermal averaging, it is not the mean value of the electron velocity or the kinetic energy, which has to be calculated, but that of the contribution to the space-charge density of each electron. This will be done in a next step, by introducing the electron velocity distribution. Including a mean thermal velocity nonetheless yields a good indication for the influence of the thermal energy on the current density.

Figures 4.8, 4.9 and 4.10 show the current densities for both solutions for electrons with and without an initial velocity, depending on different setup parameters. In all three cases, including an initial velocity leads to higher current densities. Both models, however, yield results that are of the same order of magnitude.

Investigating the current density as a function of the emitter-collector distance for both models reveals that the ratio of both results is constant (figure 4.8). This means that both scale with  $1/d_{ec}^2$ .

For the gate voltage  $V_g$ , the results show a different behavior (figure 4.9). For small values of  $V_g$ , the influence of the thermal energy is considerably stronger. For increasing  $V_g$ , the

influence diminishes, as the ratio approaches 1. This can be understood by considering the kinetic energy (4.53). Both the gate voltage and the initial energy increase to total kinetic energy. For small applied voltages,  $E_{\text{kin},0}$  dominates the kinetic energy of the electrons.

The model with no initial energy does not depend on the emitter temperature  $T_e$ . The current density obtained when including a uniform thermal velocity increases slowly for increasing  $T_e$  (figure 4.10).

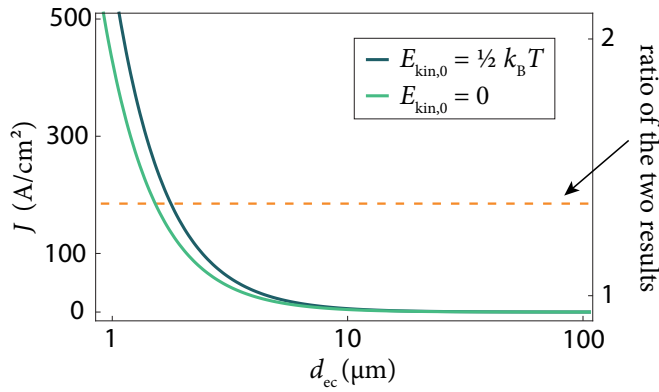


Figure 4.8: Current density as a function of the emitter-collector distance  $d_{\text{ec}}$  for electrons with and without a uniform initial kinetic energy. The dashed line indicates the ratio of the two results. As the ratio is constant, both results scale as  $1/d_{\text{ec}}^2$ . The following parameters were used:  $V_g = 2 \text{ V}$ ,  $T_e = 1500 \text{ K}$ .

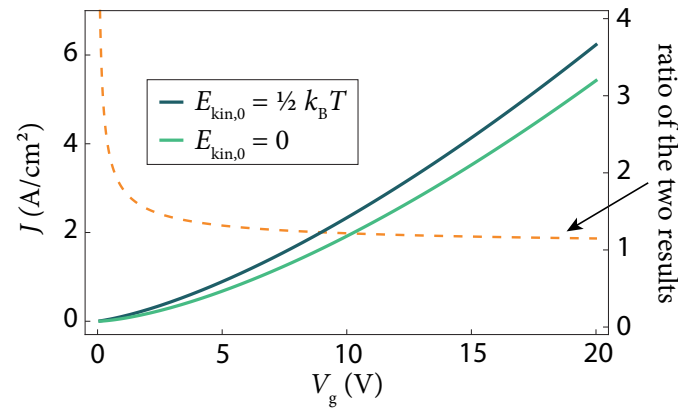


Figure 4.9: Current density as a function of the gate voltage  $V_g$  for electrons with and without a uniform initial kinetic energy. The dashed line indicates the ratio of both results. The influence of the thermal energy vanishes for high applied voltages. The following parameters were used:  $d_{\text{ec}} = 100 \mu\text{m}$ ,  $T_e = 1500 \text{ K}$ .

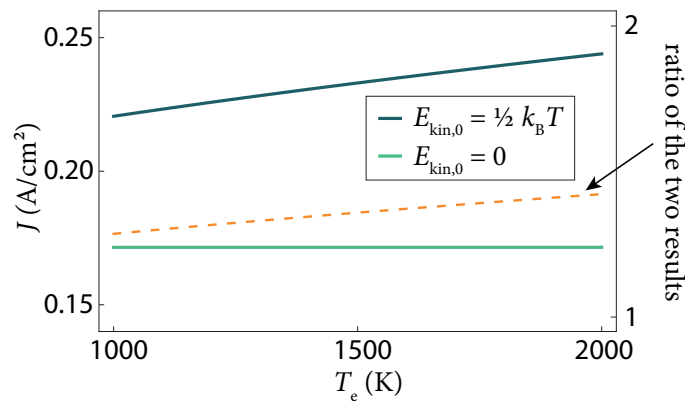


Figure 4.10: Current density as a function of the emitter temperature  $T_e$  for electrons with and without a uniform initial kinetic energy. The dashed line indicates the ratio of both results. The following parameters were used:  $d_{\text{ec}} = 100 \mu\text{m}$ ,  $V_g = 2 \text{ V}$ .

### Including the Electron Velocity Distribution in the Ideal-Gate Model - An Expansion of the Langmuir Theory

For a complete description of the ideal-gate model, the velocity distribution of the emitted electrons needs to be included. I will use the Langmuir theory and the calculations presented in chapter 4.2 as a basis, and expand them to include the gate potential  $\Phi_g(x)$ . The numerical solution of the self-consistent Poisson equation is more complex for the ideal-gate model, especially due to the discontinuity of  $\Phi_g(x)$  at  $x = x_g$ .

A similar approach for an ideal gate has been performed by Ramberg *et al.* in reference [104]. This publication has drawn little interest, and is not relevant to my calculations.

The gate potential (4.39) can be expressed as

$$\Phi_g(x) = \begin{cases} -\frac{V_g}{x_g}x & \text{for } x \leq x_g \\ -\frac{V_g}{x_g}(x_c - x) & \text{for } x \geq x_g \end{cases} \equiv |E_g x_g - E_g x| - E_g x_g, \quad (4.63)$$

considering  $E_g = V_g/x_g$  and  $x_c = 2x_g$ .

The electron velocity is given by

$$\sqrt{\frac{2e}{m_e}(-\Psi(x)) + v_0^2}, \quad (4.64)$$

while the space-charge density is defined by

$$\rho_{sc}(x) = \int \frac{j(v_x)}{v_x(x)} dv_x. \quad (4.65)$$

At the emitter surface, the velocity distribution of the emitted electrons is given by the half-Maxwellian distribution (2.11). In the inter-electrode space, however, the velocity distribution is modified by the electrostatic potential  $\Psi(x)$ . A general expression for  $\rho_{sc}(x)$  is found analogous to the considerations presented in section 4.2, while additionally accounting for the gate-potential  $\Phi_g$ . This leads to

$$\rho_{sc}(x) = 2en_0 \left( \frac{m_e}{2\pi k_B T} \right)^{\frac{1}{2}} e^{-\frac{e\Psi(x)}{k_B T}} \begin{cases} \int_{-v_{x,\min}(x)}^{\infty} dv_x e^{-\frac{v_x^2}{2k_B T}} & \text{for } x < x_{\max} \\ \int_{v_{x,\min}(x)}^{\infty} dv_x e^{-\frac{v_x^2}{2k_B T}} & \text{for } x \geq x_{\max} \end{cases}, \quad (4.66)$$

with the minimum velocity

$$v_{x,\min}(x) := \sqrt{\frac{2e}{m_e}(\Psi_{\max} - \Psi(x))}. \quad (4.67)$$

#### 4 One-Dimensional Current Model

Using the Gaussian integral and the error function (compare page 64), the Poisson equation is obtained as

$$\Delta\Psi(x) = -\frac{en_0}{\epsilon_0} e^{-\frac{e}{k_B T}\Psi(x)} \left\{ 1 \pm \operatorname{erf} \left[ \left( \frac{e}{k_B T} (\Psi_{\max} - \Psi(x)) \right)^{\frac{1}{2}} \right] \right\}. \quad (4.68)$$

The plus and minus signs indicate  $x \leq x_{\max}$  and  $x \geq x_{\max}$ , respectively. The equation can be rewritten to obtain the following self-consistent differential equation for the space-charge potential

$$\Delta\Phi_{\text{sc}}(x) = -\frac{en_0}{\epsilon_0} e^{-\frac{e}{k_B T}(\Phi_{\text{sc}}(x) - E_g x)} \left\{ 1 \pm \operatorname{erf} \left[ \left( \frac{e}{k_B T} (\Psi_{\max} - \Phi_{\text{sc}}(x) + E_g x) \right)^{\frac{1}{2}} \right] \right\}. \quad (4.69)$$

The boundary conditions are defined by the electric potential of emitter and collector

$$\Phi_{\text{sc}}(0) = \Psi(0) = 0 \quad \text{and} \quad \Phi_{\text{sc}}(x_c) = \Psi(x_c) = 0. \quad (4.70)$$

It needs to be considered that  $\Phi_{\text{sc}}(x)$  must be continuously differentiable at  $x = x_g$ .

The electron density just outside the emitter surface  $n_0$  is obtained by calculating the saturation current density, which is equivalent to the Richardson-Dushman equation, leading to

$$n_0 = \frac{J_{\text{RD}}(\phi_e, T_e)}{e} \left( \frac{\pi m_e}{2k_B T} \right)^{\frac{1}{2}}. \quad (4.71)$$

The electron density is a function of the emitter temperature  $T_e$  and the emitter work function  $\phi_e$ .

Taking all this into account, equation (4.69) can be solved numerically. After calculating the space-charge potential  $\Phi_{\text{sc}}(x)$  and the total potential  $\Psi(x)$ , the current density can be determined by

$$J = J_{\text{RD}} e^{-e\Psi_{\max}/k_B T}. \quad (4.72)$$

Using the solution of  $\Phi_{\text{sc}}(x)$ , the space-charge density in the vacuum gap can be determined by equation (4.66). It can be divided into two parts: the contributions from electrons that do not reach the collector and return to the emitter, and the contribution from those that reach the collector.

By virtue of equation (4.66), the space-charge density of the electrons returning to the emitter is given by

$$\rho_{\text{sc},1}(x) = 2en_0 \left( \frac{m_e}{2\pi k_B T} \right)^{\frac{1}{2}} e^{-\frac{e\Psi(x)}{k_B T}} \operatorname{erf} \left[ \left( \frac{e}{k_B T} (\Psi_{\max} - \Phi_{\text{sc}}(x) + E_g x) \right)^{\frac{1}{2}} \right], \quad (4.73)$$

whereas the space-charge density of the electrons reaching the collector is

$$\rho_{sc,2}(x) = 2en_0 \left( \frac{m_e}{2\pi k_B T} \right)^{\frac{1}{2}} e^{-\frac{e\Psi(x)}{k_B T}} \left\{ 1 - \operatorname{erf} \left[ \left( \frac{e}{k_B T} (\Psi_{\max} - \Phi_{sc}(x) + E_g x) \right)^{\frac{1}{2}} \right] \right\}. \quad (4.74)$$

I used these equations to calculate the space-charge potential and the space-charge density, shown in figure 3.2 on page 33, to illustrate the effect of the gate electrode in a thermoelectronic converter.

## Results and Comparison of the Different Models

In this section, I will discuss the results obtained with the ideal-gate model including the electron velocity distribution, and compare them to the results obtained with the previous models to estimate the influence of the initial electron velocity on the current density.

The dependence of the current density on the emitter-collector distance is crucial for our concept. I therefore investigated this dependency for the gate model when including the electron velocity distribution. Figure 4.11 shows  $J$  plotted as a function of  $d_{ec}$  for two different gate voltages  $V_g$ .

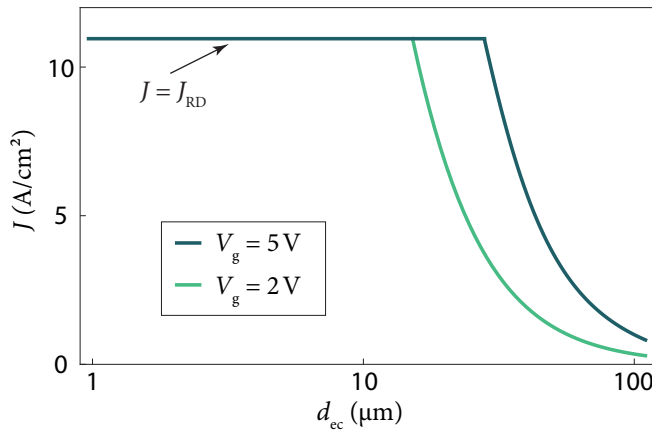


Figure 4.11: Current density  $J$  as a function of the emitter-collector distance for electrons with a thermal velocity distribution for two different gate voltages of 2 V and 5 V.  $J$  increases for decreasing distance until reaching the saturation value, described by the Richardson-Dushman current density  $J_{RD}$ . The following parameters were used:  $T_e = 1500$  K,  $\Phi_e = 2.2$  eV.

The current density increases for decreasing distance, until the saturation value, described by the Richardson-Dushman value, is reached. Within the electrostatic model, the transition into the saturation value is abrupt. This can be understood by considering the following: decreasing the distance leads to a lower space-charge potential, increasing the number of electrons reaching the emitter. As the electrons velocity distribution follows an exponential behavior, the slope of the curve is very steep. The number of electrons increases steadily, until all electrons reach the collector. To avoid this abrupt transition, the system would have to be described dynamically, also including the momentum of the electrons.

For both models including a uniform velocity, the current density scales with  $1/d_{ec}^2$ . To determine the exact dependency of  $J(d_{ec})$  for the thermal distribution model, I determined the slope of the curve  $J(d_{ec})$  before reaching saturation by performing a linear fit in a double logarithmic plot of the results. For different calculations, I obtained exponents

#### 4 One-Dimensional Current Model

in the range of 1.86–1.92. The relation  $J \propto 1/d_{ec}^2$  can thus be considered a good approximation for the ideal-gate model. This is a remarkable result, as it shows the same behavior as the Child-Langmuir Law.

To investigate the influence of the initial electron velocity on the current density, I plotted  $J$  as a function of the gate voltage  $V_g$  for the different models (figure 4.12). To better illustrate the difference between the results, I used a logarithmic scale.

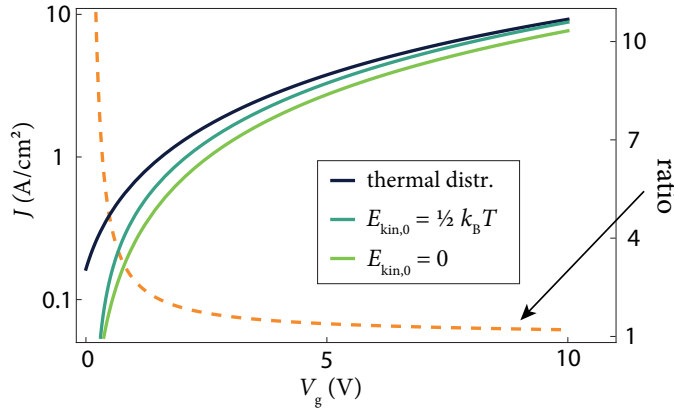


Figure 4.12: Current density  $J$  as a function of the gate voltage  $V_g$  for the three different models: 1) with no initial velocity, 2) a uniform initial velocity and 3) the thermal distribution. The dashed line indicates the ratio for electrons with no initial velocity and electrons following a thermal distribution. The following parameters were used:  $T_e = 1500$  K,  $d_{ec} = 50$   $\mu\text{m}$ ,  $\Phi_e = 2.2$  eV.

As is to be expected, both models with an initial electron velocity yield higher current densities than the model for electrons with no initial velocity. For strong voltages, however, the gate voltage dominates the kinetic energy of the electrons and the results converge.

For small applied voltages, the thermal distribution model yields significantly higher current densities. This is mainly because the current density is not limited to the case that no peak in the inter-electrode potential  $\Psi(x)$  is formed (compare the discussion on page 59). In the thermal distribution model, however, a maximum of  $\Psi(x)$  is possible, enabling higher current densities. Only in this model, the fractions of the electrons reaching the collector and of those turning around due to the space charge, can be calculated. This low-voltage regime can be crucial for thermoelectronic energy converters, if very small distances are considered.

As a last step, I will investigate the temperature dependence of the current density for the different ideal-gate models (figure 4.13). When assuming no initial velocity, the current density does not depend on  $T_e$ .

Different to the models for a uniform electron velocity, which treat the emitter as an infinite electron reservoir, the thermal distribution model accounts for the saturation current density. The saturation current is obtained as part of the solution. In the other models, the saturation limit could only be considered *a posteriori*.

For higher temperatures, when the saturation limit is not reached and the current density is limited by the space charge, the thermal distribution model yields a higher current density than the other two models. The difference increases with increasing temperature. This is because for higher temperatures, more electrons have sufficient energy to overcome the space-charge potential maximum. This effect is not included in the uniform

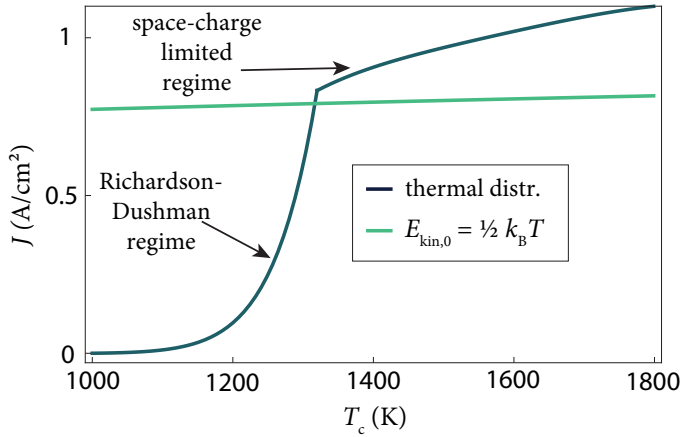


Figure 4.13: Current density  $J$  as a function of the emitter temperature  $T_e$  for the model including the thermal distribution and the model including a uniform initial velocity. In the thermal distribution model, the saturation current density is included in the calculations. The following parameters were used:  $V_g = 5$  V,  $d_{ec} = 50$   $\mu\text{m}$ ,  $\Phi_e = 2.2$  eV.

velocity model. Here, the space charge is only reduced due to a higher electron velocity with increasing temperature, resulting in a slight increase of  $J$ .

Summing up, all three models yield current densities of the same order of magnitude. For strong gate voltages, the predicted values converge. For high temperatures and moderate or low applied voltages, typically below 2 V, however, the influence of thermal distribution of the electrons is significant. Moreover, the saturation limit is also included as a part of the solution.

### Limitations of the Ideal-Gate Model

The one-dimensional, electrostatic approach is a good approximation and represents a first step for modeling the electron behavior in thermoelectronic energy converters. Nonetheless, it has several limitations, which will be discussed briefly below.

#### Static Model

In the electrostatic calculations, based on the concepts introduced by Langmuir [35, 102] and Hatsopoulos [29], the electron transport is treated as a static process. For a full description, the process has to be treated dynamically, also including the momentum of the emitted electrons.

Akimov *et al.* solve the space-charge limited current using Lagrangian flow description based on the Poisson equation, the continuity equation and the momentum equation. They show that the Child-Langmuir Law is correct if either the initial electron velocity is indeed zero, *i.e.*  $v_0 = 0$ , or the applied voltage is very strong, *i.e.*  $V \rightarrow \infty$ . They furthermore argue that the Langmuir Theory does not describe the space-charge limited current in full detail, underestimating the actual current density.

Considering these arguments, the ideal-gate model presented should underestimate the current density for small  $V_g$ . However, for higher  $V_g$ , the model should present a good approximation.

### Expansion to Different Gate Potentials

The total electrostatic potential  $\Psi(x)$  consists of the external contribution from the gate  $\Phi_g(x)$  and the space-charge potential  $\Phi_{sc}(x)$

$$\Psi(x, y, z) = \Phi_g(x, y, z) + \Phi_{sc}(x, y, z).$$

The Poisson equation is given by

$$\left( \frac{\partial^2}{\partial x^2} + \frac{\partial^2}{\partial y^2} + \frac{\partial^2}{\partial z^2} \right) \Phi_g(x, y, z) + \left( \frac{\partial^2}{\partial x^2} + \frac{\partial^2}{\partial y^2} + \frac{\partial^2}{\partial z^2} \right) \Phi_{sc}(x) = -\frac{\rho_{sc}(x, y, z)}{\epsilon_0}. \quad (4.75)$$

If no charges are present, only the contribution of the gate potential remains. Therefore

$$\left( \frac{\partial^2}{\partial x^2} + \frac{\partial^2}{\partial y^2} + \frac{\partial^2}{\partial z^2} \right) \Phi_g(x, y, z) = 0. \quad (4.76)$$

As this equation has to be valid at all times, (4.75) is reduced to

$$\left( \frac{\partial^2}{\partial x^2} + \frac{\partial^2}{\partial y^2} + \frac{\partial^2}{\partial z^2} \right) \Phi_{sc}(x) = -\frac{\rho_{sc}(x, y, z)}{\epsilon_0}.$$

If  $\rho_{sc}$  is uniform in two dimensions, this equation can be reduced to a one-dimensional form, equivalent to the form used in the ideal-gate model

$$\frac{d^2 \Phi_{sc}(x)}{dx^2} = -\frac{\rho_{sc}(x)}{\epsilon_0}.$$

However, if the gate potential has a finite curvature in x-direction, the components in y- and z-direction do not vanish as well, as can be seen from equation (4.76)

$$\frac{\partial^2 \Phi_g}{\partial x^2} \neq 0 \quad \longrightarrow \quad \frac{\partial^2 \Phi_g}{\partial y^2} + \frac{\partial^2 \Phi_g}{\partial z^2} \neq 0.$$

Such a gate potential induces a three-dimensional space-charge density. This means that a one-dimensional gate potential with a finite curvature, *e.g.*, a parabolic potential, cannot be treated in the one-dimensional approach.

### Including the Collector Back Emission

The ideal-gate model could be expanded to include the back emission from the collector, analogous to approaches to extend the Langmuir Theory in references [29, 33, 71]. For efficient thermoelectronic converters, however, the back emission has to be kept small. Including its contribution should therefore not lead to a significant modification of the results.

## 4.4 Current-Tube Model - Connection to Experimental Set-Up

The ideal-gate model assumes a perfectly homogenous electric field. Below I will present a model that is based on the ideal-gate model, but accounts for inhomogeneities in the electric field induced by the three-dimensional structure of the gate electrode. This is especially important for small distances, *i.e.*  $d_{ec} \lesssim w$ .

I worked on this approach in collaboration with Stefan Meir. He calculated the electric fields and the results of the current-tube model based on my current density calculations. His discussion of the current tube model can be found in [3].

The inter-electrode space is divided into separate tubes, each extending from the emitter to the collector surface. To guarantee that no uncovered volumes are created, these tubes need to have a triangular base area. The electric field in each tube is calculated using the electric field solver from the IES software package [99]. Determining the average value of the electric field enables us to assign a current density to each tube separately by using the ideal-gate model (as the electric field in the ideal-gate model is constant, the average value is used). The total current density is obtained by summing up the contributions of all tubes.

We consider only the current in the gate meshes. The tubes extending through the gate bars do not contribute to the collector current, and are therefore neglected. The current density in these tubes, however, can be modeled using the Child-Langmuir Law.

Figure 4.14 shows a schematic diagram of the tube model for a cross section of the setup. The colors in the tubes indicate the electric field strength.

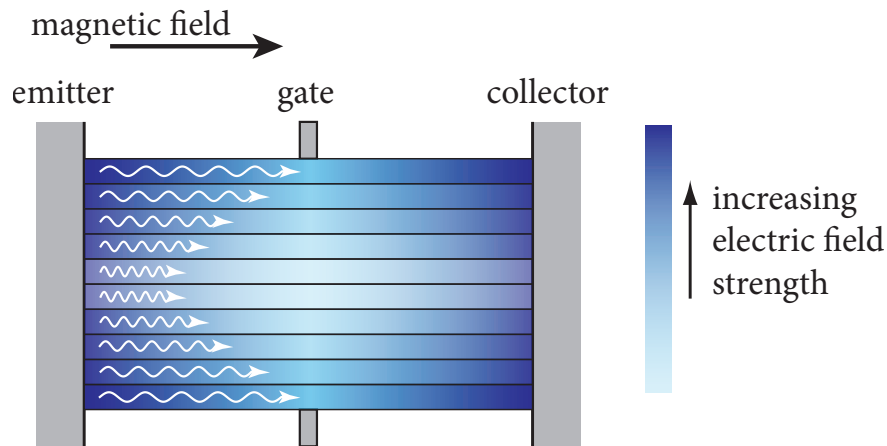


Figure 4.14: Visualization of the current-tube model for a cross section of the setup. The inter-electrode space is divided into separate tubes. For each tube, the electric field is calculated and the current density is determined using the ideal-gate model. The field strength of the electric field is indicated by the color inside the tubes. The electric field in the tubes close to the gate is stronger than in those in the center of the gate meshes. For  $d_{ec} < w$ , this inhomogeneity becomes strong. The electron paths and their velocity is indicated by white lines. Image drawn following [3].

Figure 4.15 displays an example for the calculated electric field component  $E_{\parallel}$  and the average values for two different tubes. The component  $E_{\parallel}$  is responsible for accelerating the electrons away from the emitter and reducing the space charge (compare chapter 3.2).

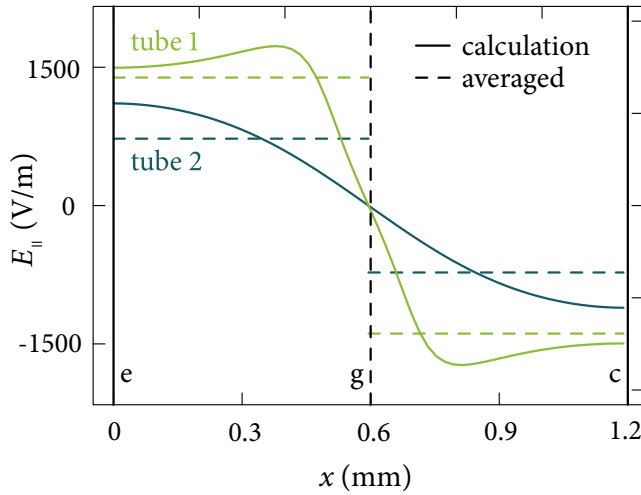


Figure 4.15: Calculated electric field (continuous lines) and average field values (dashed lines) for two different tubes within the current tube model. Tube 1 is closer to the grid bars. For this reason, the electric field is stronger than for tube 2. The letters e, c and g indicate emitter, collector and gate, respectively. The following parameters were used:  $V_g = 1 \text{ V}$ ,  $d_{ec} = 1 \text{ mm}$ ,  $w = 1.6 \text{ mm}$ . Only the parallel electric field component  $E_{\parallel}$  is considered. Data calculated Stefan Meir [3], using the electric field solver ‘Coulomb’ [99].

For a gate with  $w \rightarrow 0$ , the current-tube model is equivalent to the ideal-gate model.

### Application and Limitations of the Current Tube Model

The current tube model accounts for inhomogeneities in the gate electric field. However, the model cannot account for the three-dimensional distribution of the space-charge density. These two phenomena are interconnected. An inhomogeneous electric field induces an inhomogeneous space-charge distribution.

The effect of a varying space-charge density can be compared to a ‘cross talk’ between the tubes. I will illustrate this using the example of two adjacent tubes. Tube 1 contains a higher current and therefore a higher space-charge density than tube 2. The electrons in tube 2 ‘see’ the higher space-charge density in tube 1. Therefore, the current in tube 2 is further reduced. On the other hand, electrons in tube 1 experience a lesser space-charge density from tube 2, leading to a higher current in tube 1. As a consequence, tubes with ‘stronger’ tubes next to them yield smaller current densities than calculated, while tubes with ‘weaker’ tubes next to them yield higher current densities than calculated.

A similar effect sets in for strong gate currents. The current densities in the tubes extending through the grid bars are generally higher than in all other tubes for two reasons: 1) the electric field at the emitter surface facing the gate bars is stronger than in the areas in facing the gate meshes; 2) even for the same electric fields, the current densities in the gate tubes is greater than in the other tubes (the Child-Langmuir Law yields a higher current than the ideal-gate model). As a consequence, when the gate current becomes strong, the tubes extending through the gate bars lead to a reduction of the current in the other tubes, analogous to the case discussed above.

Considering these arguments, I expect the results from the current-tube model to deviate from the experimental results in the following cases:

- For small distances, *i.e.*  $d_{ec} \lesssim w$ , the electric field generated by the gate becomes inhomogeneous, leading to varying current densities in the tubes. Furthermore, the electric field in the emitter areas surface facing the gate bars will be very high, leading to strong gate currents. As discussed, both these effects can lead to errors in the results of the current tube model.
- For high applied voltages, the current densities in the tubes extending through the gate bars become strong and reduce the currents in the other tubes. Further increasing the voltage will therefore only lead to a small increase in the collector current, despite the increasing electric field.
- For very small emitter-gate distances, *i.e.*  $d_{ec} \ll w$ , the electric field in the gate meshes starts to decrease for decreasing distance and the electric field becomes completely inhomogeneous (compare to chapter 3.4). The current in the gate meshes therefore decreases as well and approaches the case for converters without a gate electrode. This case cannot be described by the current-tube model, however, due to the strong inhomogeneities of the electric field.

To calculate the current density using the current-tube model, the ideal-gate model has to be solved for many different values of the electric field. When including the thermal distribution, this leads to a very high computational effort, as the solution can only be found by complex numerical calculations. We therefore used the analytical solution (4.59), which represents a good approximation and yields a lower limit for the achievable currents.

## 4.5 Main Conclusions of the One-Dimensional Model Calculations

The ideal-gate and the current-tube model derived in this chapter are not an exact description of the three-dimensional space-charge limited electron motion. They do, however, allow us to estimate the current density in the system, depending on different setup parameters, and provide an insight into the formation of the space-charge potential. They are based on established space-charge theories that agree closely with experimental results.

Below I will briefly summarize the main conclusions of the one-dimensional model calculations presented.

- The optimal geometrical configuration is a symmetrical setup with the gate being mounted directly in the middle between emitter and collector, *i.e.*  $x_g = d_{ec}/2$ .
- The current density  $J$  scales, in a good approximation, with  $1/d_{ec}^2$ . Remarkably, this is the same dependency as described by the Child-Langmuir Law, which describes

the electron current between two plane-parallel metal plates, if an accelerating voltage is applied to the collector.

- The analytical solution, obtained when neglecting the thermal electron velocity, represents a good approximation for the current density and yields a lower limit for the current in a given setup. It is given by

$$J = \frac{\varepsilon_0}{\sqrt{6}} \left( \frac{e}{m_e} \right)^{\frac{1}{2}} \frac{V_g^{\frac{3}{2}}}{x_g^2}. \quad (4.77)$$

This result, however, is not valid for  $V_g \rightarrow 0$ .

- For strong applied gate voltages  $V_g$ , the thermal energy of the emitted electrons has no significant influence on the current density and can be neglected. For small values of  $V_g$ , however, the thermal energy yields a significant contribution to the current density.
- The electric field required to reduce the space charge so that all emitted electrons reach the collector can be calculated using

$$E_g = \left( \frac{J}{\varepsilon_0} \right)^{\frac{2}{3}} \left( \frac{6m_e}{e} \right)^{\frac{1}{3}} x_g^{\frac{1}{3}}. \quad (4.78)$$

This electric field decreases for decreasing distances. This means that for decreasing distances, lower voltages are needed to suppress the space charge.

- All models considered consistently show that a current density of several  $\text{A}/\text{cm}^2$  can be achieved for distances in the range of  $50 \mu\text{m}$ – $100 \mu\text{m}$ , requiring gate voltages of typically  $2 \text{ V}$ – $10 \text{ V}$ .
- All model calculations are based on an electrostatic approach. A full description would have to treat the system dynamically, also including the momentum of the electrons. Nonetheless, the electrostatic models yield a good approximation. Only for small voltages, the models slightly underestimate the actual current density.
- Although the ideal-gate model is only valid for perfectly homogenous fields, it can be used within the current-tube model to account for inhomogeneities induced by the three-dimensional gate electrode. For strong applied voltages or small distances, *i.e.*  $d_{\text{ec}} < w$ , however, I expect the calculated values to deviate from the experimental results. For  $w \rightarrow 0$ , the current-tube model is equivalent to the ideal-gate model.

In the following chapter, I will apply the ideal-gate model and the current-tube model to our experimental data. It will become evident that the considerations in this chapter characterize our investigated system well.

# 5 Experimental Investigation of the Concept

To explore the concept of thermoelectronic converters experimentally, we constructed a mechanical setup mounted in a vacuum chamber. Practical applications, as discussed in the next chapter, require devices with electrode distances of several ten micrometer, built with microelectronic technology. However, our adjustable setup allowed us to investigate different geometrical configurations.

Our experimental setup, measurement techniques and data analysis are presented in detail by Stefan Meir in [3]. Below is a brief overview of the different experimental stages, the measurement setup and the obtained results. I will compare the experimental data with the results of the model calculations discussed in the previous chapter.

## 5.1 Overview of the Experimental Setup and Development Stages

Our experimental setup went through several stages of development. We began with a very simple arrangement using a tungsten coil as emitter, a steel plate as collector, a gate formed of tungsten wires mounted on a copper frame and four small permanent magnets attached to a magnetic steel yoke to channel the electrons through the gate meshes. Figure 5.1 shows a photograph of this setup. We developed the setup further, as illustrated in figures 5.2 and 5.3, to arrive at the stage shown in figure 5.4. One constant throughout this development was the vacuum chamber, shown in figure 5.5, in which the electrode arrangement was mounted on a ceramic plate. All measurements were performed at a base pressure of  $1 \times 10^{-7}$  mbar. Electric measurements were performed using Keithley source-measurement units in 4-wire sensing. The early experiments did not yield the desired high current densities. In hindsight it is easy to see why.

For practical reasons, we did not optimize the setup for high efficiencies. For example, we did not install heat shields between the electrodes or optimize the electrical connection for a low heat transfer.

The results shown below have been obtained with the setup displayed in figure 5.4. The barium-oxide (BaO) dispenser cathode has a work function in the range of 2 eV–2.5 eV [3]. For studying the electron behavior and the current densities, the collector does not need to have a lower work function than the emitter, as in practical converters. Any work function configuration can be simulated by applying a voltage to the collector, shifting its electrostatic potential (compare chapter 2.5). We therefore used a steel collector for most

## 5 Experimental Investigation of the Concept

measurements to simplify the setup. To analyze the data and different converter configurations, we determined the work functions of emitter and collector from the measured IV-characteristics [3]. We observed a shift of the work function of the steel collector during the measurements. This shift was supposedly caused by barium vapor, evaporated from the BaO-dispenser cathode, that condensed on the collector surface, thereby lowering the work function. To validate our results, we additionally set up an arrangement of two BaO-dispenser cathodes, which enabled us to determine the work functions during the measurements.

The magnetic field was generated using two stacks of  $\text{Nd}_2\text{Fe}_{14}\text{B}$  permanent magnets [105] that we attached to a steel yoke to channel the field and guarantee a homogeneous field distribution in the measurement area. The magnetic yoke was mounted on a rotary feed-through, enabling us to rotate the magnets out of the measurement area, thus ‘switching’ the magnetic field on and off *in situ*.

To investigate the influence of the gate geometry, we performed measurements with two different gates, shown in figure 5.6. Both gates have been produced by laser-cutting tungsten foils. I will indicate the gate parameters, the mesh width  $w$ , the thickness  $d$  and the grid bar diameter  $b$ , using  $(w \times d \times b)$ .

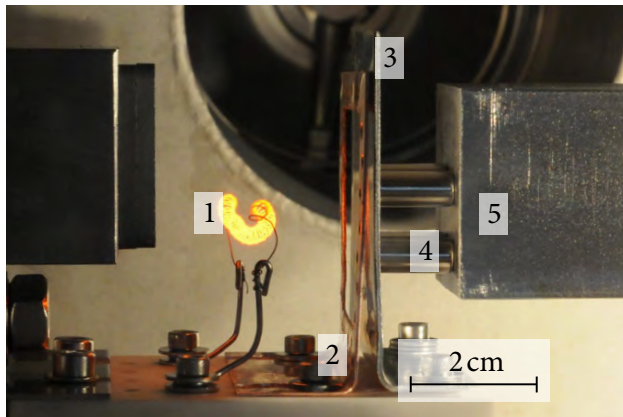


Figure 5.1: The first experimental approach. A resistively heated tungsten coil (1) is used as emitter, a steel plate as collector (3). The gate (2) is a grid formed of tungsten wires, mounted on a copper frame. Four permanent magnets (4) are attached to a steel yoke (5), matching the gate meshes, to channel the electrons through the grid holes. Powers below  $1 \mu\text{W}$  could be measured on the collector. Photograph by Klaus Wiedenmann.

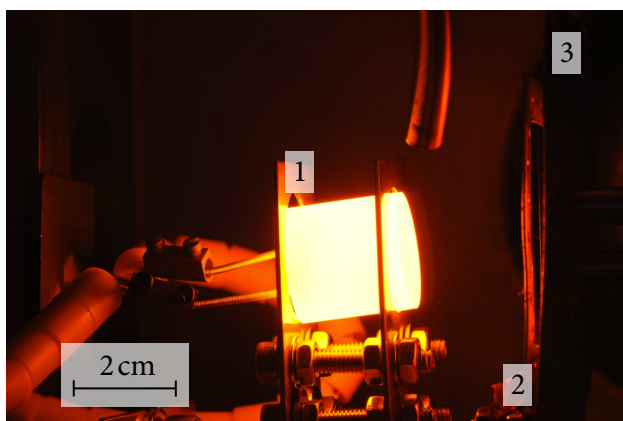


Figure 5.2: To obtain higher current densities, we replaced the tungsten coil by a resistively heated BaO-dispenser cathode (1), produced by the company Heat Wave Labs [106], while the gate (2) and the collector (3) stayed the same. With this setup, we achieved collector powers of about  $10 \mu\text{W}$ . Photograph by Alexander Herrnberger.

## 5.1 Overview of the Experimental Setup and Development Stages

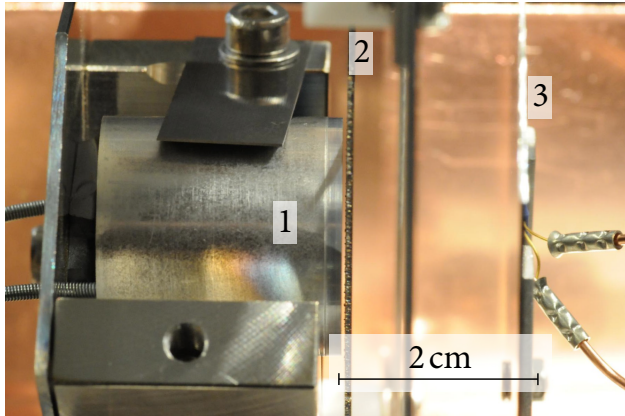
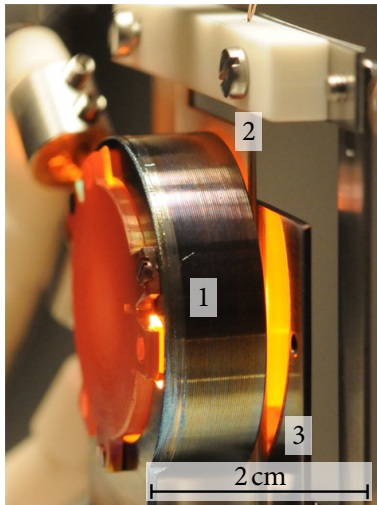


Figure 5.3: As a next step, we improved the cathode holder and used a gate laser-cut from a 200  $\mu\text{m}$  thick tungsten foil (compare figure 5.6). The gate was mounted just in front the emitter. Output powers of order 1 mW were obtained. One reason for the low output power in this setup is the arrangement of emitter (1), gate (2) and collector (3). The gate is mounted close to the emitter, but far from the collector. As discussed in the previous chapter, a non-symmetrical setup creates a strong space-charge potential, severely limiting the current density. Photograph by Klaus Wiedenmann.

(a)



(b)

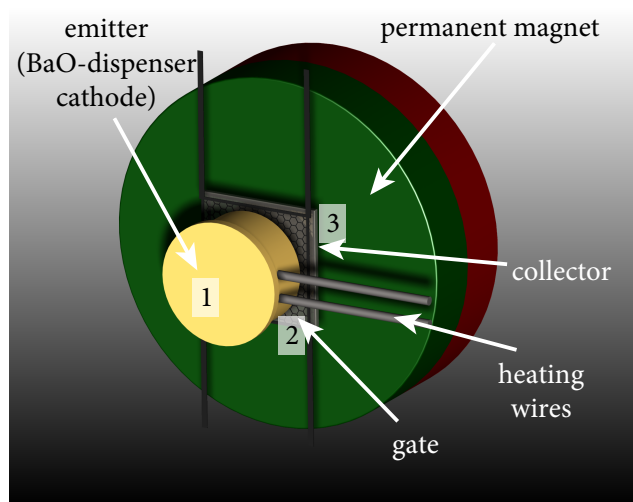


Figure 5.4: Panel (a) shows a photograph of the latest setup. The emitter is a custom designed BaO-dispenser cathode, encapsulated in a heat shield arrangement (1). The gate (2) is barely visible in the picture, as is it closely embedded by emitter and collector (3), all separated by aluminum-oxide spacers. Photograph by Alexander Herrnberger. Panel (b) shows a CAD-sketch of the setup to illustrate the different components. Drawing by Stefan Meir.

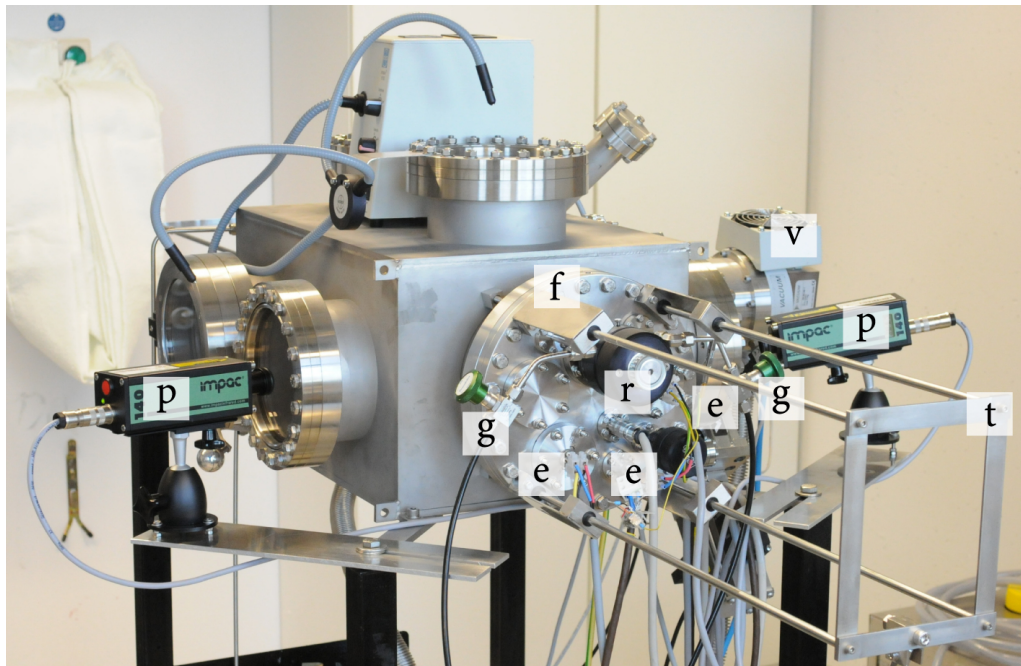


Figure 5.5: Photograph of the vacuum chamber, highlighting important components. The electrode arrangement was mounted on a ceramic plate attached to a flange (f) on the transfer system (t). Further shown are electrical feedthroughs (e), a gas inlet (g), two pyrometers (p), the rotary feedthrough for the magnetic yoke (r) and a turbo pump (v). Photograph by Klaus Wiedenmann.

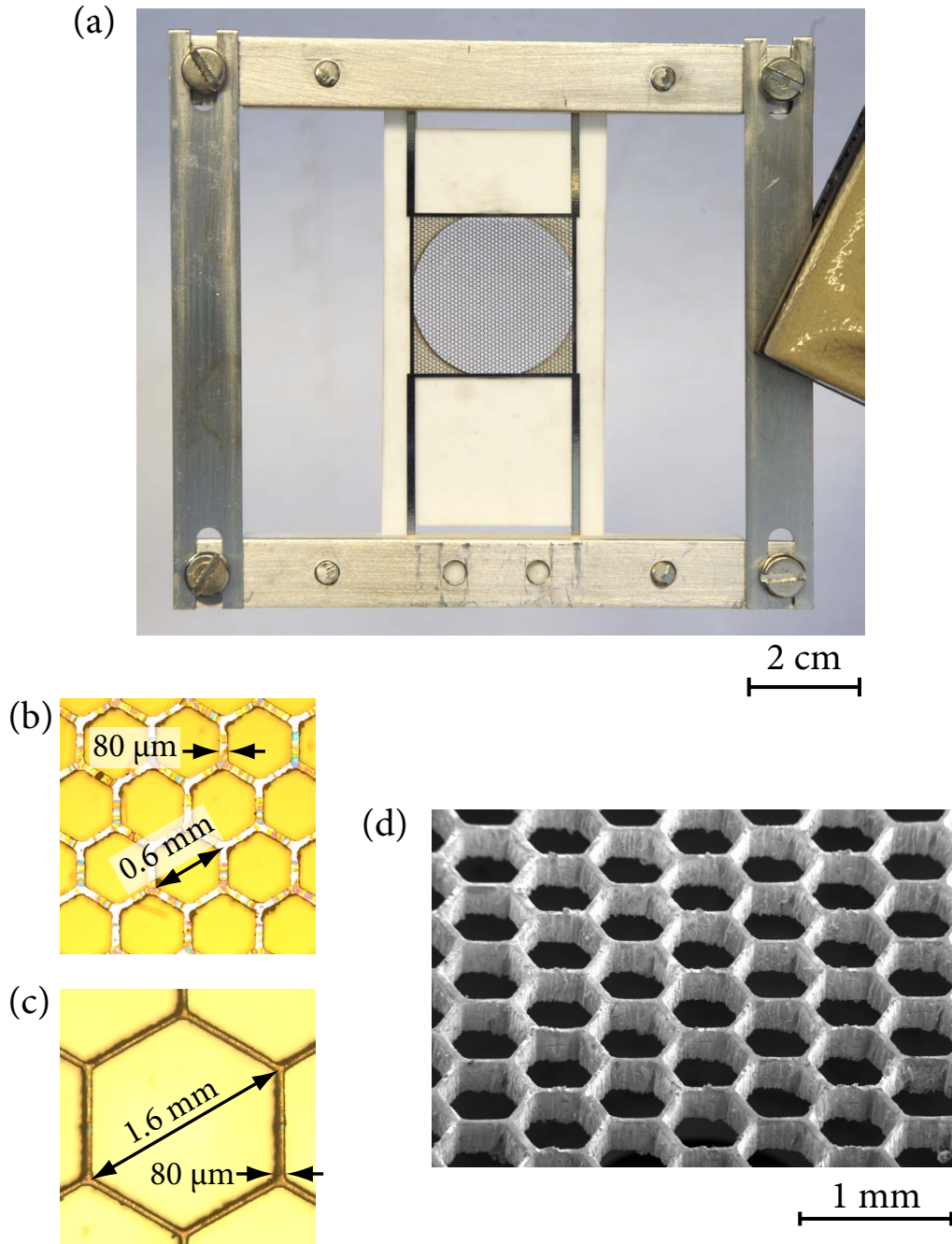


Figure 5.6: (a) Laser-cut tungsten gate mounted in a metal frame. The white plate behind the gate is an aluminum-oxide spacer [107], used to insulate the gate from the collector. Photograph by Stefan Meir. (b), (c) Microscopic images of the two gates used for the measurements, with the parameters  $(1.6 \text{ mm} \times 0.08 \text{ mm} \times 0.2 \text{ mm})$  and  $(0.6 \text{ mm} \times 0.08 \text{ mm} \times 0.2 \text{ mm})$ , respectively. The gates have a geometrical transparency of  $t = 0.98$  and  $t = 0.72$ . Both gates have been structured by laser cutting a  $0.2 \text{ mm}$ -thin tungsten foil. Photographs by Stefan Meir [3]. (d) Scanning electron microscope (SEM) picture of a gate with  $(0.6 \text{ mm} \times 0.08 \text{ mm} \times 0.2 \text{ mm})$ . Picture by B. Fenk, Max-Planck-Institute, Stuttgart.

## 5.2 Main Experimental Results

Figures 5.7–5.10 show a representative extract of the most important measurement data. As we used a steel collector for the measurements, the collector work function is higher than the emitter work function, leading to small output powers. The results demonstrate the effect of the magnetic field and illustrate the influence of the applied gate voltage on the measurements. All data were taken by Stefan Meir [3].

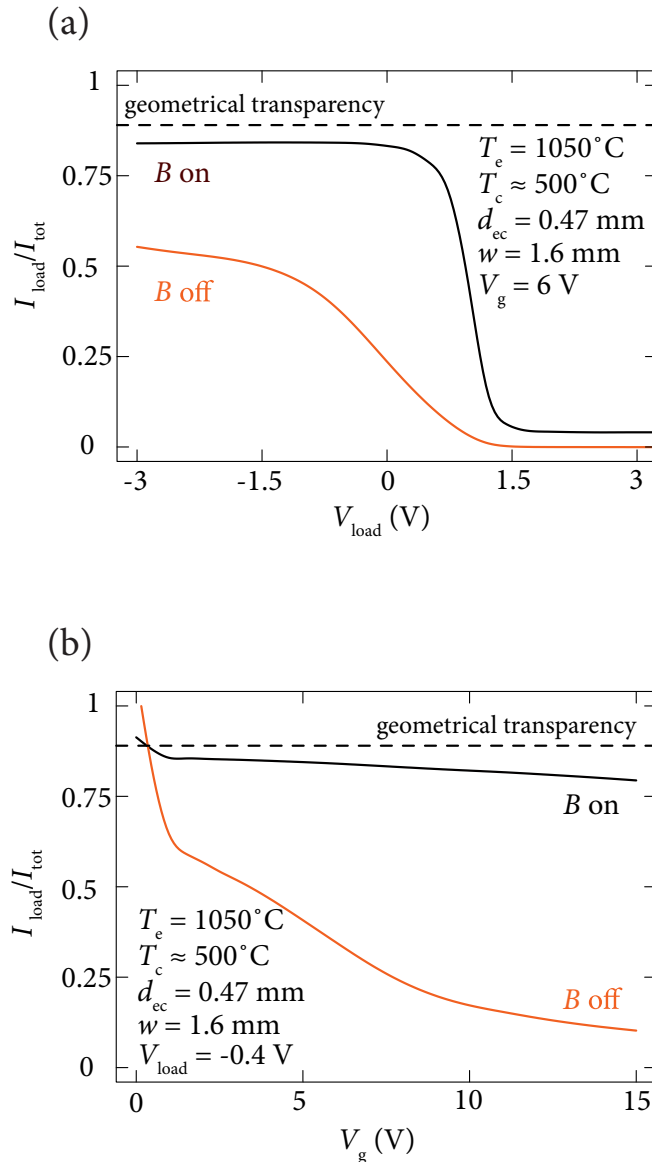


Figure 5.7:

(a) Ratio of the measured load current  $I_{\text{load}}$  to the total current  $I_{\text{tot}}$  as a function of the load voltage  $V_{\text{load}}$  with and without a magnetic guiding field  $B$ . When  $B$  is ‘switched on’, the ratio is close to the geometrical transparency  $t \approx 0.89$  of the gate (see chapter 3.1). For  $V_{\text{load}} \gtrsim 1.5\text{ V}$  the ratio approaches zero as only few electrons reach the collector. When the  $B$ -field is ‘switched off’, the ratio is significantly smaller. (b) Ratio of the measured load current  $I_{\text{load}}$  to the total current  $I_{\text{tot}}$  as function of the gate voltage  $V_g$  with and without a magnetic guiding field. When  $B$  is ‘switched on’, the ratio is close to  $t$  for the entire measurement range, whereas it quickly drops off when  $B$  is ‘switched off’.  $V_{\text{load}}$  was chosen so that emitter and collector are on the same electrostatic potential.

The steel collector was used for these measurements.

These results clearly demonstrate the channeling effect of the magnetic field.

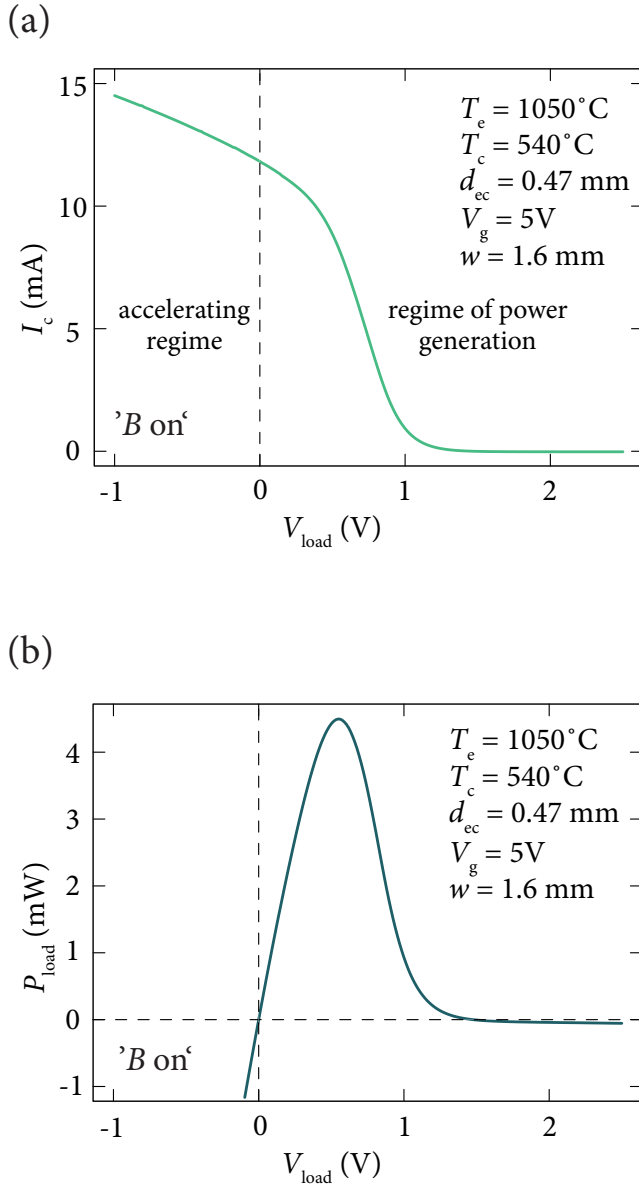


Figure 5.8: (a) Measured load current  $I_{\text{load}}$  and (b) measured load power  $P_{\text{load}}$  as functions of the load voltage  $V_{\text{load}}$ . The measurements can be divided into an accelerating regime and a regime of power generation. For negative  $V_{\text{load}}$ , electrons are accelerated towards the collector, increasing the collector current in a power consuming process. For positive  $V_{\text{load}}$ , power is generated on the collector. A magnetic guiding field was applied in longitudinal direction. A second BaO-dispenser cathode was used as collector for these measurements.

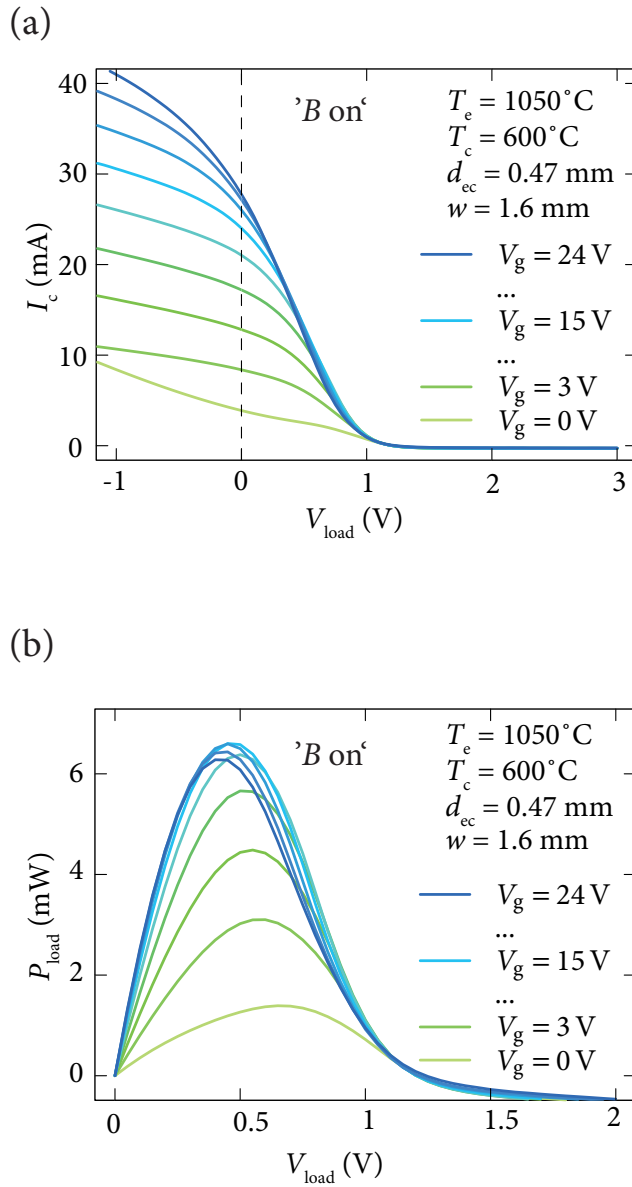


Figure 5.9: (a) Measured load current  $I_c$  and (b) measured load power  $P_{load}$  as functions of the load voltage  $V_{load}$  for a series of gate voltages  $V_g$ , ranging from 0 V–24 V. The applied gate voltage increases both  $I_{load}$  and the maximum generated power, while the value of  $V_{load}$  for the maximum power is shifted. A second BaO-dispenser cathode was used as collector for these measurements.

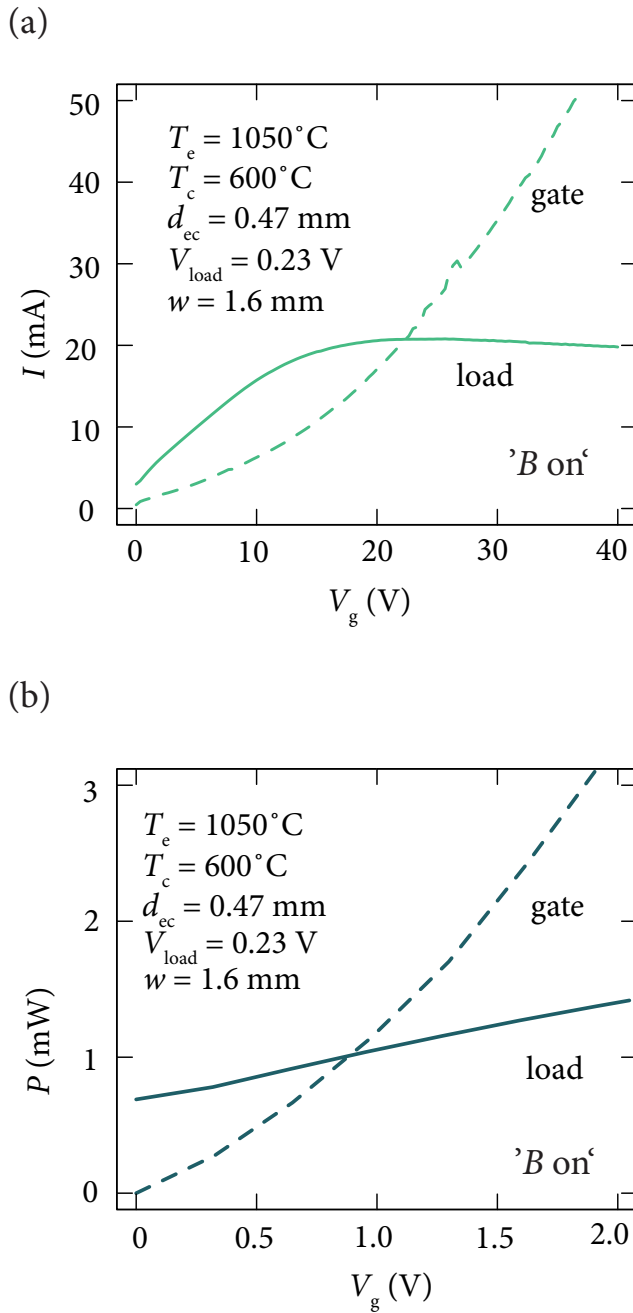


Figure 5.10:

(a) Measured currents on the load and the gate as functions of the gate voltage  $V_g$ . The gate current is greater than the load current only for high voltages.

(b) Measured power on the load and the gate as functions of the gate voltage  $V_g$ . Due to the small generated power on the collector,  $P_g$  dominates  $P_{load}$  already for small gate voltages.

For both graphs,  $V_{load}$  was chosen so that emitter and collector are on the same electrostatic potential and a magnetic guiding field was applied in longitudinal direction. A second BaO-dispenser cathode was used as collector for these measurements.

### 5.3 Comparison of Experimental Results and Model Calculations

Below I will compare the measured current densities to the values calculated according to the models presented in the previous chapter. All calculations consider emitter and collector to be on the same electrostatic potential, which corresponds to the optimal converter configuration.

The experimental measurements have been performed with two gates with mesh diameters  $w$  of 1.6 mm and 0.6 mm, respectively. This allows us to study the influence of the gate geometry on the current density.

Figure 5.11 displays the measured and the calculated current densities as functions of the load voltage. For the measured data, only the current density in the gate meshes is considered; the gate current is not included here. Therefore, the gate transparency does not influence the results, which enables us to compare the results obtained for different gate geometries.

Overall, the calculated values agree well with the measured data. There is a small difference in the qualitative behavior between the datasets, as the calculated values underestimate the experimental data for small  $V_g$  and overestimate them for high  $V_g$ . However, as discussed in chapter 4.4, this behavior is expected: the electrostatic treatment, neglecting the momentum of the electrons, underestimates the current density for small  $V_g$  and for a strong space-charge potential; for high  $V_g$ , the space-charge density becomes inhomogeneous, as the current near the gate increases to large values, reducing the current in the gate meshes.

However, for moderate values of  $V_g$ , the model calculations predict current densities very close to the measured data. This is the case for all measurement configurations. For practical converters, this voltage regime is crucial, because high voltages lead to a high gate energy loss and low voltages cannot suppress the space charge.

Figure 5.12 shows the gate current  $I_g$  as a function of  $V_g$ . The gate current can be modeled by the Child-Langmuir Law (4.13). The emitter-gate distance  $d_{eg}$  obtained by fitting the formula to the measurement data exceeds the actual value of the experimental setup. One reason could be the inhomogeneity of the electric field. Nonetheless,  $I_g$  clearly follows the  $V_g^{3/2}$  behavior predicted by the Child-Langmuir Law.

Figure 5.13 shows the measured and calculated current densities as functions of the emitter-collector distance  $d_{ec}$  for the two gates, both with an applied gate voltage of 6 V. For  $d_{ec} > w$ , the electric fields of the gates are virtually homogeneous and can be modeled by an ideal gate.

For  $d_{ec} < w$ , the fields of the gates become inhomogeneous. This effect is taken into account by the current-tube model. The results of the current-tube model therefore start to diverge from the ideal-gate behavior, as displayed in figure 5.13. For the gate with  $w = 0.6$  mm, the divergence sets in for smaller  $d_{ec}$ . However, the current-tube model does not account for the three-dimensional distribution of the space-charge density, leading to deviations of the measured and calculated results at small distances.

### 5.3 Comparison of Experimental Results and Model Calculations

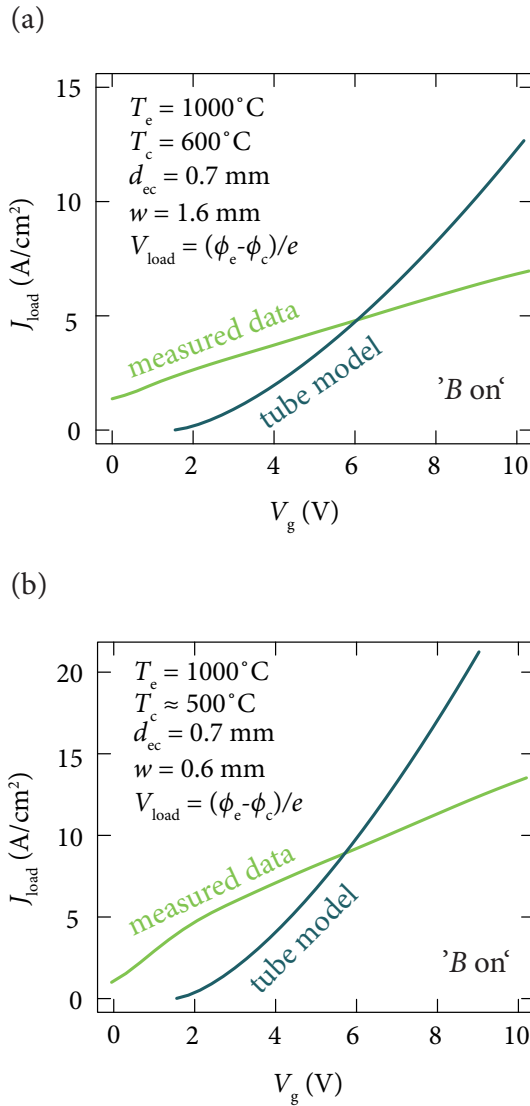


Figure 5.11: Measured and calculated current densities  $J_{\text{load}}$  as functions of the applied gate voltage  $V_g$  for two gate electrodes with different mesh diameters. Here, only the current density in the gate meshes is considered. The load voltage has been chosen so that emitter and collector are on the same electrostatic potential, accounting for their different work functions. The work function of the gate has to be considered, too. The tungsten gate has a work function of about 1.5 eV higher than the emitter [3]. Therefore, the effective voltage is lower by 1.5 V, leading to a decelerating electric field at  $V_g = 0\text{ V}$ . To take this effect in the model calculations into account, the voltage used in the current-tube model has to be adjusted by 1.5 V. The origin of the tube-model graph is therefore shifted by this value in positive direction with respect to the measured values. The steel collector was used for the measurement shown in panel (a), a second BaO-dispenser cathode as collector for the measurements in panel (b).

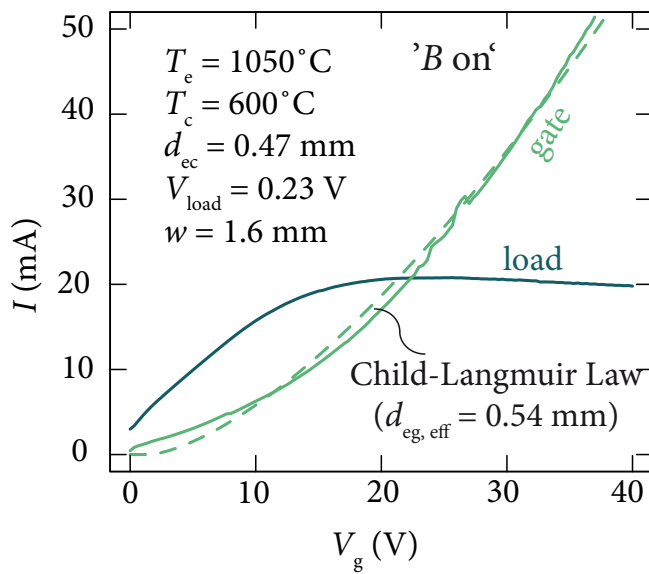


Figure 5.12: Measured and calculated gate and load currents as functions of the applied gate voltage  $V_g$ . The gate current clearly follows the  $V_g^{3/2}$  behavior predicted by the Child-Langmuir Law (4.13). Accounting for the work function of the gate electrode, the voltage for the theoretical calculations has to be adjusted by 1.5 eV. The origin of the modeled graph is therefore shifted by this value in positive direction with respect to the measured values. A second BaO-dispenser cathode was used as collector for these measurements.

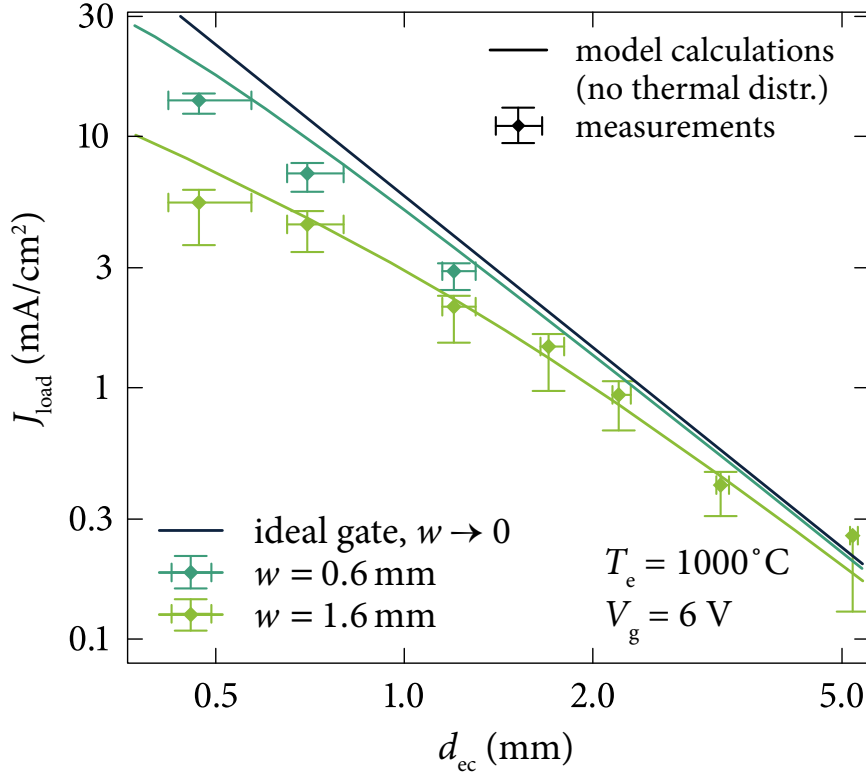


Figure 5.13: Measured and calculated current densities  $J_{\text{load}}$  as functions of the emitter-collector distance  $d_{\text{ec}}$ . Only the current density in the gate meshes is considered here. Therefore, the transparencies of the gate electrodes do not influence the results. The calculated values of the ideal-gate model and the current-tube model diverge for  $d_{\text{ec}} < w$ . The current tube model accounts to for the inhomogeneities of the gate electric fields. However, it does not account for the three-dimensional distribution of the space-charge density, leading to deviations between the calculated and the measured values for small distances. For each measurement, the load voltage has been chosen so that emitter and collector are on the same electrostatic potential. To account for the work function of the gate, the voltage used in the model calculations was adjusted by 1.5 V.

### Radius of Gyration

The radius of gyration  $r_{\text{gyr}}$  of the electrons can be calculated using equation (3.22) derived in chapter 3.2

$$r_{\text{gyr}} = \frac{(v_{x0}^2 + (v_{y0} + E_{\perp}/B)^2)^{\frac{1}{2}}}{\omega_B}, \quad (5.1)$$

where  $B$  indicates the magnetic field strength,  $E_{\perp}$  the electric field component perpendicular to  $\mathbf{B}$ , and  $\omega_B = eB/m_e$  the gyrofrequency.

For the initial electron velocities  $v_{x0}$  and  $v_{y0}$ , their thermal mean values can be used (compare chapter 2.4), given by

$$v_{x0}^2 = \frac{k_B T}{m_e} \quad \text{and} \quad v_{y0} = \sqrt{\frac{k_B T}{\pi m_e}}, \quad (5.2)$$

considering that the mean value of the velocity and the quadratic mean are not equivalent.

To estimate  $B$ , I calculated the magnetic field for a model of our experimental setup, using the IES software package [99]. Figures 5.14 illustrates the results of the field calculations, showing that the magnetic field is in the range of 0.1 T–0.5 T.

An upper limit for  $r_{\text{gyr}}$  can be determined if the maximum value of  $E_{\perp}$  along each electron path is used. I therefore also calculated the electric field in the model system and determined the perpendicular components at the point where the electron trajectories cross the center of the gate, yielding the maximum value of  $E_{\perp}$  for each trajectory.

Figure 5.15 shows  $E_{\perp}$  along two lines (indicated in red) in the center of a gate mesh, for a gate with  $w = 1.6$  mm and  $V_g = 5$  V. The radius of gyration, resulting from these electric fields, is also shown, calculated for a magnetic field strength of 0.1 T. If  $r_{\text{gyr}}$  exceeds the distance to the nearest gate bar, electrons crossing the gate at this position potentially hit the gate through their helical motion. This region is highlighted in red. The results demonstrate that the fraction of the electrons hitting the gate due to their helical motion is negligible in our setup.

### 5.3 Comparison of Experimental Results and Model Calculations

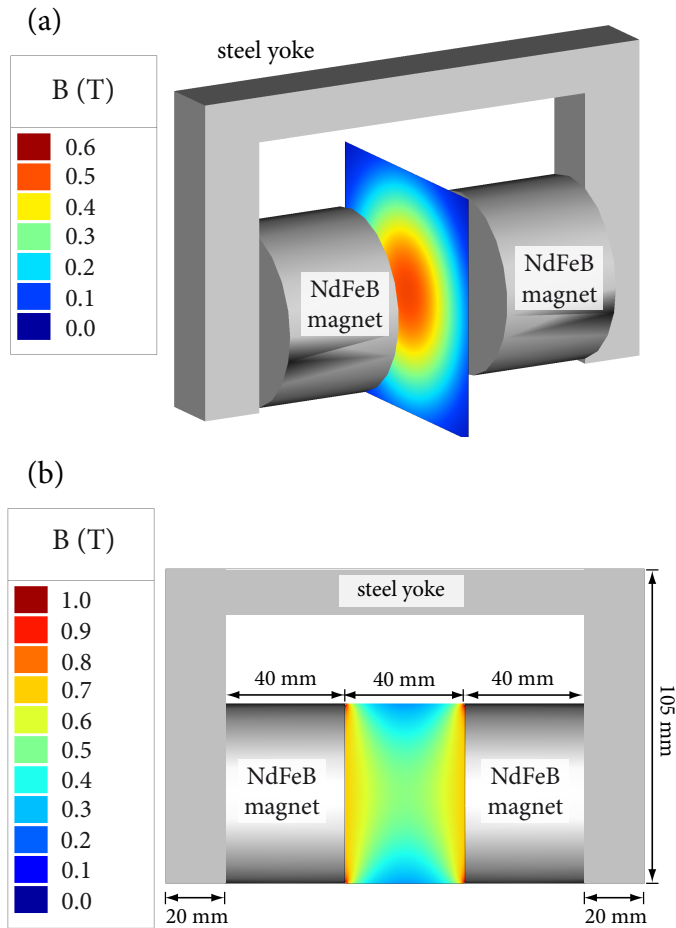


Figure 5.14: Screenshots showing the calculated magnetic field, using the magnetic field solver ‘Amperes’ [99], for the setup geometry used in the experimental measurements. In the experimental setup, the electrodes are mounted between the two Nd-FeB magnets. Panel (a) shows the magnetic field  $B$  between emitter and collector for a cross section parallel to the electrode surfaces, whereas panel (b) shows the magnetic field between the two magnets from a side view perspective. The magnetic field reaches its highest values of about 1 T near the surfaces of the magnets. The field distribution in the measurement area — the green-yellow area in panel (b) — is very homogeneous and assumes flux density of about 0.5 T.

The dimensions, indicated in panel (b), are the same in both sketches. In the calculations, the steel yoke has a relative permeability of  $\mu/\mu_0 = 1000$ , the NdFeB magnets have a remanence of  $B_r = 1.3$  T and a coercive field of  $H_c = -987 \times 10^3$  A/m.

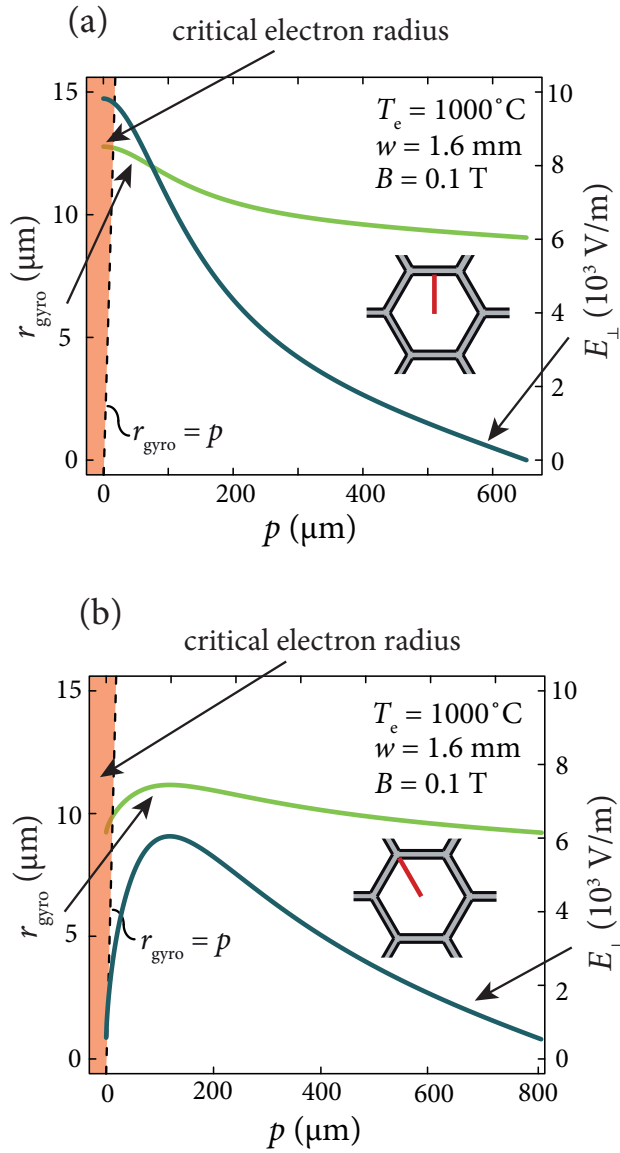


Figure 5.15: Electric field component perpendicular to the electron trajectories  $E_{\perp}$  along two different lines (indicated in red) in a gate mesh for  $V_g = 5\text{ V}$  and resulting radius of gyration  $r_{\text{gyr}}$ . The values of  $E_{\perp}$  shown correspond to the points where the electron trajectories cross the center plane of the gate, representing the maximum values for each electron path.  $p$  indicates the distance from the nearest grid bar. If  $r_{\text{gyr}} > p$ , electrons passing the gate potentially reach the grid bars due to their helical motion. This region is highlighted in red and marked as ‘critical electron radius’. For the thermal mean values of the electron velocity, an emitter temperature of  $1000^\circ\text{C}$  was assumed; a magnetic field of  $0.1\text{ T}$  was used. The calculations are performed using the example of a gate with  $(1.6\text{ mm} \times 0.08\text{ mm} \times 0.2\text{ mm})$ , corresponding to the gate used in the experimental measurements and  $d_{\text{ec}} = 800\ \mu\text{m}$ . The calculations were performed in collaboration with Stefan Meir [3].

# 6 Transition to Small-Scale, Efficient Thermoelectronic Energy Converters

The comparison of the experimental and calculated data in the previous chapter showed that the model calculations form an accurate characterization of the system. Based on these data, I will now explore the potential efficiencies of thermoelectronic converters.

To estimate the performance of the devices, I will first of all discuss the possible current densities and output power. Building on that, I will calculate the efficiencies for both autonomous heat engines and combined cycles. For solar applications, I will additionally include the photon-enhanced thermionic emission, as it greatly enhances the current densities.

Finally, and in order to look ahead to possible realizations of thermoelectronic energy converters, I will give a brief overview of material systems that are candidates for efficient thermoelectronic energy converters and will present several possible improvements to our concept.

## 6.1 Transition to Smaller Dimensions and Higher Current Densities

The experimental data and the model calculations consistently showed that the current increases for decreasing electrode distances. I will now investigate which distances are required for current densities and output powers in the range desired for applications. For small distances, gate electrodes with small mesh diameters are needed. By estimating the electrons' radius of gyration for realistic magnetic field values, I will demonstrate that even for the fine-meshed gates required, the fraction of electrons reaching the gate due to their helical motion is small.

### Possible Current Densities and Output Power

For practical applications, at least current densities of order  $1 \text{ A/cm}^2$  and power densities of order  $1 \text{ W/cm}^2$  are required. Our results show that such values can be achieved for distances in the range of  $10 \text{ }\mu\text{m}$ – $100 \text{ }\mu\text{m}$ . These values are significantly higher than the distance in close-space converters, in which the space charge is lowered by simply reducing the electrode distance (compare chapter 2.2). These devices require emitter-collector distances of about  $1 \text{ }\mu\text{m}$ .

Figure 6.1 shows the current density  $J_{\text{load}}$  in the gate meshes as a function of the emitter-collector distance  $d_{\text{ec}}$  for a gate voltage of 6 V. The graph contains the measured data for the two gates with different mesh diameters  $w$ , which we used in our experimental setup, and the calculated data for the current-tube model and the ideal-gate model including the electron velocity distribution. As discussed earlier, the ideal-gate model is a good approximation for  $d_{\text{ec}} > w$ . For decreasing distances, this condition is equivalent to  $w \rightarrow 0$ , as is indicated in the graph. The current density calculated using the ideal-gate model scales with  $1/d_{\text{ec}}^2$  (compare chapter 4.3).

For  $d_{\text{ec}} \gg w$ , the current-tube model and the ideal-gate model are equivalent. Since the current tube model neglects the initial electron velocity (compare chapter 4.4), it slightly underestimates the current density. For  $d_{\text{ec}} \lesssim w$ , the two models start to diverge, as the electric gate field becomes inhomogeneous. For very small distances, the field strength in the meshes starts to decrease (compare chapter 3.4). For this reason,  $J_c$  approaches the current density of a gate-free converter for  $d_{\text{ec}} \ll w$ .

Figure 6.1 displays current densities calculated with the current-tube model for three different gate electrodes, with  $w = 1.6$  mm,  $w = 0.6$  mm, and  $w = 0.2$  mm, respectively. The first two correspond to the gates used in our experimental setup. We included the third gate to illustrate the effect of a gate with fine meshes.

Figure 6.1 additionally shows the possible output power density  $P_{\text{load}}$ . The output power density is given by  $P_{\text{load}} = J_{\text{load}} V_{\text{load}}$ . For the ideal converter configuration,  $V_{\text{load}}$  is given by equation (2.13),  $V_{\text{load}} = (\phi_e - \phi_c)/e$ , neglecting the voltage drop in the electric circuit. Using the current density,  $P_{\text{load}}$  can therefore be calculated depending on the collector work function  $\phi_c$ . The figure displays  $P_{\text{load}}$  for different values of  $\phi_c$ , which reflect a realistic parameter range. For  $\phi_e$ , a typical value of 3 eV was assumed. Output powers of at least  $1 \text{ W/cm}^2$  can be readily achieved for distances below  $100 \mu\text{m}$ .

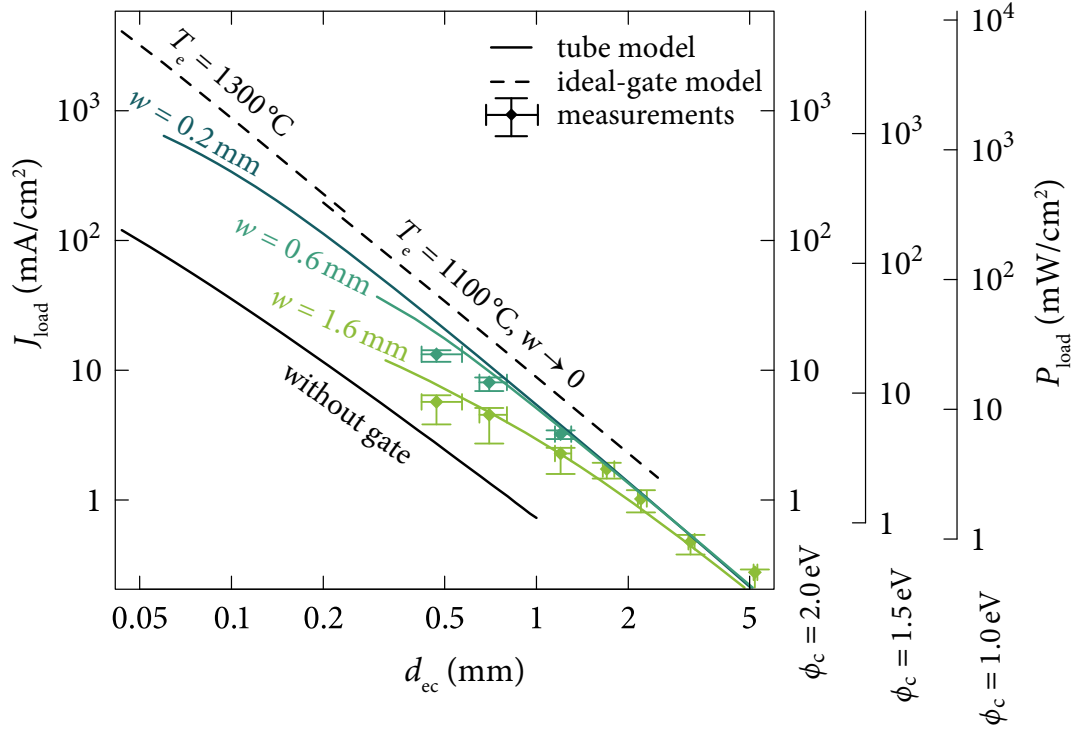


Figure 6.1: Measured and calculated current density  $J_{load}$  in the gate meshes as a function of the emitter-collector distance  $d_{ec}$ . Experimental data for two different gate electrodes are shown (compare chapter 5.3). To illustrate the possible current densities for gates with a smaller mesh diameters  $w$ , the calculated values for a gate with  $w = 0.2$  mm are shown. The ideal-gate model is a good approximation for  $d_{ec} > w$ . For very small distances, this corresponds to  $w \rightarrow 0$ . For  $d_{ec} \gg w$ , the current tube model is equivalent to a transparent gate. For  $d_{ec} \ll w$ , the current density first saturates and then approaches the values of a gate-free converter, as the electric field in the gate meshes decreases for very small distances. Data also shown in [108].

### Radius of Gyration for Small Dimensions

The electron radius of gyration  $r_{\text{gyr}}$  can be estimated analogous to the calculations performed in chapter 5.3 to assess the experimental setup.

First, the magnetic field strength that can be achieved in a small scale setup needs to be determined. I therefore calculated the magnetic field between two NdFeB magnets, identical to the ones applied in our experimental setup, with a distance of 1 cm, using the magnetic field solver ‘Amperes’ [99]. NdFeB magnets rank amongst the strongest permanent magnets commercially available [105, 109]. The calculations revealed that flux densities in the range of 0.5 T–1.2 T are possible, the exact value depending on the geometry of the magnets. As an example, I plotted the magnetic field for two 0.5 cm-thick NdFeB magnets surrounded by a steel yoke in figure 6.2. The generated field is very homogenous, with a value of about 0.6 T.

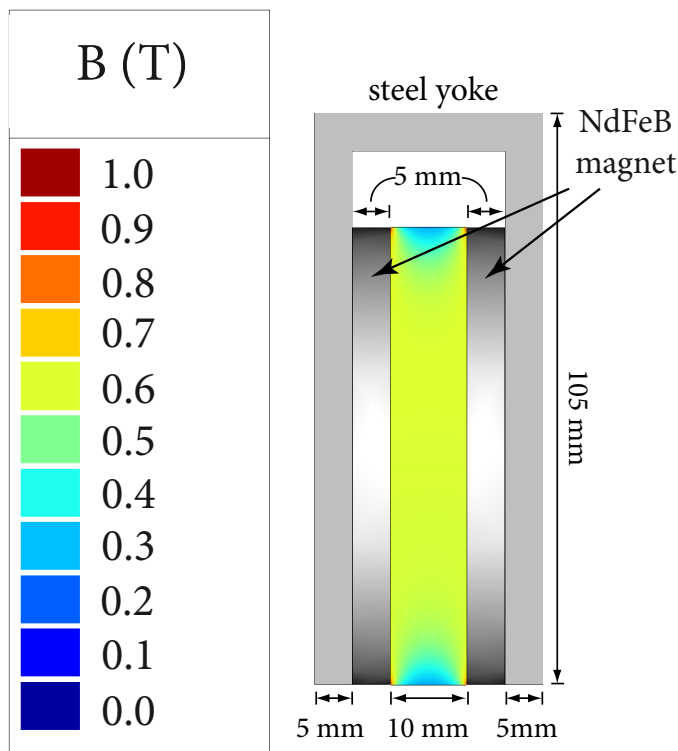


Figure 6.2: Screenshot showing the calculated magnetic field between two NdFeB permanent magnets, using the magnetic field solver ‘Amperes’ [99], for a small scale setup. The calculation is analogous to the one shown in figure 5.14. Only the dimensions of the setup have been reduced, as indicated in the sketch. The magnetic field between the two magnets is very homogeneous and has a flux density of about 0.6 T. In the calculations, the steel yoke has a relative permeability of  $\mu/\mu_0 = 1000$ , the NdFeB magnets have a remanence of  $B_r = 1.3$  T and a coercive field of  $H_c = -987 \times 10^3$  A/m.

The radius of gyration is further determined by the strength of the electrical field component  $E_{\perp}$ . I therefore calculated  $E_{\perp}$  for the example of a gate with  $w = 0.1$  mm and  $V_g = 5$  V. Figure 6.3 shows  $E_{\perp}$  along two lines, indicated in red, in the center of a gate mesh. Analogous to the previous chapter, I calculated  $r_{\text{gyr}}$  from these values, using equation (5.1) for a magnetic field of 0.5 T. The region in which the  $r_{\text{gyr}}$  exceeds the distance to the nearest gate bar is highlighted in red. Electrons passing the gate in this region can potentially reach the gate due to their helical motion. The calculations show that, in this particular example, about 15 % of the electrons pass the gate in this region. However, this value is significantly reduced when using a stronger magnetic field.

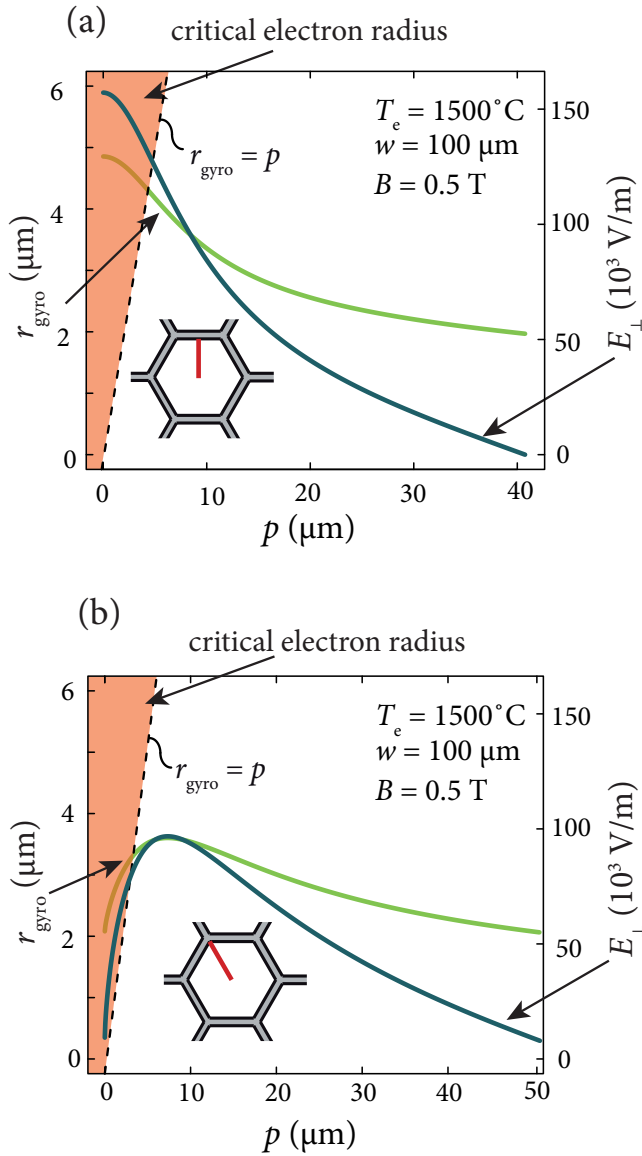


Figure 6.3: Electric field component perpendicular to the electron trajectories  $E_{\perp}$  along two different lines (indicated in red) in the center of a gate mesh with  $V_g = 5\ \text{V}$  and resulting radius of gyration  $r_{\text{gyr}}$ . For the thermal mean values of the electron velocity, an emitter temperature of  $1500^\circ\text{C}$  was assumed; a magnetic field of  $0.5\ \text{T}$  was used.  $p$  indicates the distance from the nearest grid bar. If  $r_{\text{gyr}} > p$ , electrons passing the gate potentially hit a grid bar due to their helical motion. This region is highlighted in red and marked as 'critical electron radius'. The calculations are performed using the example of a gate with  $(100\ \mu\text{m} \times 5\ \mu\text{m} \times 12.5\ \mu\text{m})$  and  $d_{\text{ec}} = 50\ \mu\text{m}$ . Calculations in collaboration with Stefan Meir [3].

## 6.2 Efficiencies of Small-Scale Thermoelectronic Energy Converters

Building on the current density calculations, the potential efficiencies of small scale thermoelectronic converters can be determined. The following calculations are based on the principles introduced in chapter 2.5. Different to ideal converters, the space-charge potential as well as the influence of the gate have to be taken into account. The current densities used in the following efficiency calculations are calculated using the ideal-gate model, which includes the thermal velocity distribution of the emitted electrons.

### Efficiency of Stand-Alone Thermoelectronic Energy Converters

To determine the efficiency of the converter, the power densities transferred to and from the system and the current densities need to be quantified. Figure 6.4 illustrates the relevant parameters in the setup, while figure 6.5 shows the corresponding electric potentials. All power quantities considered here are power densities, relating to the emitter surface  $A_e$ .

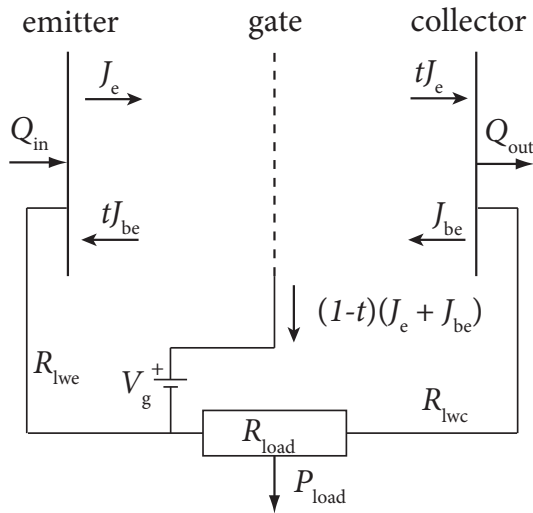


Figure 6.4: Sketch showing the parameters relevant to calculating the efficiency of a thermoelectronic converter. The heat densities inserted into and rejected from the system are indicated as  $Q_{in}$  and  $Q_{out}$ , respectively, the current densities of emitter and collector as  $J_e$  and  $J_{be}$ . A gate with the geometrical transparency  $t$  absorbs a fraction of the emitted electrons, leading to the gate current density  $J_g$ . For a small electron radius of gyration, the gate current is given by  $J_g = (1 - t)(J_e + J_{be})$ . The resistance of the lead wires connecting the emitter and collector to the load resistance  $R_{lwe}$  and  $R_{lwc}$ , respectively, are indicated, too.

The saturation current densities from emitter and collector are given by the Richardson-Dushman equation (2.4). If the space-charge potential is not reduced enough to prevent the inter-electrode potential from forming a maximum (compare chapter 4.3), a fraction of the electrons lacks the energy to overcome the potential maximum  $\Psi_{max}$ . In this case, the emitter current density  $J_e$  and the collector back emission  $J_{be}$  have to be adjusted accordingly, yielding

$$J_e = A_{RD} T_e^2 e^{-\frac{\phi_e}{k_B T_e}} e^{-\frac{\Psi_{max}}{k_B T_e}} \quad \text{and} \quad J_{be} = A_{RD} T_c^2 e^{-\frac{\phi_c}{k_B T_c}} e^{-\frac{\Psi_{max}}{k_B T_c}}. \quad (6.1)$$

The potential maximum  $\Psi_{max}$  is obtained from the ideal-gate model calculations.

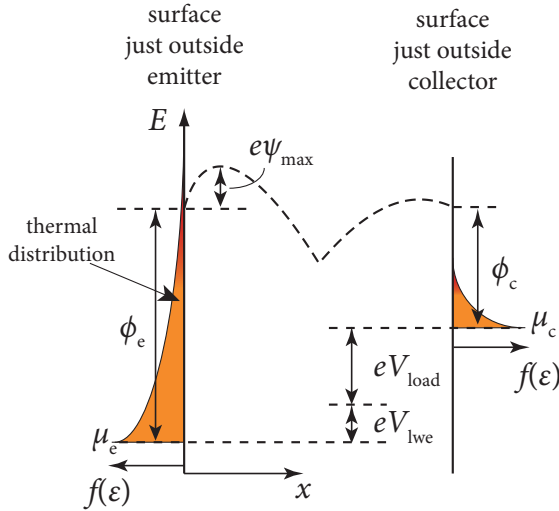


Figure 6.5: Different electrostatic potentials in a TEC, including the voltage drop due to the lead wire  $V_{lwe}$ . To reach the collector, electrons do not only have to overcome the emitter work function  $\phi_e$ , but also the maximum of the total electrostatic potential  $\Psi_{max}$ . The voltage drop in the collector wire is neglected here.

As can be seen in figure 6.4, the load current density  $J_{load}$  is given by

$$J_{load} = tJ_e - J_{be}, \quad (6.2)$$

where  $t$  indicates the geometrical transparency of the gate. This leads to the load voltage  $V_{load}$  and the load power density  $P_{load}$  of

$$V_{load} = \frac{\phi_e - \phi_c}{e} - R_{lwe} A_e (J_e - tJ_{be}), \quad (6.3)$$

$$P_{load} = J_{load} V_{load} = (tJ_e - J_{be}) \left( \frac{\phi_e - \phi_c}{e} - R_{lwe} A_e (J_e - tJ_{be}) \right). \quad (6.4)$$

To achieve high efficiencies, the collector must be cold. The lead wire connecting the collector to the load resistance can therefore be optimized for a low electric resistivity, neglecting the heat transport away from the collector. Consequently, the ohmic loss in the collector lead wire is small and will be neglected here.

The power density consumed by the gate  $P_g$  depends on the gate current density  $J_g$  (see figure 6.5) and is given by

$$P_g = J_g V_g = (1 - t)(J_e + J_{be}) V_g. \quad (6.5)$$

The heat transfer away from the emitter consists of three contributions: the electron cooling  $P_{ec}$ , the radiation cooling  $P_{rc}$  and the heat transfer through the emitter lead wire  $P_{lwe}$ . They can be derived analogous to an ideal converter, as done in chapter 2.5. Additionally,

the influence of the gate and the space-charge potential have to be considered (figure 6.5), leading to

$$P_{ec} = \frac{J_e}{e}(\phi_e + \Psi_{\max} + 2k_B T_e) - t \frac{J_{be}}{e}(\phi_e + \Psi_{\max} + 2k_B T_c), \quad (6.6)$$

$$P_{rc} = \varepsilon_{\text{eff}} \sigma (T_e^4 - t T_c^4), \quad (6.7)$$

$$P_{lwe} = \frac{1}{2} \frac{L}{R_{lwe} A_e} (T_e - T_0)^2 - \frac{1}{2} (J_e - t J_{be})^2 R_{lwe} A_e. \quad (6.8)$$

The load resistance is assumed to be at room temperature  $T_0 = 300$  K.

Taking into account all contributions, the efficiency of thermoelectronic energy converters is given by

$$\eta = \frac{P_{\text{load}} - P_g}{P_{ec} + P_{rc} + P_{lwe}}. \quad (6.9)$$

### Additional Energy Loss for Solar Heated TECs

If the emitter is heated by solar radiation, it has to be considered that a fraction of the incoming heat is lost again by the radiation from the area absorbing the sunlight. To estimate this energy loss, I assume a black cavity with an opening for the incoming solar radiation<sup>1</sup>. One wall of the cavity is connected to the emitter, thus providing heat to the TEC. In thermal equilibrium, the temperature in the cavity is equivalent to the emitter temperature  $T_e$ .

The following equation has to be fulfilled

$$P_{\text{sol,in}} = P_e + P_{\text{hole}}, \quad (6.10)$$

where  $P_{\text{sol,in}}$  is the incoming solar radiation,  $P_e$  the power consumed by the emitter and  $P_{\text{hole}}$  the radiated power through the opening. The cavity is assumed to be a perfect black radiator.

$$P_{\text{sol,in}} = C S_{\text{sol}} A_{\text{hole}}, \quad (6.11)$$

$$P_e = A_{\text{hole}} \sigma T_e^4, \quad (6.12)$$

with the concentration factor  $C$ , the Stefan-Boltzmann constant  $\sigma$  and the energy flux density of the solar radiation  $S_{\text{sol}}$ . Outside the Earth's atmosphere,  $S_{\text{sol}}$  is given by the solar constant  $E_0$  of about  $1360 \text{ W/m}^2$ . On the Earth's surface,  $S_{\text{sol}}$  can reach values up to about  $1000 \text{ W/m}^2$  in specific regions, mostly deserts.

<sup>1</sup>The considerations are the same if the emitter has an area, e.g., on the back side, which is used to absorb the sunlight.

From the equations shown above, it follows that the ratio of the radiated heat to the power consumed by the emitter is given by

$$\frac{P_{\text{hole}}}{P_e} = \frac{1}{CS_{\text{sol}}/\sigma T_e^4 - 1}. \quad (6.13)$$

The efficiency of a solar heated TEC  $\eta_{\text{sol}}$  can be expressed in terms of the efficiency of a conventionally heated TEC as follows

$$\eta_{\text{sol}} = \frac{P_{\text{load}}}{P_e + P_{\text{hole}}} = \eta \left( 1 - \frac{\sigma T_e^4}{CS_{\text{sol}}} \right). \quad (6.14)$$

This means that the influence of the radiation heat loss depends only on the emitter temperature and the concentration factor.

The limit for optical concentration of the solar flux in media with an index of refraction of 1 is given by  $C_{\text{max}} \approx 46000$  [110]. Technically, concentration factors of about 10000 are possible today [111], while Stirling Dishes with values of 3000 are already in use [15].

Figure 6.6 shows the ratio  $\eta_{\text{sol}}/\eta$  as a function of the emitter temperature  $T_e$  for different concentration factors. It becomes evident that a high concentration factor is needed if high temperatures are considered.

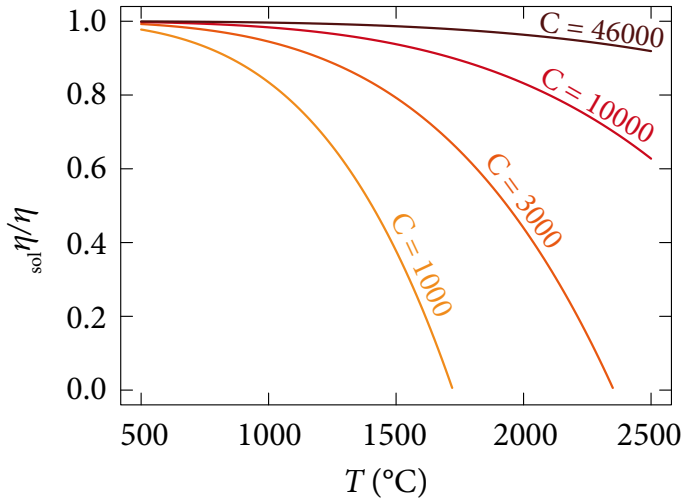


Figure 6.6: Ratio of the efficiency of a solar heated TEC  $\eta_{\text{sol}}$  to the efficiency of a conventionally heated TEC  $\eta$  as a function of the emitter temperature  $T_e$  for different concentration factors  $C$ . A solar energy flux density of  $900 \text{ W/cm}^2$  was assumed, corresponding to the AM1.5 direct+circumsolar reference spectrum [112]. Data calculated by Stefan Meir [3].

### Results from the Efficiency Calculations for Stand-Alone TECs

Figure 6.7 illustrates the efficiency of a thermoelectronic energy converter as a function of the load voltage  $V_{\text{load}}$  for the realistic set of parameters:  $\phi_e = 2.7 \text{ eV}$ ,  $\phi_c = 0.9 \text{ eV}$ ,  $T_c = 200 \text{ }^\circ\text{C}$ ,  $d_{\text{ec}} = 30 \text{ } \mu\text{m}$ ,  $t = 0.98$  and three different emitter temperatures  $T_e$ . Furthermore, the efficiency of a TEC using photon-enhanced thermionic emission [9] is shown, indicated as PETE. To explore possible efficiencies for solar applications, we also included data for an optimized collector with a work function of  $\phi_e = 0.55 \text{ eV}$ .

The efficiencies of conventionally heated thermoelectronic energy converters for the chosen setup reach values up to 40 %, which clearly exceeds efficiencies possible with thermoelectric converters. The efficiency values for TECs can be even higher for optimized collector work functions and smaller emitter-collector distances.

The main advantage of using PETE is that high current densities can be already achieved for moderate emitter temperatures, leading to a lower heat radiation loss and therefore very high efficiency values. When using PETE, TECs are not limited by the Carnot efficiency (compare chapter 2.5). Thermoelectronic energy converters heated with solar radiation have the potential to reach efficiencies exceeding the values attainable with conventional solar cells or solar heated mechanical heat engines [45, 46].

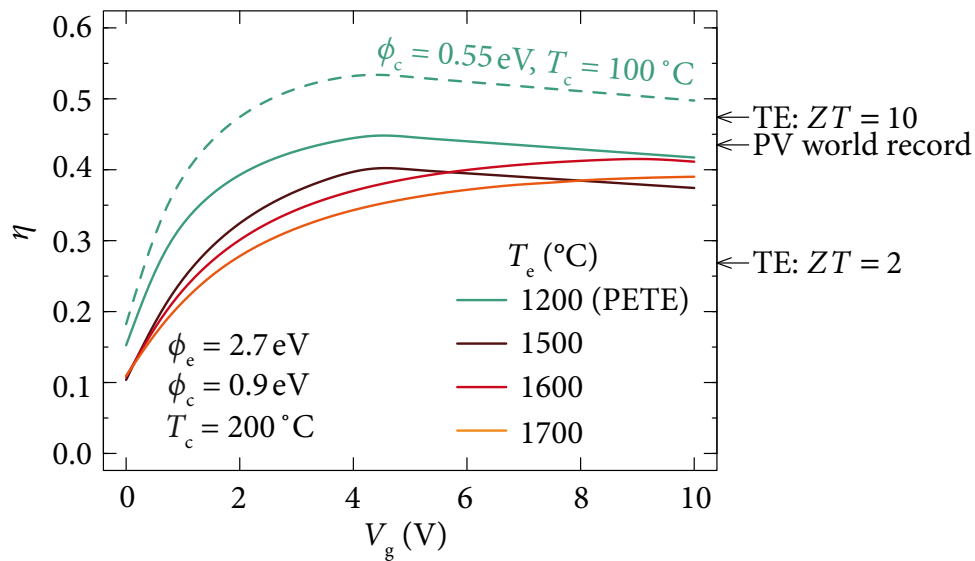


Figure 6.7: Efficiency of stand-alone thermoelectronic energy converters as a function of the gate voltage  $V_g$ . The three red-brown curves are data for conventional heated TECs. The green curves are calculated for solar heated TECs, using photon-enhanced thermionic emission [9]. The parameters shown at the bottom left are valid for all continuous lines. A solar concentration factor of 10000 and a solar energy flux density of  $900 \text{ W/cm}^2$ , corresponding to the AM1.5 direct+circumsolar reference spectrum [112], were assumed. The additional radiation heat loss due to the solar concentrator was also taken into account. The band gap and the electron affinity of the PETE-emitter was determined in a self-consistent calculation, depending on the defined current density and the emitter temperature [3]. As a comparison, the efficiency of best research multi-junction photovoltaic cells of 43.5% [113] is indicated. Furthermore, the efficiencies for thermoelectric converters with  $ZT$  values of 2 and 10, are indicated. Best practice thermoelectric devices reach  $ZT$  values of about 1 [49] (compare chapter 2.6). Stefan Meir calculated the efficiencies based on the current densities, which I calculated using the ideal-gate model. Data also shown in [108].

The gate transparency  $t$  is an crucial parameter for the efficiency of thermoelectric converters. A high value of  $t$  leads to a small power loss at the gate. To investigate the influence of  $t$  on the efficiency, we calculated the efficiencies for different transparencies. Figure 6.8 shows an extract of the results for a typical set of parameters. For a transparency of 1, no

electrons reach the gate. In this case, the gate voltage could be increased until the current density reaches its saturation value. The efficiency of a TEC would then be equivalent to the efficiency of an ideal converter.

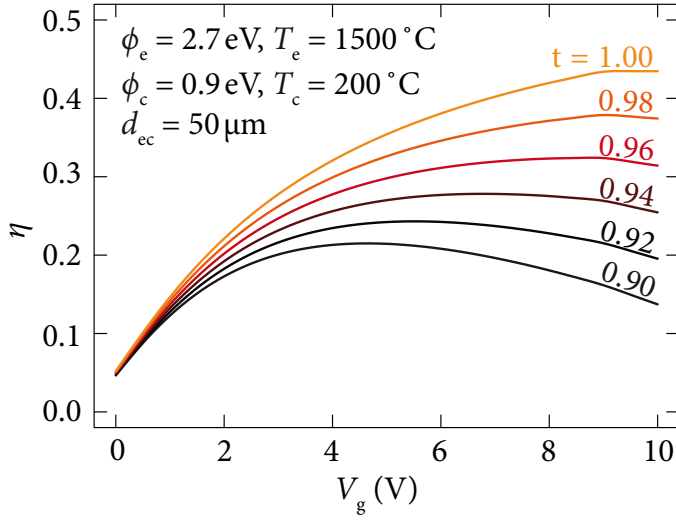


Figure 6.8: Efficiency of TECs as a function of the gate voltage  $V_g$  for different geometrical transparencies  $t$  of the gate electrode. Stefan Meir calculated the efficiencies based on the current densities, which I calculated using the ideal-gate model. Data also shown in [108].

In our experimental setup, we used laser-cut gates with geometrical transparencies of  $t = 0.89$  and  $t = 0.72$ , respectively. By optimizing the structuring process or employing microelectronic technology, higher values should certainly be possible. At the end of this chapter, I will furthermore discuss several improvements to our setup that should enable us to effectively increase the transparency.

The power lost at the gate can be compared with the different contributions of the heat transferred away from the emitter: the electron cooling, the heat radiation and the heat transported through the emitter lead wire. For high transparencies, however, the power consumed by the gate is small compared to all three contributions. The ratio of the different loss channels is therefore virtually the same as in an ideal converter (see chapter 2.5).

### Efficiency in Combined-Cycle Systems Using TECs as Topping Cycles

If TECs are used as topping cycles, the rejected heat from the collector  $Q_{\text{out}}$  is used to power a second heat engine. The heat transport from the collector therefore has to be considered and the collector lead wire cannot be optimized only for electrical transport. Consequently, the collector lead wire resistance  $R_{\text{lwc}}$  cannot be neglected and the load voltage has to be modified accordingly to

$$V_{\text{load}} = \frac{\phi_e - \phi_c}{e} - R_{\text{lwe}} A_e (J_e - t J_{\text{be}}) - R_{\text{lwc}} A_e (t J_e - J_{\text{be}}). \quad (6.15)$$

The load power is then given by

$$P_{\text{load}} = (t J_e - J_{\text{be}}) \left( \frac{\phi_e - \phi_c}{e} - R_{\text{lwe}} A_e (J_e - t J_{\text{be}}) - R_{\text{lwc}} A_e (t J_e - J_{\text{be}}) \right). \quad (6.16)$$

The heat transfer to the collector consists of three parts: the electron heating  $P_{\text{eh}}$ , the radiation heating  $P_{\text{rh}}$  and the heat conductance through the collector lead wire  $P_{\text{lwc}}$ . Again, the influence of the space-charge potential and the gate with the geometrical transparency  $t$  have to be considered, leading to

$$P_{\text{eh}} = t \frac{J_e}{e} (\phi_c + \Psi_{\text{max}} + 2k_B T_e) - \frac{J_{\text{be}}}{e} (\phi_c + \Psi_{\text{max}} + 2k_B T_c), \quad (6.17)$$

$$P_{\text{rh}} = \varepsilon_{\text{eff}} \sigma (t T_e^4 - T_c^4), \quad (6.18)$$

$$P_{\text{lwc}} = -\frac{1}{2} \frac{L}{R_{\text{lwc}} A_e} (T_c - T_0)^2 + \frac{1}{2} (t J_e - J_{\text{be}})^2 R_{\text{lwc}} A_e, \quad (6.19)$$

$$Q_{\text{out}} = P_{\text{eh}} + P_{\text{rh}} + P_{\text{lwc}}. \quad (6.20)$$

Assuming an efficiency of the second heat engine of  $\eta_s$ , the overall efficiency of the combined cycle is obtained as

$$\eta_{\text{tot}} = \frac{P_{\text{load}} - P_{\text{g}} + \eta_s Q_{\text{out}}}{P_{\text{ec}} + P_{\text{rc}} + P_{\text{lwc}}}. \quad (6.21)$$

Figure 6.8 shows the efficiency of a combined-cycle system using TECs as topping cycles for an emitter-collector distance of  $d_{\text{ec}} = 30 \mu\text{m}$  and a gate transparency of  $t = 0.98$ . The secondary heat engine is a steam turbine typically applied in coal-combustion power plants today. It works with an inlet temperature of  $600 \text{ }^\circ\text{C}$  and an efficiency of  $\eta_s = 45 \%$  [2, 114]. The collector temperature  $T_c$  needs to be equivalent to the inlet temperature of the steam turbine. The collector work function  $\phi_c$  was optimized for high efficiencies, yielding values of about  $1.5 \text{ eV}$  for all data shown here. The figure also shows the efficiency of solar heated TECs using PETE, for an emitter temperature of  $T_e = 1500 \text{ }^\circ\text{C}$ .

Different to stand-alone converters, the heat radiated from the emitter is not lost in combined-cycle systems. Most of this heat is absorbed on the collector and used to power the secondary heat engine. Here, the advantage of using PETE over conventional heated TECs is therefore not as significant as in stand-alone converters. In the example shown in figure 6.9, this advantage is almost exactly canceled out by the heat radiated from the solar concentrator.

In all cases considered, the efficiency of the steam turbine is boosted by using a TEC as a topping cycle by a value of about  $10 \%$ . This is a significant improvement and leads to an overall conversion efficiency of about  $55 \%$ .

### 6.3 Possible Material Classes for Practical, Thermoelectronic Converters

In this section, I will give a brief overview of material systems that could be used for practical, efficient thermoelectronic energy converters. As discussed below, finding suitable materials for TECs used as topping cycles should not present a problem today. For stand-

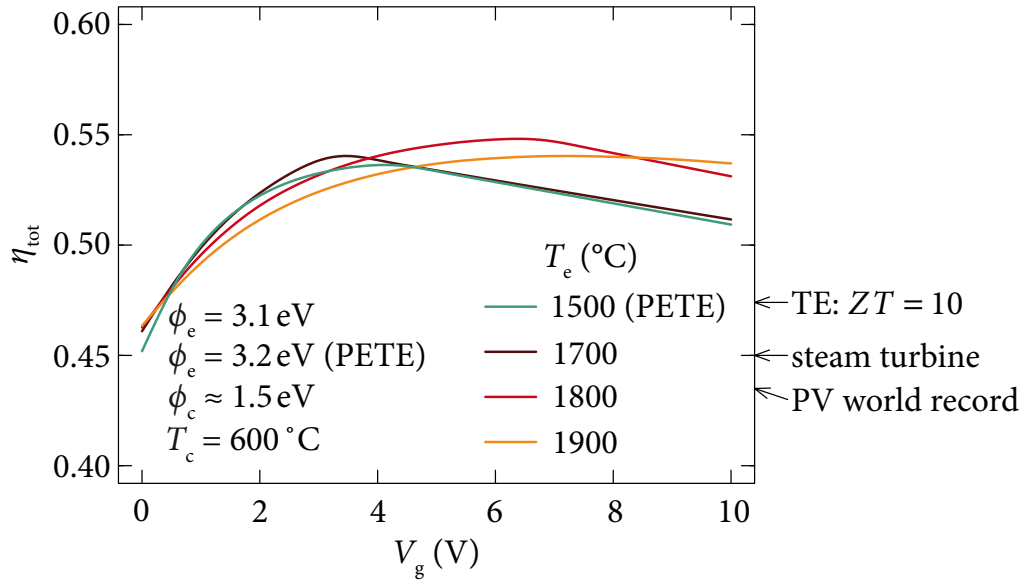


Figure 6.9: Efficiency of combined-cycle systems using a TEC as a topping cycle as a function of the gate voltage  $V_g$ . As secondary heat engine, a steam turbine with inlet temperature  $600\text{ °C}$  and efficiency  $\eta_s = 45\%$  is considered [2, 114]. The three red-brown curves are data for conventional heated TECs. The green curve is calculated for a solar heated TEC, using photon-enhanced thermionic emission [9]. A solar concentration factor of 10000 and a solar energy flux density of  $900\text{ W/cm}^2$ , corresponding to the AM1.5 direct+circumsolar reference spectrum [112], were assumed. The additional radiation heat loss due to the solar concentrator was also taken into account. The band gap and the electron affinity of the PETE-emitter was determined in a self-consistent calculation, depending on the defined current density and the emitter temperature [3]. As a comparison, the efficiency of best research multi-junction photovoltaic cells [113], as well as efficiencies for thermoelectric converters with  $ZT$  value 10, are indicated. Stefan Meir calculated the efficiencies based on the current densities, which I calculated using the ideal-gate model. Data also shown in [108].

alone devices, however, the collector work functions need to be very low, which still is a challenge. Nonetheless, several promising possibilities exist.

Emitter surfaces typically require work functions in the range of  $2\text{ eV}$ – $4\text{ eV}$ . Furthermore, the emitter material needs to be high-temperature resistant. A wide range of materials with high electron-emission characteristics, suited as emitter material are known today. For example, barium-doped tungsten cathodes, like the one used in our experimental setup, which are stable over many years, are commercially available [28, 106, 115–118]. Moreover, by using refractory metals coated with few atomic layers of chemical elements, such as Ba, Cs or La, almost any work function in the desired range can be obtained [16]. For microthermionic converters, thin-film techniques have already been successfully applied to produce suitable emitter materials [19].

For the collector materials, combined-cycle systems and stand-alone converters have to be discussed separately. When TECs are used as topping cycles, the work function needs to be in the range of about  $1\text{ eV}$ – $1.5\text{ eV}$ . Such values can be obtained, for example, with caesiated metal surfaces, such as tungsten, barium, titan or tantalum [16]. This can either

be done by coating the metal surface using thin film techniques, or by inserting a low pressure Cs vapor into the converter [6, 24, 29].

If Cs vapor is used in the converter, the work function reduction depends on the coverage of the metal surface. A high coverage leads to a small work function [6]. The coverage, however, depends on the surface temperature. For high temperatures, the evaporation of the absorbed elements is strong. A high surface temperature therefore leads to only a small modification of the work function. This effect is exploited in vapor diodes to create a difference in the work function between the hot emitter and the cold collector, both made of the same refractory metal [6].

For stand-alone converters, the collector work function should ideally be smaller than 1 eV. However, the materials do not need to be high-temperature resistant, as the collector needs to be cold for high efficiencies. Not many longtime stable material systems with such low work functions are known. This may, however, be due to the fact that such materials have very limited applications; most materials with very low work functions also have low electron emission characteristics [16]. The main application area, on the other hand, are cathodes used to generate high emission currents. For TECs, the low emission characteristics are useful, because they lead to a low collector back emission.

Recently, phosphorus-doped polycrystalline diamond films on metallic substrates were reported to have work functions of about 0.9 eV, stable up to temperatures of 765 °C [119]. Although this material has very low emission properties, it was mainly studied for electron emission purposes. But it has also been considered for thermionic devices [9, 119–122].

The most promising approach seems to be the coating of metal surfaces with chemical elements or chemical compounds. Especially the addition of oxygen seems to have a strong influence on the work function. The reason is presumably a strong polarization of the surface layers. Cs-oxide on tungsten, Cs on  $W_2O$ , or a combination of BaO and SrO, all reach work functions in the range of 0.7 eV–1 eV [16], while having very low electron emission properties.

One aspect that should be considered when designing emitter and collector materials, is that the work function is mainly determined by the outer few atomic layers of a surface. The infrared thermal radiation and reflection of radiation, on the other hand, is determined by a much thicker surface layer, of order  $10^{-6}$  m [48]. It should therefore be possible to optimize the materials for both work functions and radiation properties. Thereby, the energy loss due to heat radiation could be significantly reduced.

## 6.4 Potential Enhancements to Our Concept

To conclude this chapter, I will outline potential enhancements that can be applied to our new concept and make use of the unique properties of our setup.

### Schottky Effect and Selective Electron Emission

Thermoelectronic converters have the unique advantage over other thermionic or even thermoelectric devices, that the gate electric field can be used to influence the converter

parameters. One example is the use of the gate electrode to increase the electron emission by exploiting the Schottky effect (compare chapter 2.4). The required E-fields, typically above  $10^6$  V/m, could be generated with very high voltages.

A more elegant method, however, would be to nanostructure the emitter surface by creating nano-hillocks (figure 6.10). The electric field would be greatly enhanced at the tips, leading to a strong local electron emission.

This method further opens up the possibility of confining the electron emission to certain areas on the emitter surface. By omitting the area facing the gate bars, we could significantly reduce the gate loss current. This can also be described as an effective increase of the gate transparency.

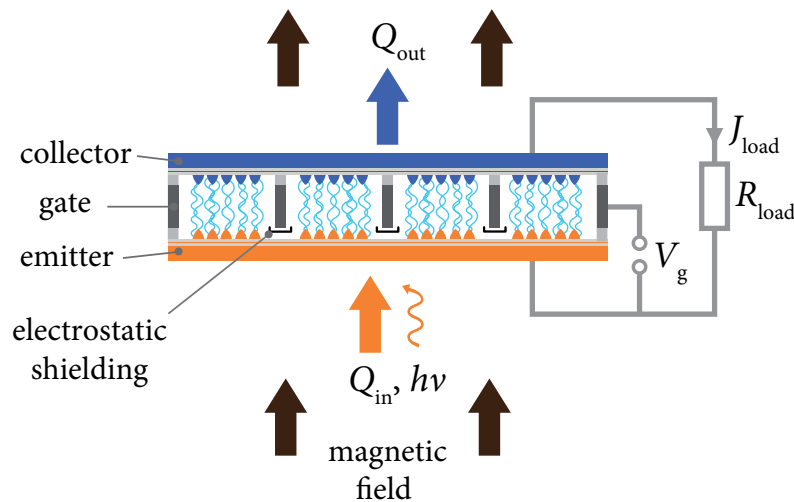


Figure 6.10: Sketch of a fully integrated TEC featuring several potential improvements to our concept. Nano-hillocks on the emitter surface locally enhance the electric field. The gate field can then be used to increase the emitter current by exploiting the Schottky effect [36]. The nanostructure of the emitter surface can be further adjusted to match the gate structure, thereby significantly lowering the gate loss current. An electrostatic shielding of the gate-front face would decrease the electric field on the emitter areas facing the gate bars, thereby further reducing the gate current. The two grey lines in emitter and collector indicate a surface that optimizes the infrared properties of the materials, thus reducing the heat radiation energy loss (compare chapter 6.3). Drawing from [108].

### Gate Electrode with Shielding Layer

To reduce the electron emission at the areas on the emitter surface facing the gate bars, the front face of the gate electrode could be covered by an insulating material (see figure 6.10). The electric field accelerating the electrons away from the emitter would be generated by the side walls and the back side of the gate, and would be stronger in the gate meshes. The gate loss current would be significantly reduced.

By negatively charging the front face of the gate, the electron emission at the areas on the emitter surface facing the gate bars could even be further reduced. A negative charge

can be achieved by collecting few emitted electrons or by applying a negative voltage to the front face of the gate.

It might be even possible to cover the side walls of the gate electrode, thus creating the accelerating electric field only by the back side. In such a configuration, electrons would barely experience any force towards the gate bars until they have passed the gate meshes. Such a configuration would virtually abolish the gate current. However, it needs to be investigated whether the electric field generated by the gate-back side of the gate is strong enough to significantly reduce the space-charge potential.

### **Gate with Adjusted Work Function**

Another alternative for decreasing the power loss at the gate,  $P_g = V_g J_g$ , would be to use a gate with a work function smaller than that of the emitter. In this case, the contact potential would create a voltage difference of  $(\phi_e - \phi_g)/e$  between emitter and gate. The applied gate voltage could be lower by this value, thus reducing  $P_g$ . For very small distances, the contact potential could even create a sufficient electric field to reduce the space charge without an additional applied gate voltage. This method would significantly simplify the setup, as the gate would not need to be electrically connected.

### **Use of an Inhomogeneous Magnetic Field**

A slightly inhomogeneous magnetic field could be applied, whose field lines do not extend through the gate bars, but avoid them. Thereby, all emitted electrons could be channeled through the gate openings, reducing the gate loss current. Such a field could be generated, for example, by using small permanent magnets, whose positions match the gate openings, or by nanostructuring the surface of a magnetic material.

### **Superconducting Coils for Magnetic Field Generation**

For large applications, the magnetic field could be generated by superconducting coils. With this method, very homogeneous fields of the order of several Tesla can be obtained. This would enable the use of extremely fine-meshed gates, because the radius of gyration of the electrons could be extremely small.

## 7 Summary

Thermionic energy converters face the problem that a space-charge region is formed between the electrodes, dramatically reducing the current densities and ruining the performance of the devices. Despite intensive efforts, no solution was found. In this thesis, I showed that this problem can be solved, thereby opening up the way to highly-efficient heat-to-electricity energy conversion.

Our concept uses an electric field, generated by a gate electrode, to accelerate the electrons away from the concentrated space-charge cloud. A magnetic guiding field is applied to prevent the electrons from reaching the gate, a honeycomb structured metal grid, by channeling them through the gate openings. This concept is based partly on previous considerations, but avoids their design flaws, which led to high loss currents and low output powers. In our concept, the previously static charges, which generated a strong space-charge region, are converted into a useful output current in a virtually lossless process.

As a first step for modeling the electron behavior in the setup, I recalled the motion of charged particles in combined electric and magnetic fields and deduced important implications for thermoelectronic converters. The magnetic field forces the electrons to perform a helical motion along the magnetic field lines, if the condition  $cB > E_{\perp}$  is fulfilled, where  $B$  indicates the magnetic flux density and  $E_{\perp}$  the electrical field component perpendicular to the magnetic field. In addition to their longitudinal motion, the electrons perform a drift in the direction perpendicular to both  $B$  and  $E_{\perp}$ . As  $E_{\perp}$  always points to the closest gate bar, the electrons are not moving towards the gate. As a consequence, only a small fraction of the emitted electrons reach the gate.

Building on these considerations, I outlined several issues that should be considered when designing thermoelectronic converters using electric and magnetic fields, and illustrated the flaws of previous models.

To estimate the current densities attainable with TECs, the electric potential of the space charge has to be determined. I therefore used a three-dimensional particle tracing software with integrated electric and magnetic field solvers to calculate the electron motion in the setup. However, it became evident that this approach is not conducive to calculating the current densities, as the calculations do not converge in many cases and the computational effort is too high.

By investigating the electric field, I could show that the electron motion can be mapped onto a one-dimensional system. In this model, the gate electrode is approximated by an ideal gate, which is equivalent to a metal plate that is transparent for electrons.

Based on established space-charge theories, I developed a model for the ideal gate, which allowed me to calculate the space-charge potential and the current densities. It further enabled me to determine the optimal geometrical configuration for thermoelectronic con-

verters: a symmetrical setup, with the gate electrode mounted exactly in the middle between emitter and collector.

One of the main results of the model calculations is that the current density scales with  $1/d_{ec}^2$  for a given gate voltage, where  $d_{ec}$  is the emitter-collector distance. I furthermore calculated the required electric field for an optimal electron yield. Decreasing values of  $d_{ec}$  decrease the required field voltage and simultaneously increase current densities with  $d_{ec}$ .

The ideal-gate model is a good approximation for high electrode distances, *i.e.*  $d_{ec} > w$ , where  $w$  represents the diameter of the gate meshes. For smaller distances, the gate field becomes inhomogeneous. In collaboration with Stefan Meir, I therefore developed an approach to include these inhomogeneities in the model calculations. It divides the inter-electrode space into separate volumes and calculates the current density in each volume using the ideal-gate model. This allows us to account for the three-dimensional distribution of the gate electric field.

To investigate the model experimentally, we created a mechanical electrode setup, mounted in a vacuum chamber. It allowed us to show that the gate voltage can be used to control the current on the collector and demonstrate the channeling effect of the magnetic field for different geometrical configurations.

Comparing our experimental results with the calculated values provided evidence that the model calculations coincide closely with our investigated system, proving that the concentrated space-charge region can indeed be removed.

According to my calculations, for output powers in the range desired for applications and high efficiencies, electrode distances in the range of 10  $\mu\text{m}$ –100  $\mu\text{m}$  are required, applying gate voltages of typically 2 V–10 V. Such devices could be built using microtechnology and could potentially produce hundreds of Watts output powers from active areas of about 100  $\text{cm}^2$ .

Stand-alone devices can work at efficiencies of over 40 %, assuming a realistic set of material parameters. If the converters are heated with solar radiation, the electron emission can be enhanced by exploiting the photoelectric effect in a semiconducting emitter [9]. In this case, TECs, not limited by the Carnot efficiencies, can reach efficiencies of more than 50 %, clearly exceeding the efficiency of best research multi-junction photovoltaic cells of 43.5 % [113].

I further illustrated the applicability of TECs as topping cycles in combination with secondary heat engines. For both conventionally and solar heated systems, the conversion efficiencies of established techniques could be boosted by more than 10 %.

Finding materials used for TECs working as topping cycles appears attainable today. For highly-efficient stand-alone devices, further material research efforts are needed; however, promising approaches exist. Especially the coating of metal surfaces with oxide materials holds great potential.

Finally, I explored potential enhancements to our model, exploiting the unique advantage of TECs over conventional thermionic converters. For example, by nano-structuring the surface, gate-field enhanced thermionic electron emission could be applied to enhance the current densities. Furthermore, by adjusting the area of the nano-structures to the gate pattern, the gate current can be significantly reduced.

## 8 Conclusion

Thermoelectronic energy converters hold the potential to have a sustained impact on electricity generation. Their full potential, however, has not been recognized, although their underlying concept has been known for over 100 years. In this thesis, I was able to show that the fundamental problem preventing the application of this technology can, in fact, be solved.

Practical converters could be realized as fully integrated devices with a flip-chip electrode arrangement, requiring a vacuum of the order of  $10^{-1}$  mbar, reminiscent of radio tubes. Engineering efforts are now required to minimize the heat loss, guarantee a stable vacuum environment and thermally insulate critical components, such as the permanent magnets. Apart from this technical perspective, the main challenge remaining is to find suitable collector materials.

Oxide materials, which feature a very broad range of physical properties, seem to be perfect candidates for encountering this challenge. Using thin-film techniques like pulsed-laser deposition or molecular-beam epitaxy enables an exact growth of oxide surfaces, with varying stoichiometrical composition to adjust the desired properties. I am convinced that, through a concentrated scientific effort, this challenge could be overcome in the near future.

Our new concept could also be expanded to operate thermoelectronic converters as heat pumps, used, *e.g.*, for microtechnology computer cooling. Thermionic converters have been considered for such applications. Our concept, however, could significantly enhance their performance and be used to produce very low energy consuming, completely silent devices, due to their virtually space-charge free electron transport. The gate field could further be used for field-enhanced electron emission, or even Fowler-Nordheim electron tunneling, thereby dramatically increasing the electron current without high energy losses.

Thermoelectronic energy converters offer exciting, new challenges and opportunities for our energy-driven society. I hope that a concerted effort will be made to fully exploit their tremendous potential.



# A Appendix

## A.1 Source Code for the Numerical Calculations

All codes shown below were used for Mathematica 8.0.1.0 [101].

### Source Code for equation (4.55) on page 71

For the example of a variable gate-position  $x_g$ .

```
me = 9.10938215*10^-31 (*kg*); eps0 = 8.8541878176*10^-12 (*As/Vm*); e0 = 1.602176487*10^-19;
kB = 1.3806488*10^-23;

conv0 = 1*10^-9; n = 0; Listi = {}; List2i = {};
xG = 2.5*10^-6; VG = 2; EG = VG/xG; T = 1500;

J0 = eps0/Sqrt[6]*Sqrt[e0/me]*VG^(3/2)/xG2
Jn[x_] := J0 = eps0/Sqrt[6]*Sqrt[e0/me]*VG^(3/2)/x2/10^4 (* in A / cm\ .b2 *)

For[i = 1, i <= 400, i++,

kleindone = 1; grossdone = 10000000/(i/4)^2;

xG = (10*i/4)*10^-6;
EG = VG/xG;

For[n = 0, n <= 500, n++,
{
Ji = (grossdone + kleindone)/2;

soli =
NDSolve[{Phi'[x] == -Ji/eps0*1/N[Sqrt[(2*e0/me)*(-Phi[x] + EG*x + Ekin0)]], 50], Phi[0] == 0, Phi
'[0] == EG}, Phi, {x, 0, xG}, MaxSteps -> Infinity, WorkingPrecision -> 20, PrecisionGoal ->
20];

If[Abs[Last[Phi'[xG] /. soli]] < conv0,
{Print["Iteration", i, "\n", n, "Ji=", NumberForm[N[Ji], ExponentFunction -> (Null &)],
"slope:", Last[Phi'[xG] /. soli]};
Listi = Append[Listi, {xG, Ji/10^4};
List2i = Append[List2i, {xG, Ji/10^4/Jn[xG]}; Break[];},
];
If[Last[Phi'[xG] /. soli] < 0, grossdone = Ji, kleindone = Ji];
}]]
```

### Source Code for equation (4.32) on page 65 and equation (4.69) on page 76

Both equations can be solved using the same algorithm. For the case of no gate, the gate voltage  $V_g$  must be set zero.

## A Appendix

```

T = 1400 + 273; d = 30*10-6; PhiEO = 2.7*e0 (*emitter work function eV*);

me = 9.10938215*10-31 (*kg*); eps0 = 8.8541878176*10-12 (*As/Vm*); e0 = 1.602176487*10-19
(*C*); kB = 1.3806488*10-23 (*J/K*); h0 = 6.62606957*10-34 (*Js*);

conv1 = 4*10-3; conv2 = 1*10-5; nmax = 1000; imax = 100;
(* convergence criteria for-loop *)

JRD = e0*me/(2*Pi2*(h0/(2*Pi))3*(kB*T)2* Exp[-PhiEO/(kB*T)]
(*saturation current density in A/m2*);
JRDcm = JRD/104 (*saturation current density in A/cm2*);

starttime = TimeUsed[];

For[qq = 4, qq <= 4, qq++,

  countsat = 0; (* Counter, der prüft, ob die Gatespannung hochgenug ist, um die
  Sättigungsstromdichte zu erreichen; wenn ja, muss das E-Feld nicht
  mehr weiter erhöht werden, da nicht mehr Strom erzeugt werden kann *)

  T = 1400 + 273 + 100*qq;
  (*VGate = 5;*)

  JRD = e0*me/(2*Pi2*(h0/(2*Pi))3*(kB*T)2*Exp[-PhiEO/(kB*T)] (*Sättigungsstromstärke in A/m2*);
  JRDcm = JRD/104 (*Sättigungsstromstärke in A/cm2*);
  n0 = 1/e0*JRD*(Pi*me/(2*kB*T))(1/2) (*Anfangsteilchendichte bei x=0*);

  For[vv = 6, vv <= 20, vv++,
  {

    speed = 0.3; (* ; die Variable speed gibt an,
    wie stark die Raumladung, die in die Lösung eingeht,
    verändert wird, nachdem die erste Schleife konvergiert ist;
    speed muss zwischen 0 und 1 liegen; desto größer der Wert,
    desto schneller wird die Raumladung verändert;
    je stärker die Raumladung, desto kleiner muss speed sein;
    der speed sollte am besten nicht über 0.4 liegen *)

    (*d= (28 - 0.1*vv)*10-6*)
    xG = d/2;

    VGate = vv/2;

    EO = 2*VGate/d;

    EGate[x_] := EO*xG - Abs[EO*xG - EO*x];

    Print["Durchgang", qq, " ", vv, " ", "Temperatur:", T, " ", "E-Feld:", EO, " ", "VGate:", VGate
    , " ", "d_ec:", NumberForm[N[d/10-6], ExponentFunction -> (Null &)], "[Micro]m"];

    (* Zuerst wird überprüft, ob in dem vorigen Schritt bereits die Sättigung erreicht wurde;
    wenn ja, sind alle weiteren Rechnungen bei dieser T,
    diesem Abstand nicht mehr notwendig *)
    If[countsat == 1,

    {
      Jfinalcm = JRDcm ;

      Print["Sättigungsstromstärke erreicht, J=", JRDcm,
      " A/cm2"];

      $stream =
      OpenAppend["D:\\Mathematica\\transp-gate_results.txt", BinaryFormat -> True];

```

```

Export[$stream, StringJoin[ToString[NumberForm[T, ExponentFunction -> (Null &)]], "_", ToString[
  NumberForm[N[d], ExponentFunction -> (Null &)]], "_",
  ToString[NumberForm[N[E0], ExponentFunction -> (Null &)]], "_",
  ToString[Jfinalcm], "_", ToString[NumberForm[N[PhiE0/e0], ExponentFunction -> (Null &)]], "_",
  ToString[NumberForm[N[JRDCm], ExponentFunction -> (Null &)]],
  "_", ToString[NumberForm[N[VGate], ExponentFunction -> (Null &)]], "_", "na", "_", "0", "\n"
]];
(*WriteString[$stream, "\n"];*)
Close[$stream];

},
(* Wenn die Sättigungsstromstärke noch nicht erreicht ist \
(countsat =/ 1) geht es hier normal weiter *)

sol0 =
NDSolve[{Phi''[x] == -e0*n0/eps0*
  Exp[e0/(kB*T)*EGate[x]]*(Erfc[
    Re[(e0/(kB*T)*EGate[x])^(1/2)]]), Phi[0] == 0,
  Phi[d] == 0}, Phi, {x, 0, d}, MaxSteps -> Infinity];

List0 = {}; List0 = Append[List0, {0, Last[Phi[0] /. sol0]};
For[j = 1, j <= 10000, j++,
  List0 = Append[List0, {d/10000*j, Last[Phi[d/10000*j] /. sol0]};];
phitotint0 = Interpolation[List0];

maxphi0 = FindMaximum[phitotint0[x], {x, 0, 0, d}];
ymaxphi0 = maxphi0[[1]]; xmaxphi0 = x /. Last[maxphi0];

gwifaktorstart = 0.5 + qq*0.3 + vv/18;
gwifaktordone = 0.1;

creationmerk = 0;
solimerk = sol0; xmaxphimerk = xmaxphi0; ymaxphimerk = ymaxphi0;
xmaxphiold = xmaxphi0; ymaxphiold = ymaxphi0;
phitotintmerk = phitotint0;
gwifaktor = gwifaktorstart; (* Für die erste Iteration der While-
Schleife wird ein Startwert für die Gewichtung genommen,
danach wird die Gewichtung angepasst *)
DoneList = {};

n = 0; break1 = "undone"; break2 = "undone";
finalbreak = "undone"; q = 0; (*
Initialisierung der Schleifenvariablen *)

While[n < nmax,

If[n > 50,
  If[n > 100,
    If[n > 150,
      If[n > 200,
        If[n > 250,
          If[n > 300,
            If[n > 350,
              If[n > 400,
                If[n > 450, If[n > 500, speed = 0.00005, speed = 0.0001],
                  speed = 0.0005], speed = 0.001], speed = 0.002],
                speed = 0.005], speed = 0.02], speed = 0.03],
                speed = 0.05], speed = 0.1],];

soli = solimerk; xmaxpsii = xmaxpsimerk; ymaxpsii = ymaxpsimerk;
phitotinti = phitotintmerk; psitotinti = psitotintmerk;
xmaxphii = xmaxphimerk; ymaxphii = ymaxphimerk;
creation = creationmerk;

Print["gwifaktor_="_, gwifaktor, "uuuymaxpsii_=", ymaxpsii,

```

## A Appendix

```

"uuymaxphii_u", ymaxphii, "uuuuu_gwi_u", gwifaktor/ymaxphii ,
"uuuuu_speed_u", speed];

(***** erste For-Schleife *****)

break1 = "undone";

For[i = 1, i <= imax, i++,

gwi = gwifaktor/ymaxphii;

If[creation == 0,
{
Listi = {};
Listi = Append[
Listi, {0, (-gwi*Last[Phi[0] /. soli] + EGate[0])}];
For[j = 1, j <= 10000, j++,

Listi = Append[
Listi, {d/10000*
j, (-gwi*Last[Phi[d/10000*j] /. soli] +
EGate[d/10000*j])}];
psitotinti = Interpolation[Listi]; (*
Gesamtfunktion Psi aus soli und EGate erzeugen *)
\
},
{
Listi = {};
Listi = Append[
Listi, {0, (-gwi*Last[Phi[0] /. soli] + EGate[0])}];
For[j = 1, j <= 5000, j++,

Listi = Append[
Listi, {xmaxpsii/5000*
j, (-gwi*Last[Phi[xmaxpsii/5000*j] /. soli] +
EGate[xmaxpsii/5000*j])}];
For[j = 1, j <= 5000, j++,

Listi = Append[
Listi, {(xmaxpsii + (d - xmaxpsii)/5000*j), (-gwi*
Last[Phi[(xmaxpsii + (d - xmaxpsii)/5000*j] /.
soli] +
EGate[(xmaxpsii + (d - xmaxpsii)/5000*j])}];
psitotinti = Interpolation[Listi]; (*
Gesamtfunktion für Psi aus soli erzeugen -
mit Gewichtung der Raumladung Phi *)
}];

maxpsii = FindMaximum[{-psitotinti[x]}, {x, 0, 0, d/2}];
ymaxpsii = maxpsii[[1]]; xmaxpsii = x /. Last[maxpsii];
(* Bestimmung des Maximum von Phi *)

If[ymaxpsii > 1*10^(-7), difdec = 1; difdec = 0]; (* Check,
ob sich ein Maximum ausbildet; wenn ja,
schaffen es nicht mehr alle e- - einige drehen um -
und die Diffgleichung muss in zwei Bereiche aufgeteilt werden *)

(***** Numerische Lösung der Diffgleichung
*****

If[difdec == 0,
{
Print["Iteration:u", qq, "u-u", vv, "u-u", n, "u-u", i,

```

```

"#####not all through", "#####ymaxpsii=", ymaxpsii,
"#####xmaxpsii=", xmaxpsii/d, "*d", "#####ymaxphii=",
ymaxphii, "#####xmaxphii=", xmaxphii/d, "*d"];

soli = NDSolve[{

  Phi''[x] == -e0*n0/eps0*
    Exp[e0/(kB*T)*psitotinti[x]]*(Erfc[
      Re[(e0/(kB*T)*psitotinti[x])^(1/2)]]),
  Phi[0] == 0,
  Phi[d] == 0},
  Phi, {x, 0, d}, MaxSteps -> Infinity];

Listi = {};
Listi = Append[Listi, {0, Last[Phi[0] /. soli]};
For[j = 1, j <= 10000, j++,

  Listi = Append[
    Listi, {d/10000*j, Last[Phi[d/10000*j] /. soli]};];
phitotinti = Interpolation[Listi]; (*
Gesamtfunktion Phi aus soli erzeugen *)

creation = 0;

}
,
{
Print["Iteration:", qq, "-", vv, "-", n, "-", i,
"#####not all through", "#####ymaxpsii=",
ymaxpsii, "#####xmaxpsii=", xmaxpsii/d, "*d",
"#####ymaxphii=", ymaxphii, "#####xmaxphii=", xmaxphii/d,
"*d"];

soli = NDSolve[{

  Phia''[x] == -e0/eps0*n0*
    Exp[e0/(kB*T)*psitotinti[x]]*(1 +
      Erf[Re[(-e0/(kB*T)*(-ymaxpsii - psitotinti[x]))^(1/2)]]),

  Phib''[x] == -e0/eps0*n0*
    Exp[e0/(kB*T)*psitotinti[x]]*(Erfc[
      Re[(-e0/(kB*T)*(-ymaxpsii - psitotinti[x]))^(1/2)]]),
  Phia[0] == 0,
  Phib[d] == 0,
  Phia[xmaxpsii] == Phib[xmaxpsii],
  Phia'[xmaxpsii] == Phib'[xmaxpsii]},
  {Phia, Phib}, x, MaxSteps -> Infinity];

Listi = {}; Listi = Append[Listi, {0, Last[Phia[0] /. soli]};
For[j = 1, j <= 5000, j++,

  Listi = Append[
    Listi, {xmaxpsii/5000*j,
      Last[Phia[xmaxpsii/5000*j] /. soli]};];
For[j = 1, j <= 5000, j++,

  Listi = Append[
    Listi, {(xmaxpsii + (d - xmaxpsii)/5000*j),
      Last[Phib[(xmaxpsii + (d - xmaxpsii)/5000*j)] /. soli]};];
phitotinti = Interpolation[Listi]; (*
Gesamtfunktion aus soli erzeugen *)

creation = 1;

}

```

## A Appendix

```

];
(***** Ende Numerische Lösung der Diffgleichung
*****)
\

maxphii = FindMaximum[{phitotinti[x]}, {x, 0, 0, d}];
ymaxphii = maxphii[[1]]; xmaxphii = x /. Last[maxphii];
(* Bestimmung des Maximum von Phi *)

xconv = Abs[ Abs[xmaxphii/xmaxphiold - 1]];
yconv = Abs[ Abs[ ymaxphii/ymaxphiold] - 1]; (*
Berechnung der Konvergenzkriterien;
Die Konvergenz wird über die Raumladung Phi,
nicht über das Gesamtpotential Psi festgestellt *)

Print["xconv= ", xconv, " yconv= ", yconv];

If[xconv < conv1 && yconv < conv1,
{break1 = "done"; gwifaktordone = gwifaktor; Print["BREAK!!"];
solimerk = soli; xmaxpsimerk = xmaxpsii;
ymaxpsimerk = ymaxpsii; xmaxphimerk = xmaxphii;
ymaxphimerk = ymaxphii; phitotintmerk = phitotinti;
psitotintmerk = psitotinti; creationmerk = creation;
DoneList = Append[DoneList, {gwifaktor}]; Break[]}, (*
Die Variablen mit "merk" am Ende werden überschrieben,
falls die Lösung konvergiert,
damit in weiteren Rechnungen nicht mehr verändert werden \
können; außerdem wird die Variable gwifaktordone auf den Wert \
gwifaktor gesetzt,
bei dem gerade die Lösung konvergiert ist *)
\
{xmaxphiold = xmaxphii; ymaxphiold = ymaxphii; break1 = "undone"}]; (*
Abbruchsbedingung - Check der Konvergenzkriterien *)
]

Print["break1= ", break1, "\n"];
(***** erste For-Schleife zu Ende *****)

If[break1 == "done",
{gwifaktorneu = ((1 - speed)*gwifaktor + speed* ymaxphii);
If[Abs[gwifaktorneu - gwifaktor] > 0.03,
gwifaktorneu =
gwifaktor + Sign[gwifaktorneu - gwifaktor]*0.03,];
gwifaktor = gwifaktorneu;
q = 0},
{gwifaktor = (gwifaktordone + gwifaktor)/2; q = q + 1;});

If[q == 5, {Print["EMERGENCY_OSCI!!"];
gwifaktordone1 = gwifaktordone1*0.9; q = 0,};

If [Abs[(gwifaktor /ymaxphii - 1)] < conv2, break2 = "done",
break2 = "undone"];

Print["DoneList= ", DoneList];
Print["break2= ", break2];

Print["|1-gwifaktor_/ymaxphii|= ",
Abs[(gwifaktor /ymaxphii - 1)]];

n++;

Print["\n\n"];

```

```

endtime = TimeUsed[];
etime = endtime - starttime;

Print["elapsed_time:␣", etime, "s"];

If [ break1 == "done" && break2 == "done",
{
  (***** Berechnung von psitotinti *****)

  If[creation == 0,
  {
    Listi = {};
    Listi = Append[
      Listi, {0, (-gwi*Last[Phi[0] /. soli] + EGate[0])}];
    For[j = 1, j <= 10000, j++,

      Listi = Append[
        Listi, {d/10000*
          j, (-gwi*Last[Phi[d/10000*j] /. soli] +
            EGate[d/10000*j])}];
      psitotinti = Interpolation[Listi]; (*
        Gesamtfunktion Psi aus soli und EGate erzeugen *)
      \
    },
    {
      Listi = {};
      Listi = Append[
        Listi, {0, (-gwi*Last[Phia[0] /. soli] + EGate[0])}];
      For[j = 1, j <= 5000, j++,

        Listi = Append[
          Listi, {xmaxpsii/5000*
            j, (-gwi*Last[Phia[xmaxpsii/5000*j] /. soli] +
              EGate[xmaxpsii/5000*j])}];
        For[j = 1, j <= 5000, j++,

          Listi = Append[
            Listi, {(xmaxpsii + (d - xmaxpsii)/5000*j), (-gwi*
              Last[Phib[(xmaxpsii + (d - xmaxpsii)/5000*j] /.
                soli] +
                EGate[(xmaxpsii + (d - xmaxpsii)/5000*j])}]}];
            psitotinti = Interpolation[Listi]; (*
              Gesamtfunktion für Psi aus soli erzeugen -
              mit Gewichtung der Raumladung Phi *)
            }];

      maxpsii = FindMaximum[{-psitotinti[x]}, {x, 0, 0, d/2}];
      ymaxpsii = maxpsii[[1]]; xmaxpsii = x /. Last[maxpsii];
      (* Bestimmung des Maximum von Psi *)

      If[ymaxpsii > 1*10-7, difdec = 1;, difdec = 0];

      (***** psitotinti muss noch ein mal berechnet werden,
        da es immer vor jedem Iterationsschritt berechnet wird,
        aber nicht mehr danach.
        Hier also die "finale Version" *****)

      Jfinalcm = JRDcm *Exp[-e0*yamaxpsii/(kB*T)];
      If[Abs[Jfinalcm - JRDcm] < 1*10-5, countsat = 1,];

      (***** Plots - Beginning *****)

      text1 =

```

```

StringJoin["d_=", ToString[N[d*1000]], "_mm", "UUUEGate_=",
ToString[N[EO/1000]], "_*10^3_V/m_n", "PhiE_=",
ToString[N[PhiEO/e0]], "_eV", "UUUT_=", ToString[T],
"K_n", "JRD_=", ToString[N[JRDcm, 3]], "_A_/cm^.b2", "\n",
"J_=", ToString[Jfinalcm], "_A_/cm^.b2"];

Plotfinalphi =
Plot[phitotinti[x], {x, 0, d},
PlotRange -> {{0, d}, {0, 1.2*ymaxphii}},
Axes -> {True, False}, AxesOrigin -> {0, 0},
PlotStyle -> Thick,
Epilog ->
Inset[Framed[Text[Style[text1, 14]], Background -> White],
ImageScaled[ {.4, .3}]], ImageSize -> 500, Frame -> True,
FrameLabel -> {Style["distance", 20],
Style["space_charge", 20]}, LabelStyle -> {FontSize -> 14}];
filenamephi =
StringJoin["D:\\Mathematica_Plots\\transparent-gate_phi_d-",
ToString[N[d*1000]], "_V-",
ToString[NumberForm[N[VGate], ExponentFunction -> (Null &)]],
"_E-",
ToString[NumberForm[N[EO], ExponentFunction -> (Null &)]],
"_PhiE-", ToString[N[PhiEO/e0]], "_T-", ToString[T],
".pdf"];
Export[filenamephi, Plotfinalphi];

Plotfinalpsi =
Plot[-psitotinti[x], {x, 0, d},
PlotRange -> {{0, d}, {-VGate, 1.5*ymaxpsii}},
Axes -> {True, False}, AxesOrigin -> {0, 0},
PlotStyle -> Thick,
Epilog ->
Inset[Framed[Text[Style[text1, 14]], Background -> White],
ImageScaled[ {.75, .3}]], ImageSize -> 500, Frame -> True,
FrameLabel -> {Style["distance", 20],
Style["space_charge", 20]}, LabelStyle -> {FontSize -> 14}];
filenamepsi =
StringJoin["D:\\Mathematica_Plots\\transparent-gate_psi_d-",
ToString[N[d*1000]], "_V-",
ToString[NumberForm[N[VGate], ExponentFunction -> (Null &)]],
"_E-", ToString[
NumberForm[N[EO], ExponentFunction -> (Null &)]], "_PhiE-",
ToString[N[PhiEO/e0]], "_T-", ToString[T], ".pdf"];
Export[filenamepsi, Plotfinalpsi];

sctota[x_] :=
e0*n0*Exp[
e0/(kB*T)*psitotinti[x]*(1 +
Erf[Re[(-e0/(kB*T)*(-ymaxpsii - psitotinti[x]))^(1/2)]]);
sctotb[x_] :=
e0*n0*Exp[
e0*psitotinti[x]/(kB*T)*(Erfc[
Re[(-e0/(kB*T)*(-ymaxpsii - psitotinti[x]))^(1/2)]]);

If[difdec == 0,
{
plotsctotb =
Plot[sctotb[x], {x, 0, d}, PlotStyle -> {Thick, Blue},
PlotRange -> {{0, d}, {0, 1}}, Axes -> {True, False},
AxesOrigin -> {0, 0}, PlotStyle -> Thick, ImageSize -> 500,
Frame -> True,
FrameLabel -> {Style["distance_/m", 20],
Style["charge_density_/C_/m^3", 20]},

```

```

LabelStyle -> {FontSize -> 14},
Epilog ->
  Inset[Framed[Text[Style[text1, 14]], Background -> White],
    ImageScaled[ {.7, .8} ]];
Plotsctot = Show[plotsctotb];
},
{
plotsctota =
Plot[sctota[x], {x, 0, xmaxpsii},
PlotStyle -> {Thick, Blue}, PlotRange -> {{0, d}, {0, 1}},
Axes -> {True, False}, AxesOrigin -> {0, 0},
PlotStyle -> Thick, ImageSize -> 500, Frame -> True,
FrameLabel -> {Style["distance⊥/μm", 20],
  Style["charge⊥density⊥/C⊥/μm3", 20]},
LabelStyle -> {FontSize -> 14},
Epilog ->
  Inset[Framed[Text[Style[text1, 14]], Background -> White],
    ImageScaled[ {.7, .8} ]];
plotsctotb =
Plot[sctotb[x], {x, xmaxpsii, d},
PlotStyle -> {Thick, Blue}, PlotRange -> {{0, d}, {0, 1}},
Axes -> {True, False}, AxesOrigin -> {0, 0},
PlotStyle -> Thick, ImageSize -> 500, Frame -> True,
FrameLabel -> {Style["distance⊥/μm", 20],
  Style["charge⊥density⊥/C⊥/μm3", 20]},
LabelStyle -> {FontSize -> 14},
Epilog ->
  Inset[Framed[Text[Style[text1, 14]], Background -> White],
    ImageScaled[ {.7, .8} ]];
Plotsctot = Show[plotsctota, plotsctotb];
}];

filenamesc =
StringJoin["D:\\Mathematica_Plots\\transparent-gate_sc_d-",
ToString[N[d*1000]], "_V-",
ToString[NumberForm[N[VGate], ExponentFunction -> (Null &)]],
"_E-",
ToString[NumberForm[N[E0], ExponentFunction -> (Null &)]],
"_PhiE-", ToString[N[PhiE0/e0]], "_T-", ToString[T],
".pdf"];
Export[filenamesc, Plotsctot];

sctotthrough[x_] :=
2*e0*n0*Exp[e0*psitotinti[x]/(kB*T)]*
Erf[Re[(-e0/(kB*T))*(-ymaxpsii - psitotinti[x])^(1/2)]];
sctthrough[x_] :=
e0*n0*Exp[
e0*psitotinti[x]/(kB*T)]*(Erfc[
Re[(-e0/(kB*T))*(-ymaxpsii - psitotinti[x])^(1/2)]]);

If[difdec == 0,
{
plotsctthrough =
Plot[sctthrough[x], {x, 0, d}, PlotStyle -> {Thick, Green},
PlotRange -> {{0, d}, {0, 1}}, Axes -> {True, False},
AxesOrigin -> {0, 0}, PlotStyle -> Thick, ImageSize -> 500,
Frame -> True,
FrameLabel -> {Style["distance⊥/μm", 20],
  Style["charge⊥density⊥/C⊥/μm3", 20]},
LabelStyle -> {FontSize -> 14},
Epilog ->
  Inset[Framed[Text[Style[text1, 14]], Background -> White],
    ImageScaled[ {.7, .8} ]];
Plotallsc = Show[plotsctotb, plotsctthrough];
},
{

```

```

plotsctnotthrough =
Plot[sctnotthrough[x], {x, 0, xmaxpsii},
PlotStyle -> {Thick, Red}, PlotRange -> {{0, d}, {0, 1}},
Axes -> {True, False}, AxesOrigin -> {0, 0},
PlotStyle -> Thick, ImageSize -> 500, Frame -> True,
FrameLabel -> {Style["distance_/_μm", 20],
Style["charge_density_/_C_/_μm^3", 20]},
LabelStyle -> {FontSize -> 14},
Epilog ->
Inset[Framed[Text[Style[text1, 14]], Background -> White],
ImageScaled[ {.7, .8} ]];
plotsctthrough =
Plot[sctthrough[x], {x, 0, d}, PlotStyle -> {Thick, Green},
PlotRange -> {{0, d}, {0, 1}}, Axes -> {True, False},
AxesOrigin -> {0, 0}, PlotStyle -> Thick, ImageSize -> 500,
Frame -> True,
FrameLabel -> {Style["distance_/_μm", 20],
Style["charge_density_/_C_/_μm^3", 20]},
LabelStyle -> {FontSize -> 14},
Epilog ->
Inset[Framed[Text[Style[text1, 14]], Background -> White],
ImageScaled[ {.7, .8} ]];
Plotallsc =
Show[plotsctota, plotsctotb, plotsctnotthrough,
plotsctthrough];
];

filenameesc =
StringJoin[
"D:\Mathematica_Plots\transparent-gate_sc-all_d-",
ToString[N[d*1000]], "_V-",
ToString[NumberForm[N[VGate], ExponentFunction -> (Null &)]],
"_E-", ToString[
NumberForm[N[E0], ExponentFunction -> (Null &)]], "_PhiE-",
ToString[N[PhiE0/e0]], "_T-", ToString[T], ".pdf"];
Export[filenameesc, Plotallsc];

(**** Plots End ****)

(**** Creating data files for the plots - Beginning ****)

filenamedatpotentialsall =
StringJoin[
"D:\Mathematica\data_files\potentials_all_data-",
ToString[N[d*1000]], "_E-",
ToString[NumberForm[N[E0], ExponentFunction -> (Null &)]],
"_PhiE-", ToString[N[PhiE0/e0]], "_T-", ToString[T],
".txt"];
$stream =
OpenWrite[filenamedatpotentialsall, BinaryFormat -> True];
Export[$stream, StringJoin["#_x[m]_phi[eV]_psi[eV]", "\n"]];
(*Close[$stream];

$stream=OpenAppend[filenamedatpotentialsall,BinaryFormat->
True];*)
For[i = 0, i <= 1000, i++,
(*$stream=OpenAppend[filenamedatascall,BinaryFormat->True]; *)

Export[$stream,
StringJoin[
ToString[
NumberForm[N[d/1000*i], ExponentFunction -> (Null &)]],
"_", ToString[
NumberForm[N[phitotinti[d/1000*i]],

```

```

    ExponentFunction -> (Null &)]], "\u",
    ToString[
    NumberForm[N[psitotinti[d/1000*i]],
    ExponentFunction -> (Null &)]], "\n"];
(*Close[$stream]*);

];
Close[$stream];

filenamedatascall =
StringJoin["D:\\Mathematica\\data_files\\sc_all_data_",
ToString[N[d*1000]], "_E-",
ToString[NumberForm[N[E0], ExponentFunction -> (Null &)]],
"_PhiE-", ToString[N[PhiE0/e0]], "_T-", ToString[T],
".txt"];
$stream = OpenWrite[filenamedatascall, BinaryFormat -> True];
Export[$stream,
StringJoin[
"#x[m]\u\scttotal[C/m^3]\u\sctnotthrough[C/m^3]\u\sctthrough[C/m^3]",
"\n"];
Close[$stream];

$stream = OpenAppend[filenamedatascall, BinaryFormat -> True];
For[i = 0, i <= 1000, i++,
If[d/1000*i < xmaxpsii,
{(*$stream=OpenAppend[filenamedatascall,BinaryFormat->
True]; *)

Export[$stream,
StringJoin[
ToString[
NumberForm[N[d/1000*i], ExponentFunction -> (Null &)]],
"\u", ToString[
NumberForm[N[sctota[d/1000*i]],
ExponentFunction -> (Null &)]], "\u",
ToString[
NumberForm[N[sctnotthrough[d/1000*i]],
ExponentFunction -> (Null &)]], "\u",
ToString[
NumberForm[N[sctthrough[d/1000*i]],
ExponentFunction -> (Null &)]], "\n"];
(*Close[$stream]*);
},
{
(*$stream=OpenAppend[filenamedatascall,BinaryFormat->
True]; *)

Export[$stream,
StringJoin[
ToString[
NumberForm[N[d/1000*i], ExponentFunction -> (Null &)]],
"\u", ToString[

NumberForm[N[sctotb[d/1000*i]],
ExponentFunction -> (Null &)]], "\u",
ToString[NumberForm[N[0], ExponentFunction -> (Null &)]],
"\u", ToString[
NumberForm[N[sctthrough[d/1000*i]],
ExponentFunction -> (Null &)]], "\n"];
(*Close[$stream];*)
}}
];
Close[$stream];
(**** Creating data files for the plots - End ****)

```

## A Appendix

```
(**** Output in Mathematica - Beginning *****)

Print[Show[Plotfinalphi, ImageSize -> 1000]];
Print[Show[Plotfinalpsi, ImageSize -> 1000]];
Print[Show[Plotsctot, ImageSize -> 1000]];
Print[Show[Plotallsc, ImageSize -> 1000]];

Print["saturation_current:␣", JRDcm, "␣A␣/␣cm^2"];
Print["space_charge_limited_current:␣", Jfinalcm, "␣A␣/␣cm^2"];
Print["current_without_thermal_distribution:␣",
  1/10^4*1/Sqrt[6]*Sqrt[e0/me]*eps0*(E0)^(3/2)/(d/2)^(1/2),
  "␣A␣/␣cm^2"];

(**** Output in Mathematica - End *****)

(**** Data for file - Beginning *****)

$stream =
  OpenAppend["D:\\Mathematica\\transp-gate_results.txt",
    BinaryFormat -> True];
Export[$stream,
  StringJoin[
    ToString[NumberForm[T, ExponentFunction -> (Null &)]], "␣",
    ToString[NumberForm[N[d], ExponentFunction -> (Null &)]],
    "␣", ToString[
      NumberForm[N[E0], ExponentFunction -> (Null &)]], "␣",
    ToString[Jfinalcm], "␣",
    ToString[
      NumberForm[N[PhiE0/e0], ExponentFunction -> (Null &)]], "␣",
    ToString[
      NumberForm[N[JRDcm], ExponentFunction -> (Null &)]], "␣",
    ToString[NumberForm[N[VGate], ExponentFunction -> (Null &)]],
    "␣", ToString[
      NumberForm[N[ymaxphii], ExponentFunction -> (Null &)]], "␣",
    ToString[
      NumberForm[N[ymaxpsii], ExponentFunction -> (Null &)]],
    "\\n"];
Close[$stream];
(**** Data for file - End *****)

endtime = TimeUsed[];
etime = endtime - starttime;

Print["elapsed_time:␣", etime, "s"];
Break[];

},];
];

] (* Klammer für die If-Schleife mit countsat *)

]; (* Ende For-Schleife vv *)

endtime = TimeUsed[];
etime = endtime - starttime;

Print["elapsed_time:␣", etime, "s"];

]; (* Ende For-Schleife qq *)
```

# Bibliography

- [1] *Key World Energy Statistics 2012*. Technical report, International Energy Agency (2012).
- [2] R. KNEER (2012). RWTH Aachen, private communication with Jochen Mannhart.
- [3] S. MEIR. *Highly-efficient conversion of heat and solar radiation into electricity*. Ph.D. thesis, Universität Augsburg (2012).
- [4] B. Y. MOYZHES and T. H. GEBALLE. *The thermionic energy converter as a topping cycle for more efficient heat engines—new triode designs with a longitudinal magnetic field*. *Journal of Physics D: Applied Physics* **38**, 782–786 (2005). doi:10.1088/0022-3727/38/5/017.
- [5] NATIONAL RESEARCH COUNCIL. COMMITTEE ON THERMIONIC RESEARCH AND TECHNOLOGY. *Thermionics Quo Vadis? An Assessment of the DTRA's Advanced Thermionics Research and Development Program*. National Academy Press, Washington D.C. (2001). ISBN 030908282X.
- [6] G. N. HATSOPOULOS and E. P. GYFTOPOULOS. *Thermionic Energy Conversion Volume I: Processes and Devices*. MIT Press, Cambridge and London (1973). ISBN 0262080591.
- [7] W. SCHLICHTER. *Die spontane Elektronenemission glühender Metalle und das glühelektrische Element*. *Annalen der Physik* **47**, 573–640 (1915). doi:10.1002/andp.19153521302.
- [8] N. N. PONOMAREV-STEPNOI, V. M. TALYZIN and V. A. USOV. *Russian space nuclear power and nuclear thermal propulsion systems*. *Nuclear News* **43**, 33–46 (2000).
- [9] J. W. SCHWEDE, I. BARGATIN, D. C. RILEY, B. E. HARDIN, S. J. ROSENTHAL, Y. SUN, F. SCHMITT, P. PIANETTA, R. T. HOWE, Z. SHEN and N. A. MELOSH. *Photon-enhanced thermionic emission for solar concentrator systems*. *Nature Materials* **9**, 762–767 (2010). doi:10.1038/nmat2814.
- [10] G. D. MAHAN. *Thermionic refrigeration*. *Journal of Applied Physics* **76**, 4362–4366 (1994). doi:10.1063/1.357324.
- [11] Y. DENG and J. LIU. *Recent advances in direct solar thermal power generation*. *Journal of Renewable and Sustainable Energy* **1** (2009). doi:10.1063/1.3212675.

## Bibliography

- [12] P. G. TANNER, D. A. FRASER and A. D. IRVING. *Developments in thermionic energy converters*. IEE Proceedings - Science, Measurement and Technology **152**, 1–6 (2005). doi:10.1049/ip-smt:20051050.
- [13] G. FITZPATRICK, E. BRITT and B. MOYZHES. *Updated perspective on the potential for thermionic conversion to meet 21st Century energy needs*. In *Energy Conversion Engineering Conference, 1997.*, pages 1045 –1051 vol.2 (1997). doi:10.1109/IECEC.1997.661913.
- [14] J. R. LUKE. *Results from the advanced thermionic technology program*. In *Energy Conversion Engineering Conference, 2002.*, pages 565– 570. IEEE (2004). ISBN 0-7803-7296-4. doi:10.1109/IECEC.2002.1392107.
- [15] H. MÜLLER-STEINHAGEN and F. TRIEB. *Concentrating solar power*. *Ingenia* pages 43–50 (2004).
- [16] V. S. FOMENKO. *Handbook of Thermionic Properties*. Plenum Press, New York (1966). ISBN 0306651173.
- [17] G. N. HATSOPOULOS and J. KAYE. *Measured thermal efficiencies of a diode configuration of a thermo electron engine*. *Journal of Applied Physics* **29**, 1124–1125 (1958). doi:10.1063/1.1723373.
- [18] G. FITZPATRICK, J. KOESTER, J. CHANG, E. BRITT and J. McVEY. *Close-spaced thermionic converters with active spacing control and heat-pipe isothermal emitters*. In *Energy Conversion Engineering Conference, 1996.*, volume 2, pages 920 –927 vol.2 (1996). doi:10.1109/IECEC.1996.553821.
- [19] D. B. KING, K. R. ZAVADIL, D. R. JENNISON, C. C. BATTAILE and A. C. MARSHALL. *Low work function material development for the microminiature thermionic converter*. Technical report, Sandia National Laboratories, Albuquerque and Livermore (2004).
- [20] J. LEE, I. BARGATIN, N. A. MELOSH and R. T. HOWE. *Optimal emitter-collector gap for thermionic energy converters*. *Applied Physics Letters* **100**, 173904 1–4 (2012). doi:10.1063/1.4707379.
- [21] Y. HISHINUMA, T. H. GEBALLE, B. Y. MOYZHES and T. W. KENNY. *Refrigeration by combined tunneling and thermionic emission in vacuum: Use of nanometer scale design*. *Applied Physics Letters* **78**, 2572–2574 (2001). doi:10.1063/1.1365944.
- [22] Y. C. GERSTENMAIER and G. WACHUTKA. *Efficiency of Thermionic and Thermoelectric Converters*. *AIP Conference Proceedings* **890**, 349–360 (2007). doi: 10.1063/1.2711752.
- [23] N. RASOR. *Emission physics of the thermionic energy converter*. *Proceedings of the IEEE* **51**, 733–747 (1963). doi:10.1109/PROC.1963.2266.

- [24] N. S. RASOR. *Thermionic energy-conversion plasmas*. IEEE Transactions on Plasma Science **19**, 1191–1208 (1991).
- [25] N. W. ASHCROFT and N. D. MERMIN. *Festkörperphysik*. Oldenbourg (2001). ISBN 3486248340.
- [26] N. D. LANG and W. KOHN. *Theory of metal surfaces - work function*. Physical Review B **3**, 1215–1223 (1971).
- [27] D. R. LIDE, editor. *CRC Handbook of Chemistry and Physics*. CRC Press, Boca Raton, 80 edition (1999). ISBN 0849304806.
- [28] R. FORMAN. *Surface studies of barium and barium oxide on tungsten and its application to understanding the mechanism of operation of an impregnated tungsten cathode*. Journal of Applied Physics **47**, 5272–5279 (1976). doi:10.1063/1.322602.
- [29] G. N. HATSOPOULOS and E. P. GYFTOPOULOS. *Thermionic Energy Conversion Volume II: Theory, Technology and Application*. MIT Press, Cambridge and London (1979). ISBN 0262080591.
- [30] M. NONNENMACHER, M. P. O'BOYLE and H. K. WICKRAMASINGHE. *Kelvin probe force microscopy*. Applied Physics Letters **58**, 2921–2923 (1991). doi:10.1063/1.105227.
- [31] O. W. RICHARDSON. *The Emission of Electricity from Hot Bodies*. Longmans, Green and Co., London (1916).
- [32] S. DUSHMAN. *Electron emission from metals as a function of temperature*. Physical Review **21**, 623–636 (1923). doi:10.1103/PhysRev.21.623.
- [33] A. C. MARSHALL. *A reformulation of thermionic theory for vacuum diodes*. Surface Science **517**, 186–206 (2002). doi:10.1016/S0039-6028(02)02063-0.
- [34] C. D. CHILD. *Discharge from hot CaO*. Physical Review (Series I) **32**, 492–511 (1911). doi:10.1103/PhysRevSeriesI.32.492.
- [35] I. LANGMUIR. *The effect of space charge and residual gases on thermionic currents in high vacuum*. Physical Review **2**, 450–486 (1913). doi:10.1103/PhysRev.2.450.
- [36] W. SCHOTTKY. *Über kalte und warme Elektronenentladungen*. Zeitschrift für Physik A **14**, 63–106 (1923). doi:10.1007/BF01340034.
- [37] R. H. FOWLER and L. NORDHEIM. *Electron emission in intense electric fields*. Proceedings of the Royal Society of London A **119**, 173–181 (1928).
- [38] G. P. SMESTAD. *Conversion of heat and light simultaneously using a vacuum photodiode and the thermionic and photoelectric effects*. Solar Energy Materials and Solar Cells **82**, 227–240 (2004). doi:10.1016/j.solmat.2004.01.020.

## Bibliography

- [39] A. EINSTEIN. *Über einen die Erzeugung und Verwandlung des Lichtes betreffenden heuristischen Gesichtspunkt*. *Annalen der Physik* **322**, 132–148 (1905). doi:10.1002/andp.19053220607.
- [40] J. H. INGOLD. *Calculation of the maximum efficiency of the thermionic converter*. *Journal of Applied Physics* **32**, 769–772 (1961). doi:10.1063/1.1736103.
- [41] J. M. HOUSTON. *Theoretical Efficiency of the Thermionic Energy Converter*. *Journal of Applied Physics* **30**, 481–487 (1959). doi:10.1063/1.1702392.
- [42] N. S. RASOR. *Figure of Merit for Thermionic Energy Conversion*. *Journal of Applied Physics* **31**, 163–167 (1960). doi:10.1063/1.1735392.
- [43] A. SCHOCK. *Optimization of Emission Limited Thermionic Generators*. *Journal of Applied Physics* **32**, 1564–1570 (1961). doi:10.1063/1.1728397.
- [44] F. G. BAKSHT, G. A. DYVZHEV, A. M. MARTSINOVSKIY, B. Y. MOYZHES, G. Y. DIKUS, E. B. SONIN and V. G. YURYEV. *Thermionic converters and low-temperature plasma*. NASA STI/Recon Technical Report N **80**, 17579 (1978).
- [45] C. RICHTER, editor. *SolarPACES Annual Report 2008*. International Energy Agency (2009). Available from [www.solarpaces-csp.org/Library/AnnualReports](http://www.solarpaces-csp.org/Library/AnnualReports).
- [46] C. RICHTER, editor. *SolarPACES Annual Report 2009*. International Energy Agency (2010). Available from [www.solarpaces-csp.org/Library/AnnualReports](http://www.solarpaces-csp.org/Library/AnnualReports).
- [47] W. B. STINE and R. B. DIVER. *A Compendium of Solar Dish/Stirling Technology*. Technical report, Sandia National Laboratories, Albuquerque and Livermore (1994).
- [48] A. F. IOFFE. *Semiconductor Thermoelements and Thermoelectric Cooling*. Infosearch Ltd. London, London (1957).
- [49] G. J. SNYDER and E. S. TOBERER. *Complex thermoelectric materials*. *Nature Materials* **7**, 105–114 (2008). doi:10.1038/nmat2090.
- [50] A. V. DA ROSA. *Fundamentals of renewable energy processes*. Elsevier Academic Press, Amsterdam; Boston (2009). ISBN 9780123746399.
- [51] T. M. TRITT and M. A. SUBRAMANIAN. *Thermoelectric materials, phenomena, and applications: a bird's eye view*. *MRS Bulletin* **31**, 188–198 (2006). doi:10.1557/mrs2006.44.
- [52] C. B. VINING. *An inconvenient truth about thermoelectrics*. *Nature Materials* **8**, 83–85 (2009). doi:10.1038/nmat2361.
- [53] W. H. PREECE. *On a peculiar behaviour of glow-lamps when raised to high incandescence*. *Proceedings of the Royal Society of London* **38**, 219–230 (1884). doi:10.1098/rspl.1884.0093.

- [54] O. W. RICHARDSON. *On the negative radiation from hot platinum*. Proceedings of the Cambridge Philosophical Society pages 286–295 (1901).
- [55] O. W. RICHARDSON. *Some applications of the electron theory of matter*. Philosophical Magazine Series 6 **23**, 594 (1912). doi:10.1080/14786440408637250.
- [56] O. W. RICHARDSON. *The Emission of Electrons from Tungsten at High Temperatures: An Experimental Proof That the Electric Current in Metals Is Carried by Electrons*. Science **38**, 57–61 (1913). doi:10.1126/science.38.967.57.
- [57] L. L. MARTON. *Advances in Electronics and Electron Physics*. Academic Press (1963). ISBN 9780120145171.
- [58] M. R. CHAMPEIX. *Considerations of the Transformation of Heat into Electrical Energy in Thermionic Phenomena*. Vide **6**, 936 (1951).
- [59] G. N. HATSOPOULOS. *The Thermo-Electron Engine*. PhD thesis, Massachusetts Institute of Technology (1956).
- [60] H. MOSS. *Thermionic diodes as energy converters*. Journal of Electronics and Control **2**, 305–322 (1957). doi:10.1080/00207215708937036.
- [61] K. G. HERNQVIST, M. KANEFSKY and F. H. NORMAN. *Thermionic energy converter*. RCA Review **19**, 244–258 (1958).
- [62] G. N. HATSOPOULOS and J. KAYE. *Analysis and experimental results of a diode configuration of a novel thermoelectron engine*. Proceedings of the IRE **46**, 1574–1579 (1958). doi:10.1109/JRPROC.1958.286932.
- [63] G. M. GROVER, D. J. ROEHLING, E. W. SALMI and R. W. PIDD. *Properties of a thermoelectric cell*. Journal of Applied Physics **29**, 1611–1612 (1958). doi:10.1063/1.1723009.
- [64] W. B. NOTTINGHAM. *Thermionic diode as a heat-to-electrical-power transducer*. Journal of Applied Physics **30**, 413–417 (1959). doi:10.1063/1.1735178.
- [65] H. F. WEBSTER. *Calculation of the performance of a high-vacuum thermionic energy converter*. Journal of Applied Physics **30**, 488–492 (1959). doi:10.1063/1.1702393.
- [66] V. C. WILSON. *Conversion of heat to electricity by thermionic emission*. Journal of Applied Physics **30**, 475–481 (1959). doi:10.1063/1.1702391.
- [67] J. KAYE. *Direct conversion of heat to electricity*. Wiley, New York [u.a.] (1960).
- [68] P. A. LINDSAY and F. W. PARKER. *Potential distribution between two plane emitting electrodes II. thermionic engines*. Journal of Electronics and Control **9**, 81–111 (1960). doi:10.1080/00207216008962752.

## Bibliography

- [69] E. S. RITTNER. *On the theory of the close-spaced impregnated cathode thermionic converter*. Journal of Applied Physics **31**, 1065–1071 (1960). doi:10.1063/1.1735747.
- [70] G. HATSOPOULOS, J. KAYE and E. LANGBERG. *Prediction of optimum performance of vacuum-diode configuration of thermionic engines*. IRE Transactions on Electron Devices **7**, 117–122 (1960). doi:10.1109/T-ED.1960.14666.
- [71] A. F. DUGAN. *Contribution of anode emission to space charge in thermionic power converters*. Journal of Applied Physics **31**, 1397–1400 (1960). doi:10.1063/1.1735850.
- [72] D. GABOR. *A New Thermionic Generator*. Nature **189**, 868–872 (1961). doi:10.1038/189868a0.
- [73] M. A. CAYLESS. *Thermionic generation of electricity*. British Journal of Applied Physics **12**, 433–442 (1961). doi:10.1088/0508-3443/12/9/303.
- [74] B. DEVIN and M. VANDEVYVER. *Maximum theoretical efficiency of thermoelectronic emission energy converters*. Journal de Physique Appliquée **23**, 18 (1962).
- [75] N. S. RASOR and C. C. WEEKS. *Thermionic converters for compact nuclear power plants*. Atomics International (1962).
- [76] M. ZGORZELSKI. *Optimization of the Magnetic Triode-Type Thermionic Converter*. Journal of Applied Physics **35**, 197 (1964). doi:10.1063/1.1713067.
- [77] G. N. HATSOPOULOS. *Conversion of Thermal Energy into Electrical Energy* (1959). U.S. Classification: 310/306.
- [78] R. ENGDAHL, A. CASSANO and R. DOWDELL. *Thermionics in Fossil-Fuel and Nuclear Central Power Stations*. Combustion **41**, 24–& (1970).
- [79] D. M. ALLEN, R. J. PINKERTON and T. MAHEFKY. *A summary of the National Research Council's report on thermionics*. In *Energy Conversion Engineering Conference, 2002.*, pages 571–576. IEEE (2004). doi:10.1109/IECEC.2002.1392108.
- [80] M. TARASENKO. *Twinkle, twinkle little topaz*. Bulletin of the Atomic Scientists **49**, 11–13 (1993).
- [81] S. F. ADAMS. *Solar thermionic space power technology testing: a historical perspective*. AIP Conference Proceedings **813**, 590–597 (2006). doi:doi:10.1063/1.2169239.
- [82] P. N. CLARK, J. DESPLAT, H. H. STRECKERT, S. F. ADAMS and J. W. SMITH. *Solar thermionic test in a thermal receiver*. AIP Conference Proceedings **813**, 598–606 (2006). doi:10.1063/1.2169240.

- [83] M. R. MARTINEZ, O. IZHVANOV, B. ROBERTSON, P. N. CLARK, H. H. STRECKERT and J. DESPLAT. *Cylindrical inverted multi-cell (CIM) thermionic converter for solar power and propulsion systems*. AIP Conference Proceedings **746**, 926–934 (2005). doi:10.1063/1.1867217.
- [84] Y. HISHINUMA, B. Y. MOYZHES, T. H. GEBALLE and T. W. KENNY. *Vacuum thermionic refrigeration with a semiconductor heterojunction structure*. Applied Physics Letters **81**, 4242–4244 (2002). doi:10.1063/1.1523653.
- [85] J. R. SMITH, G. L. BILBRO and R. J. NEMANICH. *Theory of space charge limited regime of thermionic energy converter with negative electron affinity emitter*. Journal of Vacuum Science & Technology B: Microelectronics and Nanometer Structures **27**, 1132–1141 (2009). doi:10.1116/1.3125282.
- [86] A. N. TAVKHELIDZE. *Nanostructured electrodes for thermionic and thermotunnel devices*. Journal of Applied Physics **108**, 044313 1–7 (2010). doi:10.1063/1.3464256.
- [87] T. ZENG. *Thermionic-tunneling multilayer nanostructures for power generation*. Applied Physics Letters **88**, 153104 1–3 (2006). doi:10.1063/1.2192973.
- [88] C. ZHANG, K. NAJAFI, L. BERNAL and P. WASHABAUGH. *Micro combustion-thermionic power generation: feasibility, design and initial results*. In *12th International Conference on Transducers, Solid-State Sensors, Actuators and Microsystems*, volume 1, pages 40–44 (2003). doi:10.1109/SENSOR.2003.1215248.
- [89] J. H. LEE, I. BARGATIN, T. O. GWINN, M. VINCENT, K. A. LITTAU, R. MABOUDIAN, Z. SHEN, N. A. MELOSH and R. T. HOWE. *Microfabricated silicon carbide thermionic energy converter for solar electricity generation*. In *IEEE 25th International Conference on Micro Electro Mechanical Systems*, pages 1261 –1264 (2012). doi:10.1109/MEMSYS.2012.6170386.
- [90] G. WACHUTKA and Y. GERSTENMAIER. *Thermoelectric and thermionic microgenerators: chances, challenges and limitations*. In *Mixed Design of Integrated Circuits and System, 2006.*, pages 48–51. IEEE (2006). ISBN 83-922632-2-7. doi: 10.1109/MIXDES.2006.1706534.
- [91] Y. HISHINUMA, T. H. GEBALLE, B. Y. MOYZHES and T. W. KENNY. *Measurements of cooling by room-temperature thermionic emission across a nanometer gap*. Journal of Applied Physics **94**, 4690–4696 (2003). doi:10.1063/1.1606852.
- [92] X. C. XUAN. *Combined thermionic-thermoelectric refrigerator*. Journal of Applied Physics **92**, 4746–4750 (2002). doi:10.1063/1.1509101.
- [93] L. CHEN, Z. DING and F. SUN. *Performance analysis of a vacuum thermionic refrigerator with external heat transfer*. Journal of Applied Physics **107**, 104507 1–7 (2010). doi:10.1063/1.3428419.

## Bibliography

- [94] H. T. CHUA, X. WANG and J. M. GORDON. *Thermionic and tunneling cooling thermodynamics*. Applied Physics Letters **84**, 3999–4001 (2004). doi:10.1063/1.1738939.
- [95] R. L. LAING. *Thermionic Converter* (1969). U.S. Classification: 322/2.00R.
- [96] J. D. JACKSON. *Classical Electrodynamics*. Wiley, 3 edition (1998). ISBN 047130932X.
- [97] T. C. HALES. *The honeycomb conjecture*. Discrete and Computational Geometry **25**, 1–22 (2001). doi:10.1007/s004540010071.
- [98] A. ROTH. *Vacuum Technology*. Elsevier Science Publishers, Amsterdam, 3 edition (1990). ISBN 0444860274.
- [99] INTEGRATED ENGINEERING SOFTWARE. *IES*. (2011). COULOMB, AMPERES, and LORENTZ, version 9.0, [www.integratedsoft.com](http://www.integratedsoft.com).
- [100] J. T. KATSIKADELIS. *Boundary Elements: Theory and Applications*. Elsevier (2002). ISBN 9780080441078.
- [101] W. RESEARCH. *Mathematica*. (2011). Version 8.0.1.0, [www.mathematica.com](http://www.mathematica.com).
- [102] I. LANGMUIR. *The effect of space charge and initial velocities on the potential distribution and thermionic current between parallel plane electrodes*. Physical Review **21**, 419–435 (1923). doi:10.1103/PhysRev.21.419.
- [103] I. N. BRONSTEIN and K. A. SEMENDJAJEW. *Taschenbuch der Mathematik*. Deutsch, Thun [u.a.] (2001). ISBN 3817120052.
- [104] E. G. RAMBERG and L. MALTER. *Potential Distribution for Space-Charge Limited Current between a Plane Accelerating Grid and Parallel Anode*. Journal of Applied Physics **23**, 1333–1335 (1952). doi:10.1063/1.1702070.
- [105] MAGNETLADEN.DE. *Neodymmagnete*. [www.magnetladen.de/service/neodym-magnete/](http://www.magnetladen.de/service/neodym-magnete/) (2012). Visited Mai 15, 2012.
- [106] HEATWAVE LABS INC. 195 Aviation Way, Suite 100, Watsonville, CA 95076-2069, USA.
- [107] LASERCUT24. Thomas Frey, Weimarische Str. 55, 99510 Apolda, Germany.
- [108] S. MEIR, C. STEPHANOS, T. H. GEBALLE and J. MANNHART. *Space-charge-free thermoelectronic conversion of heat into electric power*. submitted to the Journal of Renewable and Sustainable Energy (2013).
- [109] MAGNETSHOP.COM. *Materials*. [www.magnetshop.com/materials.html](http://www.magnetshop.com/materials.html) (2008). Visited Mai 15, 2012.

- [110] P. GLECKMAN, J. O'GALLAGHER and R. WINSTON. *Concentration of sunlight to solar-surface levels using non-imaging optics*. *Nature* **339**, 198–200 (1989). doi:10.1038/339198a0.
- [111] R. PITZ-PAAL. *Introduction to Solarthermal Power Plants - Lecture Script* (2010).
- [112] A. S. F. TESTING. *ASTM G173-03 Terrestrial (AM1.5) Reference Spectra* (2003). Available from <http://rredc.nrel.gov/solar/spectra/am1.5/>.
- [113] M. A. GREEN, K. EMERY, Y. HISHIKAWA, W. WARTA and E. D. DUNLOP. *Solar cell efficiency tables (version 40)*. *Progress in Photovoltaics: Research and Applications* **20**, 606–614 (2012). doi:10.1002/pip.2267.
- [114] F. CZIESLA, J. BEWERUNGE and A. SENZEL. *Lünen – state-of-the-art ultra supercritical steam power plant under construction*. In *POWER-GEN Europe, Cologne*. Cologne, Germany (2009).
- [115] J. L. CRONIN. *Modern dispenser cathodes*. *IEE Proceedings I, Solid-State and Electron Devices* **128**, 19–32 (1981). doi:10.1049/ip-i-1.1981.0012.
- [116] V. VLAHOS, J. H. BOOSKE and D. MORGAN. *Ab initio investigation of barium-scandium-oxygen coatings on tungsten for electron emitting cathodes*. *Physical Review B* **81**, 054207 1–15 (2010). doi:10.1103/PhysRevB.81.054207.
- [117] R. T. LONGO. *Physics of thermionic dispenser cathode aging*. *Journal of Applied Physics* **94**, 6966–6975 (2003). doi:10.1063/1.1621728.
- [118] H. AHMED and A. H. W. BECK. *Thermionic Emission from Dispenser Cathodes*. *Journal of Applied Physics* **34**, 997–998 (1963). doi:10.1063/1.1729584.
- [119] F. A. M. KOECK, R. J. NEMANICH, A. LAZEA and K. HAENEN. *Thermionic electron emission from low work-function phosphorus doped diamond films*. *Diamond and Related Materials* **18**, 789–791 (2009). doi:10.1016/j.diamond.2009.01.024.
- [120] F. A. M. KOECK and R. J. NEMANICH. *Low temperature onset for thermionic emitters based on nitrogen incorporated UNCD films*. *Diamond and Related Materials* **18**, 232–234 (2009). doi:10.1016/j.diamond.2008.11.023. WOS:000264429300031.
- [121] F. A. M. KOECK, R. J. NEMANICH, Y. BALASUBRAMANIAM, K. HAENEN and J. SHARP. *Enhanced thermionic energy conversion and thermionic emission from doped diamond films through methane exposure*. *Diamond and Related Materials* **20**, 1229–1233 (2011). ISSN 0925-9635. doi:10.1016/j.diamond.2011.06.032. WOS:000295300800026.
- [122] M. KATAOKA, C. ZHU, F. A. KOECK and R. J. NEMANICH. *Thermionic electron emission from nitrogen-doped homoepitaxial diamond*. *Diamond and Related Materials* **19**, 110–113 (2010). doi:10.1016/j.diamond.2009.09.002.



# Acknowledgements

Mein Dank gilt zuallererst meinem Doktorvater Herrn Prof. Dr. Jochen Mannhart. Für seinen Mut, dieses spannende Projekt aufzugreifen, das Herz, mit dem er stets dabei war und sein Vertrauen mir gegenüber. Die ständige Unterstützung, die vielen Diskussionen, Anregungen und Ideen. Und seine große Begeisterung — für unser Projekt und für die gesamte Physik — mit der Herr Mannhart allen Herausforderungen entgegentritt und die er mit uns geteilt und auf uns übertragen hat.

Ganz besonders bedanke ich mich bei Stefan Meir. Wir haben das Projekt von Anfang an gemeinsam bestritten. Ohne die intensive, offene und fruchtbare Zusammenarbeit wäre dieses Projekt so nicht möglich gewesen. Viele Sachverhalte haben wir nur gemeinsam erarbeiten und verstehen können und die besten Ideen sind in unseren teils endlosen Diskussionen entstanden. Ich möchte mich auch für die gemeinsame Zeit im Büro bedanken, die Bereitschaft und das Durchhaltevermögen, Probleme bis ins letzte Detail durchzudenken, für Zotero, Joghurt, Musik und Kekse.

Weiter möchte ich Herrn Prof. Dr. Armin Reller danken, für die Unterstützung während des gesamten Projekts, die wichtigen Diskussionen und die Übernahme der Zweitkorrektur. Ich möchte mich außerdem bei Herrn Reller für die Möglichkeit, sein Team und die Arbeit an seinem Lehrstuhl kennenzulernen, bedanken.

I want to thank Prof. emer. Dr. Theodore H. Geballe from Stanford University, who gave the initial impetus for the project and made substantial contributions to our concept. Without him, this dissertation would not have been possible.

Ich danke Dr. Andreas Schmehl, der entscheidende Ideen zu unserem Konzept beigetragen und uns bei jeglichen experimentellen Fragen tatkräftig unterstützt hat.

Besonders möchte ich mich bei Herrn Prof. Dr. Thilo Kopp bedanken, für seine Unterstützung während meiner gesamten Zeit am Lehrstuhl, seine Herzlichkeit, die vielen wissenschaftlichen und persönlichen Gespräche und die immer offene Tür.

Ich bedanke mich bei Herrn Dr. German Hammerl für die ständige Bereitschaft und die Geduld, mir bei verschiedenen Problemen, vor allem aber bei jeglichen  $\text{\LaTeX}$ -Fragen und kleineren Katastrophen zu helfen.

Dr. Florian Loder möchte ich danken für seine Hilfe bei vielen Fragen theoretischer Natur. Obwohl er eigentlich nicht direkt mit unserem Projekt verbunden war, hat er mich

## *Bibliography*

in zahlreichen Diskussionen unterstützt, sich in unsere Probleme intensiv hineingedacht und in einigen schwierigen Modellrechnungen sehr geholfen.

Dr. Rainer Held und Dr. Martin Breitschaft danke ich herzlich für viele wichtige Anregungen, Anmerkungen und das eine oder andere Glas vorzüglichen Weins.

Christoph Richter, Rainer (als) Jany und Klaus Wiedenmann danke ich für die Hilfe bei unserem Projekt und den vielen Dingen drum herum, aber vor allem für die lange gemeinsame Zeit, ob beim Dart, beim Kaffee, bei Spieleabenden, beim Grillen, im Walsertal oder im Barbershop.

Alexander Herrnberger danke ich für seine unglaubliche Hilfsbereitschaft, seine ruhige Hand und die Geduld, mit der er jedes Problem angeht. Ich habe wirklich viel von ihm gelernt.

Dem ganzen Team vom Lehrstuhl Experimentalphysik VI danke ich herzlich für die lange, gute Zeit, die Hilfe, die Unterstützung und die tolle Atmosphäre. Ich hatte großes Glück, in diesem Team mitarbeiten zu können. Ganz besonders möchte ich mich bei Eleonore Saladie bedanken, denn ohne sie und ihr Schaffen im Hintergrund wäre die produktive Zusammenarbeit gar nicht möglich gewesen.

Simon Meissner danke ich für die tolle Zusammenarbeit und seine herzliche, offene Art. Die gemeinsamen Seminare haben mir sehr viel Spaß gemacht, ich selber habe wohl am meisten dabei gelernt.

Lothar und Olli. Auch wenn Sie an diesem Projekt nur wenig beteiligt waren, hat mich unsere gemeinsame Studienzeit überhaupt erst soweit gebracht. Ich habe immer am meisten über die Physik in Zusammenarbeiten und Diskussionen gelernt und verstanden, und mit Lothar und Olli habe ich die intensivste Zeit meines Studiums geteilt, viel diskutiert (böse Zungen behaupten gar gestritten), gelacht und gelernt.

Meiner Schwester Merit gilt mein ganz besonderer Dank. Sie hat mich unterstützt, angetrieben, zu mir gehalten und mir Kraft gegeben.

Abschließend möchte ich meinen Eltern danken. Sie haben mir das Studium und diese Arbeit ermöglicht, haben mich immer unterstützt, auch in schwierigen Zeiten, mich ermutigt, meine Entscheidungen mitgetragen und mir Halt gegeben. Ich bin ihnen unglaublich dankbar.

# Curriculum vitae

<i>Zur Person</i>	Name	Cyril Stephanos
	Geburtstag	14. November 1980
	Geburtsort	Ulm
<i>Schulbildung</i>	9/1987 – 7/1991	Grundschule Reutti, Neu-Ulm
	9/1991 – 7/1993	Lessing-Gymnasium, Neu-Ulm
	9/1993 – 7/2000	Bertha-von-Suttner Gymnasium, Neu-Ulm
	7/2000	Abschluß: Allgemeine Hochschulreife
<i>Zivildienst</i>	10/2000 – 07/2001	Universitätsklinikum Ulm, HNO-Abteilung
<i>Studium</i>	10/2001 – 10/2008	Studium Diplom-Physik an der Universität Augsburg Diplomarbeit bei Prof. Dr. T. Kopp, Universität Augsburg: „ <i>Non-Local Pairing at Interfaces of Heterogeneous Electron Systems</i> “
	10/2008	Abschluß: Diplom-Physiker (Univ.)
<i>Promotion</i>	seit 01/2010	Doktorand an der Universität Augsburg
<i>Werdegang</i>	01/2009 – 07/2012	Wissenschaftlicher Mitarbeiter, Universität Augsburg
	seit 08/2012	Wissenschaftlicher Mitarbeiter, Max-Planck-Institut für Festkörperforschung, Stuttgart